

ProQuest Number: 10090151

All rights reserved

INFORMATION TO ALL USERS

The quality of this reproduction is dependent upon the quality of the copy submitted.

In the unlikely event that the author did not send a complete manuscript and there are missing pages, these will be noted. Also, if material had to be removed, a note will indicate the deletion.



ProQuest 10090151

Published by ProQuest LLC(2016). Copyright of the Dissertation is held by the Author.

All rights reserved.

This work is protected against unauthorized copying under Title 17, United States Code.
Microform Edition © ProQuest LLC.

ProQuest LLC
789 East Eisenhower Parkway
P.O. Box 1346
Ann Arbor, MI 48106-1346

Abstract

An analysis of data collected in the NA1 high energy photoproduction experiment at the CERN SPS is presented. The theoretical status of charmed particle decay is reviewed. The NA1 experimental apparatus is discussed.

Experiment NA1 used an active semiconductor target exposed to a 70-225 GeV tagged photon beam and the forward spectrometer FRAMM to collect data on the decay of particles carrying the charm quantum number. FRAMM was equipped with three lever arms for charged particle momentum analysis, electromagnetic calorimeters for neutral particle reconstruction and Cerenkov detectors for charged particle identification. The active target measured the charged particle multiplicity development along the beam axis to determine the decay length of particles. The proper time resolution of the target was $\sim 0.2 \times 10^{-13} \text{s}$.

A sample of sixty-three Λ_C charmed baryons are isolated in the decay channel $\Lambda_C \rightarrow pK^-\pi^+\pi^0 + cc$ via an inclusive analysis. Twenty-four of these Λ_C s have decay lengths resolved in the NA1 active target which can be matched to the information in the forward spectrometer FRAMM. The mean lifetime of these events is

$$\tau(\Lambda_C) = (1.4 \pm 0.4 \pm 0.3 \pm 0.2) \times 10^{-13} \text{s}.$$

A study of the sixty-three Λ_C s reconstructed in FRAMM indicates that a large proportion decayed via the channel $\Lambda_C \rightarrow \Delta^{++}K^{*-} + cc$, a decay which is believed to proceed exclusively through W exchange.

Contents

Section		Page
3	The FTASZ Experiment	80
3.0	Introduction	80
3.1	Initial State	80
3.2	Final State	80
3.2.1	Vertex Region	80
3.2.2	The Forward Spectrometer	80
3.2.3	Abstract	2
3.2.3.1	Contents	3
3.2.3.2	List of Tables	5
3.2.3.3	List of Figures	6
3.2.4	Acknowledgements	11
3.2.5	Introduction	12
3.2.6		
3.3	Charm Production	14
1	Review	14
1.0	Introduction	14
1.1	The Standard Model	14
1.2	Charm Decay	22
1.2.1	The Effective Weak Hamiltonian	25
1.2.2	Flavour Annihilation	29
1.2.3	W exchange	30
1.2.4	Pauli Interference	31
1.2.5	Λ_c Decay	33
1.2.6	Summary	35
1.3	Branching Ratios	36
1.4	Charm Production	38
2	The Active Target	41
2.0	Introduction	41
2.1	Semiconductor Detectors	44
2.2	The NA1 Target	47
2.3	Fluctuations of Energy Loss	55
2.4	Target Simulation	60
2.5	The Target Scanning Software	67
2.6	Scanning Efficiency	72
2.7	Nuclear Recoil	81

3	The FRAMM Spectrometer	85
3.0	Introduction	85
3.1	Initial State	85
3.2	Final State	87
3.2.1	Vertex Region	87
3.2.2	The Forward Spectrometer	90
3.2.3	The Photon Detectors	90
3.2.3.1	Photon Detector SD1	91
3.2.3.2	Photon Detectors SD2, SD4, and SD5	92
3.2.4	Tracking	95
3.2.5	Cerenkov Counters	98
3.2.6	The Trigger	101
3.3	Offline Production	103
4	Λ_C Analysis	106
4.0	Introduction	106
4.1	Large Impact Parameter Tagging	110
4.2	Δ and K^* Tagging	122
4.3	Λ_C Lifetime Measurement	132
5	Conclusions	151
	References	159

List of Tables

Table		Page
1.1	The fundamental fermions	15
1.2	The fundamental gauge bosons	15
1.3	Multiplet structure & electro-weak quantum numbers	18
1.4	Mark III D meson semileptonic branching ratios	36
1.5	Λ_C hadronic branching ratios	37
2.1	Relative ratio of charm to non-charm production	43
2.2	The NA1 target: parameters	50
2.3	Pulse height window cuts	68
2.4	Target event statistics	71
2.5	Target scanning efficiency using simulation program	74
2.6	Results of target visual scan	77
2.7	Summary of rejected events	80
2.8	Results of recoil visual scan	83
3.1	Characteristics of the photon detectors	91
3.2a	FRAMM magnet specifications	96
3.2b	Drift chamber stack locations	96
3.3	Drift chamber parameters	97
3.4	Cerenkov detector parameters	99
3.5a	Response of Cerenkov counters	100
3.5b	Ranges in which Cerenkovs discriminate $pK\pi e$	100
3.6	Final DST statistics	105
4.1	$\Lambda_C \rightarrow pK\pi\pi^0$ event summary	129
4.2	Summary of target configurations for the Λ_C sample	132
5.0	Summary of Λ_C lifetime measurements	154

List of Figures

Figure		Page
1.1	Spin 0 mesons of the $SU(F)_4$ flavour group	17
1.2	Spin 1/2 baryons of the $SU(F)_4$ flavour group	18
1.3	The Weinberg angle	20
1.4a	Spectator diagram for Cabbibo-favoured charm meson decay	23
1.4b	Spectator diagram for muon decay	23
1.5	Spectator diagram in infinite W mass limit	25
1.6	First order QCD corrections to weak Hamiltonian	26
1.7	Colour mixed diagram for charmed meson decay	28
1.8	Flavour annihilation diagram in D_S meson decay	29
1.9	W exchange in Λ_C decay	30
1.10	Symbolic representation of charmed meson decay	31
1.11	Pauli interference in D^+ decay	32
1.12	Diagrams available for Cabbibo-allowed Λ_C decay	34
1.13	Coherent photoproduction	38
1.14	The vector meson dominance model	39
1.15	The photon gluon fusion model	39
2.1	Principle of operation of the active target	45
2.2	The pn junction	46
2.3	The NA1 1983/84 active target	49
2.4	Noise sources for the target readout	51
2.5	Detail of the germanium monolith	52
2.6	Schematic section through the germanium monolith	52
2.7	Detail of the silicon detectors	53
2.8	Recipe for germanium monolithic detector	54
2.9	Schematic energy loss spectrum for a thin detector	55

2.10	Ionisation by charged particle in a medium	56
2.11	Pulse height distributions for the target	59
2.12	Sum of pulse height of target detectors (period 1B)	60
2.13	Principle operations in the GS simulation program	61
2.14	Photoproduction distribution in the target (simulation)	63
2.15	Uniform decay distribution seen in the NA1 target	64
2.16	D ⁰ energy spectrum from exclusive analysis	65
2.17	Example of monte carlo generated target event	67
2.18a	Distribution of first step found (period 2B)	70
2.18b	Distribution of second and third step found (period 2B)	70
2.19	Efficiency for finding levels of length n detectors	73
2.20a	Time efficiency using the target scanning software	75
2.20b	The same efficiency with max-min effects unfolded	76
2.21	Sample bad events rejected by the scanning program	79
2.22	Variables for recoil calculation	81
2.23	Distribution of 'recoil' candidate energies in m.i.p.s	82
2.24	Example of event with 'recoil' candidate	83
3.1	The H4 beam line	86
3.2	NA1 photon tagging arrangement	87
3.3	The FRAMM spectrometer	88
3.4	The NA1 vertex region	89
3.5	The high resolution vertex drift chamber	89
3.6	One plane of SD1	92
3.7	Lead glass electromagnetic calorimeters	93
3.8	Neutral pion invariant mass distribution	95
3.9a	Schematic diagram of the Cerenkov counters	98
3.9b	Cerenkov counter construction	99
3.10	$\pi\pi\pi^0$ effective mass distribution	101
3.11	Electron/pion discrimination using the electromagnetic calorimeters	104
4.0	The $p^+K^-\pi^+ + cc$ and $p^+K^-\pi^+\pi^0 + cc$ effective mass	107
4.1	The $p\pi$ effective mass with no impact parameter cuts	111
4.2	Definition of the impact parameter	112

4.3	Impact parameter details	113
4.4	Impact parameter distribution for events containing protons	115
4.5	The $p\pi$ effective mass, π impact parameter $< 1.0\text{cm}$	116
4.6	The $p\pi$ effective mass, π impact parameter $\geq 1.0\text{cm}$	116
4.7	$p^+K^-\pi^+\pi^0 + \text{cc}$ effective mass for different impact parameter cuts	118
4.8	$p^+K^-\pi^+ + \text{cc}$ effective mass for impact parameter $\geq 3.0\text{cm}$	119
4.9	$p^+K^-\pi^+\pi^0 + \text{cc}$ and $p^-K^+\pi^-\pi^0 + \text{cc}$ effective mass	120
4.10	Effective mass distribution for tracks associated with Λ_C candidates: $p\pi$ and $\pi\pi$	120
4.11	Impact parameter distributions for tracks in Λ_C events	121
4.12	Triangle plots showing evidence of resonant substructure	123
4.13	$p\pi$ effective mass distributions for events in Λ_C peak and background	123
4.14	$K\pi$ effective mass distributions	124
4.15	$p^+K^-\pi^+\pi^0 + \text{cc}$ effective mass for resonance tagging	125
4.16	$p^+K^-\pi^+\pi^0 + \text{cc}$ effective mass for Δ tagging	126
4.17	$p^+K^-\pi^+\pi^0 + \text{cc}$ effective mass for K^* tagging	126
4.18	Λ_C tagged via $\Delta^{++}K^{*-} + \text{cc}$ and $\Delta^+K^{*0}\text{-bar} + \text{cc}$	127
4.19	Sum of $\Lambda_C \rightarrow \Delta^{++}K^{*-} + \text{cc}$ and $\Delta^+K^{*0}\text{-bar} + \text{cc}$	128
4.20	Effective mass in the D_S region for events in the Λ_C peak when the proton is regarded as a kaon	130
4.21	Energy distribution for the $\Lambda_C \rightarrow p^+K^-\pi^+\pi^0 + \text{cc}$ events	131
4.22	Examples of target events from the Λ_C sample	134
4.23	Schematic diagram showing the effect of maximum and minimum observable decay lengths	137
4.24	Time resolution function for the target	139
4.25	Decay time distribution corrected for acceptance	140
4.26	Likelihood and support functions for 24 event sample	141

4.27	Distribution of $t-t_{\min}$ for events with decay steps of two and four	142
4.28	Distribution of $t-t_{\min}$ for events with decay step of two	143
4.29	Distribution of mean lifetime when one randomly generated decay time is added to the sample	144
4.30	Acceptance corrected decay time distribution of the wrong sign background events	145
4.31	Likelihood function for wrong sign background events	146
4.32	Monte carlo plot of τ_{input} against τ_{output}	147
4.33	Dependence of the fitted mean lifetime on the mixture of associated production	149
5.0	Analysis of $\Lambda_c \rightarrow \Delta K^*$ decays	152
5.1	World Λ_c lifetime results	155
5.2	D^0 effective mass from exclusive analysis	157
5.3	$M(D^*) - M(D^0)$ mass difference	157
5.4	Decay time distribution for D^0 s	158

Acknowledgements

Special thanks to my supervisor Phil March for his good advice, encouragement and his great enthusiasm for the subject.

High energy physics experiments are collaborative projects involving large groups of people. To all of those people contributing to experiment RA1 goes my sincere appreciation and gratitude. In particular I would like to thank my colleagues Giovanni Bagnan, Agnes Ciocal, Lorenzo Fox, Lionel Sacks and Roberto Tescheri. A number of illustrations in Chapter 3 are due to Lionel, who was good enough to share his work with me.

All members of the Royal Holloway and Bedford New College H.E.P. group work together as a team, and deserve special praise for being such a unique bunch - thanks to

If you have it [charm], you don't need anything else;
and if you don't have it, it doesn't much matter what else you have.

To all members of my family - James Barrie 1860-1937 - appreciation and thanks, especially to Dasher, Biddy, Del-Boy, The Old Man, Sandy and Sarah.

Thanks also to all my friends whose company has been so important: Helen, Tang, Tabir, Sylvia, Rery, Tonie, Lindsey, Alys, Jen, Louise, The Animal, Dave, Kevin, Steve, Geoff, 'Possum' Dave and to all the others who I do not list here, in particular my fellow students in the 'class of 85'.

Finally, thanks to the SERC for funding, and to all those at CERN who made the work possible.

Acknowledgements

Special thanks to my supervisor Phil March for his good advice, encouragement and his great enthusiasm for the subject.

High energy physics experiments are collaborative projects involving large groups of people. To all of those people contributing to experiment NA1 goes my sincere appreciation and gratitude. In particular I would like to thank my colleagues Giovanni Batignani, Agnese Ciocci, Lorenzo Foa, Lionel Sacks and Roberto Tenchini. A number of illustrations in Chapter 3 are due to Lionel, who was good enough to share his work with me.

All members of the Royal Holloway and Bedford New College H.E.P. group work together as a team, and deserve special praise for being such a unique bunch - thanks to Barry, Colin, John, 'Mad' Mac, Martin, Mary, Mike, Phil, Rachel, Terry, and Tony. Thanks too to RHBNC/Westfield oldboys Amir, Graham, Lionel, Murrough and Ted.

To all members of my family past and present my appreciation and thanks, especially to Basher, Bidy, Del-Boy, The Old Man, Sandy and Sarah.

Thanks also to all my friends whose company has been so important: Helen, Tariq, Tahir, Sylvie, Rory, Tonia, Lindsey, Alys, Jen, Louise, 'The Animal', Dave, Kevin, Steve, Geoff, 'Positron' Dave and to all the others who I do not list here, in particular my fellow students in the 'class of 85'.

Finally, thanks to the SERC for funding, and to all those at CERN who made the work possible.

Introduction

The charm quark was first postulated to exist by Glashow, Iliopoulos and Maiani in 1970, in order to cancel the strangeness changing neutral-current which had been observed in experiments to be strongly suppressed. Experimental confirmation of its existence had to wait until 1974 when the J/Ψ charmonium resonance was observed in e^+e^- interactions at SPEAR and in $p\text{Be}$ interactions at Brookhaven AGS. Since then the study of charmed states has become an important laboratory for testing the standard model of strong and electro-weak interactions.

The charm quark is one of five observed quarks (a sixth quark, top, is also believed to exist) which comprise the matter sector of the standard model participating in the strong interactions. Transitions between the types of quark, or flavours, proceed via the charged-current weak interactions. All hadronic matter is believed to consist of only these fundamental quarks.

Experiments on the charm sector have provided information on the quark masses, mixing angles and strong and electro-weak couplings, all basic input parameters to the standard model. The lifetime of the charmed quark is also a fundamental parameter of the model and therefore of considerable interest. Moreover, due to the subtle interplay of the strong and weak forces involved in charm decay, measurements of the charmed hadron lifetimes give insight into the dynamical quark-gluon structure of the hadrons.

Experiment NA1 was conducted in the north experimental area at the CERN SPS. The principle aim of the experiment was to measure the lifetime of hadrons containing the charmed quark, produced in high energy photon interactions with matter. The short lifetime ($\sim 10^{-13}\text{s}$), small production cross-section and typically large number of secondaries in events conspire to make the measurement of charm lifetimes a particularly difficult task. NA1 used a novel semiconductor active target placed in a 70-225 GeV photon beam, in association with the FRAMM multiparticle spectrometer. The active target could resolve proper decay times $\sim 0.2 \times 10^{-13}\text{s}$ and was read out at a high rate. Furthermore, the information delivered by the active target was amenable to efficient computer scanning techniques. FRAMM provided momentum analysis, charged particle identification and neutral particle reconstruction of the final state.

The NA1 collaboration have already published results on the lifetime of the D^+ meson, which was measured to be $\tau(D^+)=(9.5+3.1-1.9)\times 10^{-13}\text{s}$ [ALBINI 82], and the D^0 meson, which was measured to be $\tau(D^0)=(3.4+0.6-0.5\pm 0.3)\times 10^{-13}\text{s}$ [AMENDOLIA 88]. The author was an active participant in the latter analysis. This thesis presents an inclusive analysis of the NA1 data, searching for and measuring the mean lifetime of the charmed baryon Λ_c , the knowledge of which is still poor. A preliminary result has already been published by the collaboration: $\tau(\Lambda_c)=(1.1+0.8-0.4)\times 10^{-13}\text{s}$ [AMENDOLIA 87]. This thesis represents an improved analysis, resulting in larger final statistics, and contains a more detailed study of the background and bias to the measurement.

The author was solely responsible for the Λ_c analysis presented in chapter 4 and for the monte carlo programs used to correct the lifetime measurements for acceptance etc for both the published D^0 and Λ_c analyses. The author also contributed to the detailed study of the performance of the apparatus, eg lead glass calibration, target, Cerenkov and track finding efficiencies, and to the D^0 analysis.

Chapter one reviews the current theoretical status of charmed lifetimes. Chapter two details the active target and includes an assessment of its performance, and chapter three summarises the apparatus of the FRAMM spectrometer. Chapter four contains the methodology and results of the analysis. Chapter five, the conclusions, highlights the most interesting features of the results and compares them to the accumulated experimental data.

1: Review

1.0: Introduction

The object of this chapter is to give a brief outline of the physics relevant to the experiment. An overview of the standard model is followed by a discussion of the decay of the charmed quark. A summary of the experimental results on charmed hadron branching ratios of interest to the experiment is given. A discussion of the experimental status of charm hadron lifetimes has been deferred until the conclusion.

1.1: The standard model

The achievement of high energy physics is that numerous diverse systems and processes may be described in terms of a small number of fundamental (or, more accurately, structureless and indivisible on a scale of 10^{-19}m) building blocks, together with a small number of basic interactions between them. The principal distinction between these two groups of fundamental entities follows from their spin-statistics: the quanta of the matter fields have half-integral spin and thus obey Fermi-Dirac statistics (fermions), whilst the quanta of the force fields have integral spin, their behaviour being described by Bose-Einstein statistics (bosons). Table 1.1 summarises the fundamental fermions (note that the top quark t has not yet been observed). The corresponding antiparticles are obtained by the conjugation of table 1.1.

	flavour			electric charge	colour	weak t_3
Leptons	ν_e	ν_μ	ν_τ	0	0	$1/2$
	e	μ	τ	-1	0	$-1/2$
Quarks	u	c	t	$+2/3$	R,B,orG	$1/2$
	d	s	b	$-1/3$	R,B,orG	$-1/2$

Table 1.1: The fundamental fermions.

The fundamental gauge bosons, via the exchange of which the fermions of table 1.1 interact, are summarised in table 1.2 (neglecting the gravitational interaction, since the graviton coupling is $\sim 10^{-39}$ times weaker than the strong coupling).

Interaction	Gauge Group	Source	Gauge Bosons	Coupling Constant
Strong	SU(3)	Colour	Gluons	α_s
Electro-Weak	SU(2)xU(1)	Flavour	W^\pm, Z^0, γ	g, g'

Table 1.2: The fundamental gauge bosons.

Of these fundamental interactions only the charged current component (w^\pm) of the electro-weak interaction does not conserve the identity (flavour) of the fermions in table 1.1 (the neutral flavour changing weak currents exactly cancel in the standard model). Furthermore, the weak sector of the electro-weak interaction is observed to violate parity (P) and particle conjugation (C) symmetries, although it appears that CP is approximately, and CPT exactly, conserved.

Review

At least one further, possibly fundamental, boson is postulated but not yet observed: the neutral scalar (spin 0) Higgs particle responsible for the spontaneous breakdown of symmetry from the electro-weak $SU(2)_L \times U(1)$ group to the $SU(2)_L$ (weak interaction) and $U(1)$ (electro-magnetic) groups.

An important distinction exists between those fermions which do not carry a colour charge (leptons), and those which do (quarks). The quarks therefore participate in colour interactions, which are described by the theory quantum chromodynamics (QCD), based on the group $SU(3)_C$. In the fundamental representation of $SU(3)_C$ the base vectors form a triplet, the three 'colour charge' states of the quark, conventionally referred to as Red, Blue and Green; and the 8 representation of $SU(3)_C$, the group generators, are the massless gauge quanta (gluons). Since these gluons are not colour singlets (but are part of a colour octet) they also carry colour and may therefore interact with each other, which is, along with the fact that the gluons have zero mass, the reason for the strength of the colour force. Furthermore, the gluon self-coupling leads to the asymptotic freedom of the colour force: at low momentum transfer (large distance) the interaction is strong, whilst at large momentum transfer (short distance) the strength of the colour interaction decreases until, at a sufficiently short distance, perturbation methods may be applied.

It is observed that, despite extensive experimental searches, free particles in nature are colour singlets. Although this is believed to arise from the strength of the long distance colour force (infra-red slavery) no proof yet exists, and this must be regarded as an empirical fact. The net result is that quarks and gluons are confined to colourless bound states, the hadrons. The colourless hadronic bound states are observed in two types: three quark bound states (baryons) where each quark carries a different colour, and quark-antiquark bound state (mesons) where the quark carries a colour and the antiquark the corresponding anticolour.

$$\begin{aligned}
 B &= \frac{1}{\sqrt{6}} \epsilon_{\alpha\beta\gamma} q_1^\alpha q_2^\beta q_3^\gamma & \alpha, \beta, \gamma &= R, B, G \\
 M &= \frac{1}{\sqrt{3}} \delta_{\alpha\beta} q^\alpha \bar{q}^\beta
 \end{aligned}
 \tag{1.1}$$

Review

The QCD-quark model of hadronic matter has been successful in describing and predicting the static properties of hadrons (where the additive quantum numbers of the valence quarks combine to give the quantum numbers of the hadron). The spin 0 mesons of the $SU(4)_F$ flavour symmetry group (ie four quarks) are shown in figure 1.1, and the spin 1/2 baryons in figure 1.2. From a dynamical point of view, it is expected that the hadronic wave function also contains gluon and colour sea (q-antiq pairs) components which, due to the strength of the colour interaction on the hadron scale, do not succumb to perturbative methods. Thus the success of QCD at the quark level (short distance) is not matched on the hadron scale (long range) and experimental input is required.

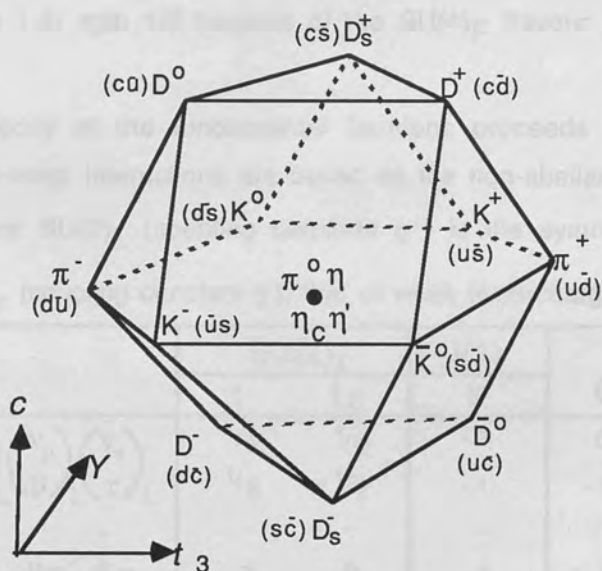


Figure 1.1: spin 0 mesons of the $SU(4)_F$ flavour group

Review

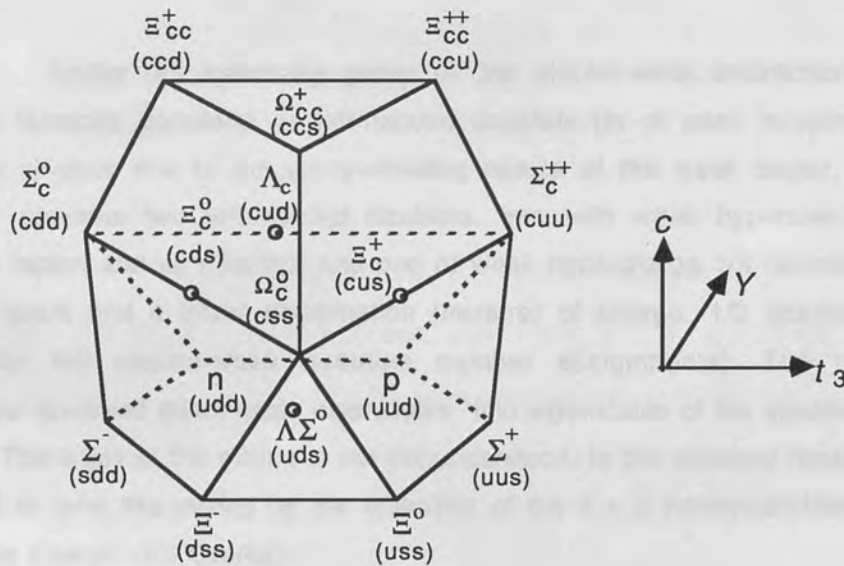


Figure 1.2: spin 1/2 baryons of the $SU(4)_F$ flavour group

The decay of the fundamental fermions proceeds via the weak interaction. The electro-weak interactions are based on the non-abelian gauge group $SU(2)_L \times U(1)_Y$, where $SU(2)_L$ (coupling constant g) is the symmetry group of weak isospin and $U(1)_Y$ (coupling constant g'), that of weak hypercharge.

		$SU(2)_L$		$U(1)$	Q			
		t	t_3	y				
FERMIONS	Leptons	$\begin{pmatrix} \nu_e \\ e \end{pmatrix}_L$	$\begin{pmatrix} \nu_\mu \\ \mu \end{pmatrix}_L$	$\begin{pmatrix} \nu_\tau \\ \tau \end{pmatrix}_L$	$1/2$	$1/2$	-1	0
		e_R	μ_R	τ_R	0	0	-2	-1
		$\begin{pmatrix} u \\ d' \end{pmatrix}_L$	$\begin{pmatrix} c \\ s' \end{pmatrix}_L$	$\begin{pmatrix} t \\ b' \end{pmatrix}_L$	$1/2$	$1/2$	$1/3$	$2/3$
	Quarks	u_R	c_R	t_R	0	0	$4/3$	$2/3$
		d'_R	s'_R	b'_R	0	0	$-2/3$	$-1/3$
		$\begin{pmatrix} \phi^+ \\ \phi^0 \end{pmatrix}$	$1/2$	$1/2$	1	1		
SCALARS	Higgs	$1/2$	$-1/2$	1	0			

Table 1.3: Multiplet structure and electro-weak quantum number assignments.

Review

Under the symmetry group of the electro-weak interactions the fundamental fermions transform as left-handed doublets (ie of weak isospin) and right-handed singlets due to the parity-violating nature of the weak sector. Each "generation" contains two left-handed doublets, one with weak hypercharge -1 containing a lepton and its neutrino, and one of weak hypercharge 1/3 containing a charge 2/3 quark and a linear combination (mixture) of charge -1/3 quarks (see table 1.3 for full electro-weak quantum number assignments). The mixing transforms the observed quark mass eigenstates into eigenstates of the electro-weak Lagrangian. The origin of the mixing is not yet understood. In the standard model it is conventional to treat this mixing by the operation of the 3 x 3 Kobayashi-Maskawa matrix on the charge -1/3 quarks:

$$\begin{bmatrix} d' \\ s' \\ b' \end{bmatrix} = V \begin{bmatrix} d \\ s \\ b \end{bmatrix} = \begin{bmatrix} V_{ud} & V_{us} & V_{ub} \\ V_{cd} & V_{cs} & V_{cb} \\ V_{td} & V_{ts} & V_{tb} \end{bmatrix} \begin{bmatrix} d \\ s \\ b \end{bmatrix} \quad (1.2)$$

The Kobayashi-Maskawa matrix may be conveniently approximated (ie neglecting CP violation) by:

$$V = \begin{bmatrix} 1 & \theta & \theta^3 \\ -\theta & 1 & \theta^2 \\ \theta^3 & -\theta^2 & 1 \end{bmatrix} \quad (1.3)$$

where θ is the sine of the Cabbibo angle ($\theta \approx 0.22$). The measured values and errors of the mixing parameters are [MARTIN 88]:

$$|V| = \begin{bmatrix} 0.9754 & 0.2206 & 0.0050 \\ 4 & 18 & 50 \\ 0.2203 & 0.9743 & 0.0460 \\ 19 & 5 & 60 \\ 0.0101 & 0.0449 & 0.9989 \\ 86 & 62 & 3 \end{bmatrix} \quad (1.4)$$

The Kobayashi-Maskawa matrix gives the hierarchy of transitions between generations. The diagonal elements are approximately equal to 1, implying the dominance of transitions between members of the same doublet. The non-zero off-diagonal elements are responsible for transitions from one generation to another.

The $SU(2)_L \times U(1)_Y$ local gauge invariance produces four massless gauge fields, $W^{a\mu}$ $a=1,2,3$ and B^μ . The symmetry of $SU(2)_L \times U(1)_Y$ is spontaneously broken to $SU(2)_L$ and $U(1)_Y$ by postulating a doublet of scalar Higgs fields, three degrees of freedom of which are transformed into helicity 0 states of the gauge fields, thereby removing the mass degeneracy of the multiplet. The physical gauge fields of the electro-weak interaction are then

$$\begin{aligned} W^\pm &= W^{a\mu} \quad a = 1, 2 && \text{charged weak} \\ Z^\mu &= \cos\theta_w W^{3\mu} - \sin\theta_w B^\mu && \text{neutral weak} \\ A^\mu &= \sin\theta_w W^{3\mu} + \cos\theta_w B^\mu && \text{electromagnetic} \end{aligned} \quad (1.5)$$

where the fundamental parameter θ_w (defined by $\tan\theta_w = g'/g$, the ratio of the coupling constants of $U(1)_Y$ and $SU(2)_L$), parametrises the mixing of the unphysical fields $W^{3\mu}, B^\mu$ onto the physical states γ, Z^0 in the neutral sector:

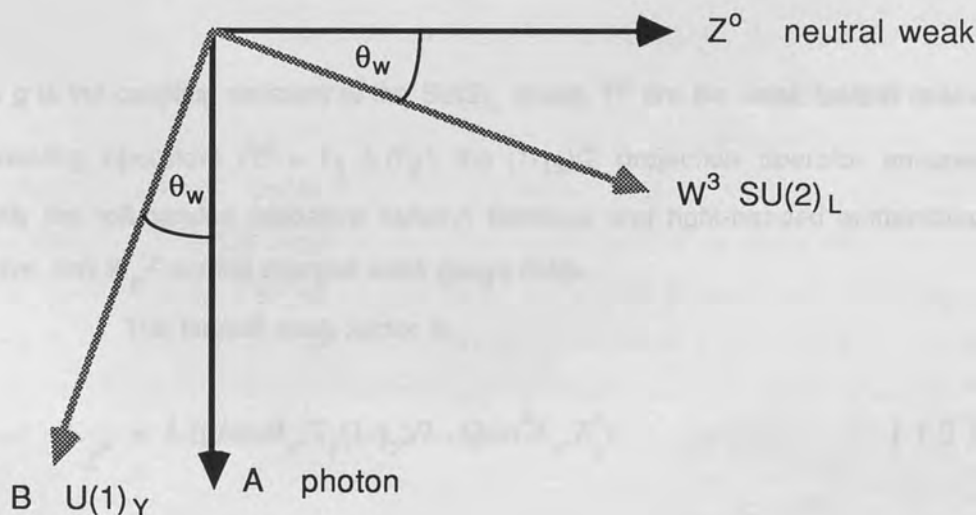


Figure 1.3: the Weinberg angle.

The current value of $\sin^2\theta_w$ as determined by experiment is 0.23 ± 0.005 [DARRIULAT 87].

Each sector of the Lagrangian takes the general form:

$$L(\lambda, \hat{O}, F) = \lambda \sum_i \bar{f}_i \gamma^\mu \hat{O} f_i F_\mu \quad (1.6)$$

where λ is the relevant coupling constant, O the generator of the symmetry group, F_μ is the appropriate gauge field, and f_i are the fermions of table 1.1.

For the electromagnetic interactions (1.6) becomes

$$L_{em} = L(e, Q, A_\mu) = e \sum_i \bar{f}_i \gamma^\mu Q f_i A_\mu \quad (1.7)$$

where e is the electron charge ($e = g \sin\theta_w$), Q the charge operator ($Q = T_3 + Y/2$), and A_μ the photon field. The charged weak sector becomes

$$L_{W^\pm} = L(g, T^\pm (1 - \gamma_5)/2, W^\pm) \quad (1.8)$$

where g is the coupling constant of the $SU(2)_L$ group, T^\pm are the weak isospin raising and lowering operators ($T^\pm = T_1 \pm iT_2$), the $(1 - \gamma_5)/2$ projection operator ensures that only the left-handed (negative helicity) fermions and right-handed antifermions are active, and W_μ^\pm are the charged weak gauge fields.

The neutral weak sector is

$$L_{Z^0} = L(g/\cos\theta_w, T_3(1 - \gamma_5)/2 - Q\sin^2\theta_w, Z_\mu^0) \quad (1.9)$$

T_3 being the generator of third component of weak isospin and Z_μ^0 the neutral weak gauge field.

The effective electroweak Lagrangian can now be written

$$L_{ew}^{eff} = L_{em} + L_{W^\pm} + L_{Z^0} \quad (1.10)$$

To summarise, the fermions fall into left-handed doublets and right-handed singlets of weak isospin $SU(2)_L$. Charged weak currents induce transitions between, and only between, members of the same doublet. Transitions between generations occur because the components of the doublets are mixed. Flavour changing weak neutral currents are cancelled by mixing. The electric charge of fermions is given the Gell-Mann Nishijima relationship $Q=t_3 - y/2$ where t_3 is the third component of the $SU(2)_L$ weak isospin and y is the $U(1)_Y$ weak hypercharge.

1.2: Charm decay

This section contains a brief review of the theoretical understanding of charm decays, specifically the Cabibbo-favoured non-leptonic decays of the charmed hadrons with which the experiment is concerned.

As indicated in section 1.1, the flavour changing $\Delta s = \Delta c = 1$ decay of the charmed quark is a weak charged current process. In the valence quark approximation the simplest model charmed hadron decay is the ' β -decay' or spectator process in figure 1.4a (so-called since the light quark does not participate in the decay, taking the passive role of a spectator). The decay of the charmed baryon Λ_c in the spectator model is the same as the top half of figure 1.4a along with two light spectator quarks. Note that for the charmed mesons the spectator amplitude is expected to be dominant due to the helicity suppression of the annihilation and W exchange amplitudes, whilst for charmed baryon decay the helicity suppression is lifted and the W exchange amplitude is expected to be non-negligible.

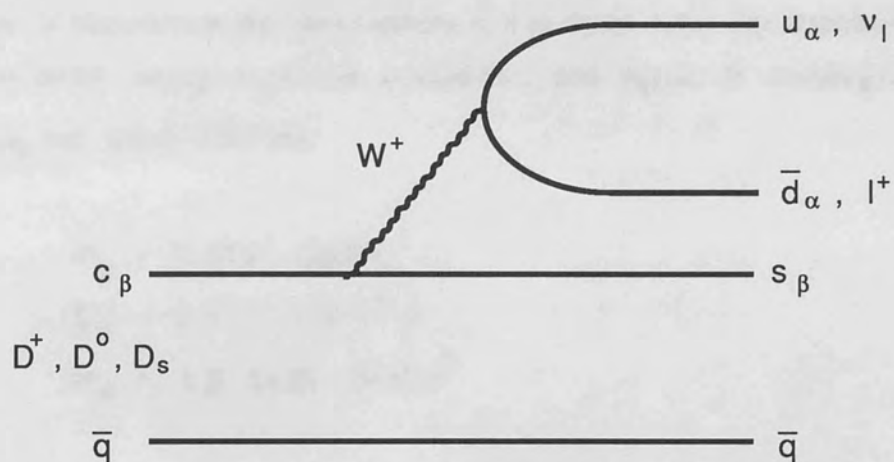


Figure 1.4a: the spectator diagram for Cabbibo-favoured charmed meson decay.

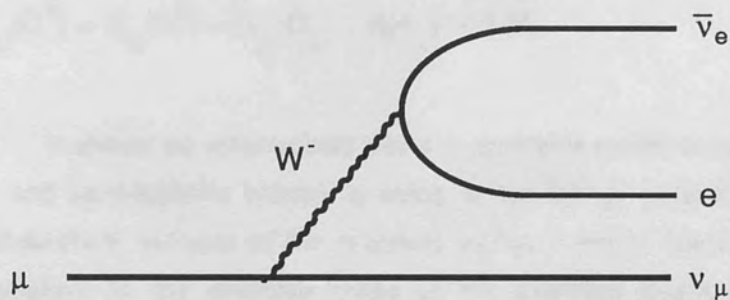


Figure 1.4b: the spectator diagram for muon decay.

Assuming a universal strength for the weak interaction, a direct comparison of diagram 1.4a with the 'model' weak decay process of diagram 1.4b [KALMUS 82] gives the spectator model prediction:

$$\tau_c = \frac{1}{n_{sl} + 3n_{nl}} \left(\frac{m_\mu}{m_c} \right)^5 \tau_\mu \quad (1.11)$$

$$B_{sl} = \frac{1}{n_{sl} + 3n_{nl}}$$

where the factor of 3 on the number of non-leptonic channels (n_{nl}) derives from the

number of colours (see the colour indices α, β in figure 1.4a). For Cabibbo-favoured charm quark decay $n_{\text{fl}}=1$, ie $c \rightarrow s u \bar{d}$, and $n_{\text{sl}}=2$, ie $c \rightarrow s e \nu_e$ and $c \rightarrow s \mu \nu_\mu$. Using [PDG 86]:

$$m_\mu = 0.1057 \text{ GeV}/c^2$$

$$\tau_\mu = 2.197 \times 10^{-6} \text{ s}$$

$$m_c = 1.5 \text{ (1.8) GeV}/c^2$$

we arrive at the predictions (spectator contribution only):

$$\tau(D^+) = \tau(D^0) = \tau(D_s) = \tau(\Lambda_c) \approx 7.6 \text{ (3.1) } \times 10^{-13} \text{ s} \quad (1.12)$$

$$B_{\text{sl}}(D^+) = B_{\text{sl}}(D^0) = B_{\text{sl}}(D_s) = B(\Lambda_c) \approx 20\%$$

It should be emphasised that the spectator model predicts equality of the lifetimes and semi-leptonic branching ratios of the lowest lying charmed hadron states. The theoretical estimate of the charmed meson lifetimes made in this way is extremely sensitive to the effective mass of the charmed quark which, due to confinement, is only poorly known. Nevertheless, the prediction of the charmed hadron lifetimes in the 10^{-13}s region must be regarded as a considerable achievement for the model. Experiment has since established that the lifetimes of the D^0, D^+, D_s and Λ_c are indeed in the 10^{-13}s regions, but further indicates marked inequalities between D^0, D^+, D_s and Λ_c lifetimes and semi-leptonic branching ratios (see table 1.4 for the Mark III D semileptonic branching ratios).

It has been pointed out that since the semi-leptonic decays of the charmed particles are due to the transition (spectator process) $c \rightarrow s + l^+ + \nu_l$ which predicts equality between the charmed hadron semi-leptonic decay rates, the lifetime inequality must clearly arise from differences in the non-leptonic decay widths [ROSEN 80].

The spectator model effectively assumes that the charm quark is asymptotically heavy so that the decay of the charmed hadron may be treated as free

quark decay, and the study of such a system would be expected to reveal the fundamental nature of the quark weak interactions. The departure of the data from the expectations of the simple spectator model indicates that additional processes other than the spectator amplitude are involved. The charmed quark should thus be regarded as "medium-heavy", with pre-asymptotic boundstate effects contributing to the total decay width of charmed hadrons. The study of charmed hadron decay should therefore provide some insight into the dynamical nature of the QCD bound states.

1.2.1 The effective weak Hamiltonian

The operation of the effective weak Hamiltonian on the particle state vectors gives the transition matrix elements:

$$M = \langle f | H_W^{eff} | i \rangle \quad (1.13)$$

For charm decay, the low mass of the charm quark relative to the W mass ($M_C \ll M_W$) means that the W boson propagator effectively reduces to $\frac{1}{M_W^2}$ and is absorbed into the Fermi coupling constant G_F . Thus in the limit of $M_W \rightarrow \infty$ we obtain the Fermi four fermion point interaction and the effective weak interaction becomes:

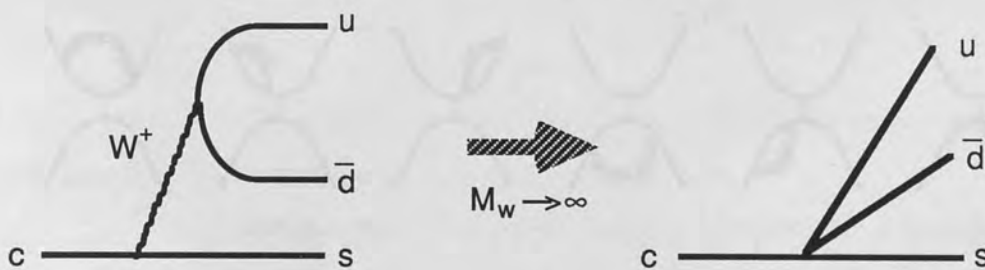


Figure 1.5: spectator decay in the infinite W mass limit.

$$H_W = \frac{G_F}{\sqrt{2}} (J_\mu^+(0) J_\mu^-(0) + hc) \quad (1.14)$$

where G_F is the Fermi weak coupling constant ($G_F = 1.16637 \times 10^{-5} \text{ GeV}^{-2}$) and, considering only the non-leptonic part,

$$J_{\lambda}^{+} = (\bar{u} \bar{c} \bar{e}) \gamma_{\lambda} (1 - \gamma_5) V \begin{pmatrix} d \\ s \\ b \end{pmatrix}$$

$$J_{\mu}^{-} = (J_{\mu}^{+})^{\dagger}$$

(1.15)

It is not satisfactory to neglect the colour interaction given that the charm quark is not asymptotically heavy and we are led to short range virtual gluon corrections to the effective weak Hamiltonian [ALTARELLI 74],[GAILLARD 74], as in figure 1.6. The top line, a, represents the bare effective weak interaction whilst the diagrams marked b contribute to the self energy and vertex corrections and are absorbed into the effective coupling G_F . Those diagrams marked c modify the nature of the weak current, leading to the renormalisation of the weak coupling and a distortion of the colour structure, allowing effective colour changing weak interactions.

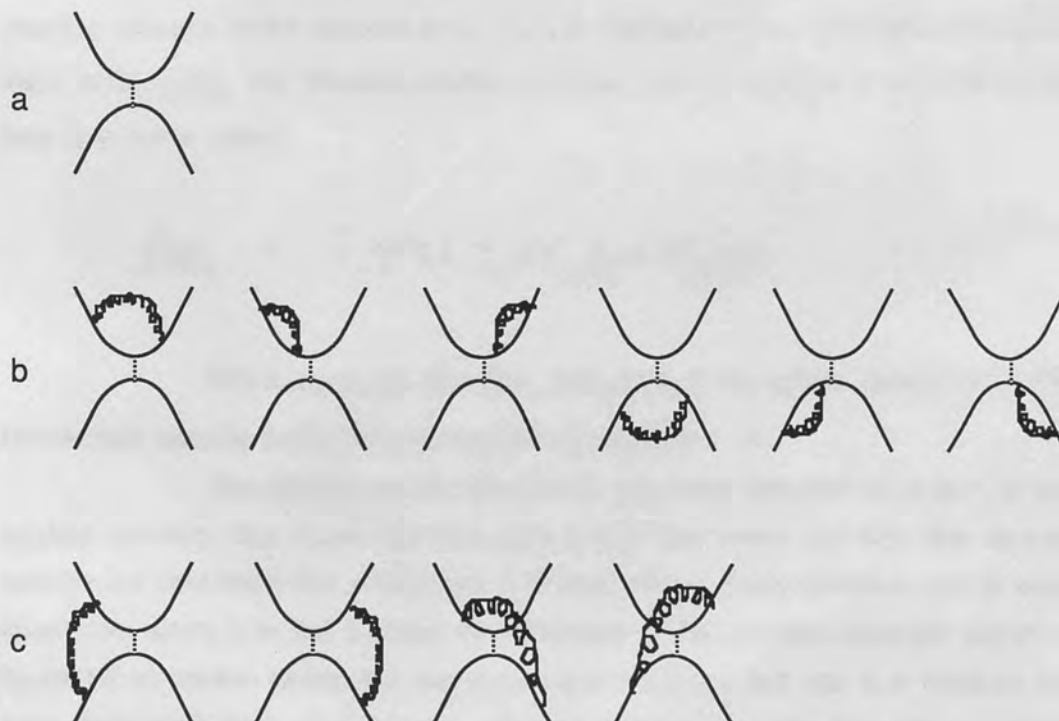


Figure 1.6: first order QCD corrections to the weak interaction.

The derivation of the QCD corrections to the weak Hamiltonian is beyond the scope of this thesis and the results are simply quoted (the reader is referred to [RUCKL 83] for a full account). The short range (ie hard gluon) QCD corrections are absorbed into the constants c_1 and c_2 in the effective weak Hamiltonian for $\Delta c=1$, renormalised and recast as:

$$H_{NL}^{\text{eff}} = \frac{G_F}{\sqrt{2}} \left\{ C_1 (\bar{U}D)_L (\bar{S}C)_L + C_2 (\bar{U}C)_L (\bar{S}D)_L \right\}$$

$$C_1 = \frac{C_+ + C_-}{2} \quad C_2 = \frac{C_+ - C_-}{2} \quad (1.16)$$

$$C_- = C_+^{-2} = \left[\frac{\alpha_s(\mu^2)}{\alpha_s(M_w^2)} \right]^{\frac{12}{33-2F}}$$

for three colors, where F is the number of flavours, and α_s the QCD coupling constant, which depends on μ , the renormalization point, and also on the QCD mass scale Λ_{QCD} . The following notation has been used in equation 1.16 for brevity (α here is a colour index):

$$(\bar{U}D)_L = \bar{u}_\alpha \gamma^\mu (1-\gamma_5) (V_{ud} d_\alpha + V_{us} s_\alpha) \quad (1.17)$$

When $c_- = c_+ = 1$ (the free field limit of no colour interactions) the Hamiltonian reduces to the bare Hamiltonian of equation 1.14.

The effective weak Hamiltonian has been rewritten as a sum of the original spectator four quark operator, plus a new four quark operator (the second term on the right hand side of equation 1.16 top). This is a new effective neutral weak interaction, which is in fact a colour mixed version of the spectator diagram, shown in figure 1.7 for meson decay. We can understand intuitively that this is a result of the hard gluon exchanges which lead to colour octet weak currents. The new current is neutral since, from the colour point of view, the u quark in the final state of the example in figure 1.7 B) *has the same colour* as the charm quark due to gluon

exchange, and the c and u quarks have the same electric charge.

Also note that due to the asymptotic freedom of the strong coupling equation 1.16 implies that c_- is greater than one (and c_+ is less than one), and thus the strength of the effective weak interaction is renormalised. Equation 1.16 further implies that as $\mu \rightarrow M_W$ the c_{\pm} approach unity, which is what is required since $\mu \geq M_W$ is the free field limit. Numerically the values of c_{\pm} are sensitive to the choice of Λ_{QCD} and μ . Using $F=4$, $\mu=1.5$ GeV and $\Lambda_{\text{QCD}}=0.25$ GeV, for example, the results are [RUCKL 83]:

$$C_+ = 0.74 ; C_- = 1.8 ; \eta = \frac{C_-}{C_+} = \frac{1}{C_+^3} = 2.43 \quad (1.18)$$

and $C_1=1.27$ and $C_2=-0.53$.

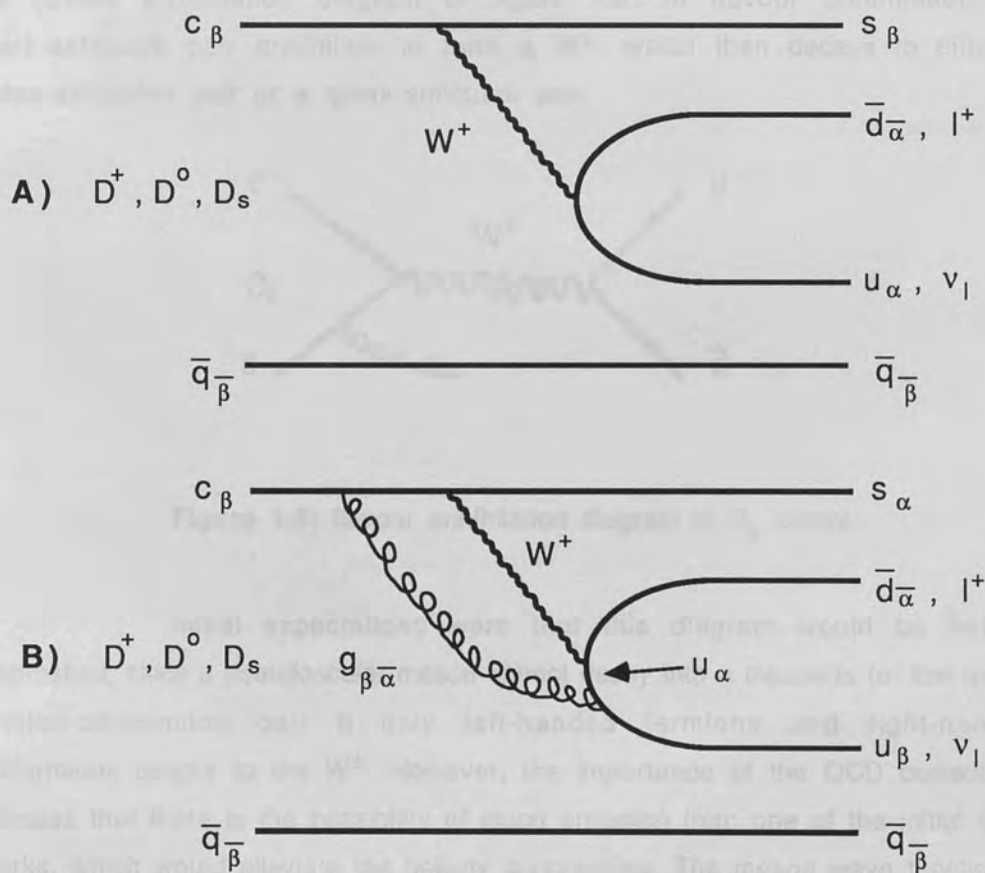


Figure 1.7: A) colour mixed diagram for meson decay; B) example of gluon exchange and its effect on the colour structure.

The net effect of using the short distance QCD corrected effective weak Hamiltonian modifies the non-leptonic decay widths by a factor proportional to $(2c_+^2 + c_-^2)$ [RUCKL 83]. Since $c_- > 1 > c_+$ this is an enhancement, and its magnitude is of the order of 1.4, using the identities in 1.18.

Thus the inclusion of the QCD corrections reduces the mean lifetimes and the semi-leptonic branching ratios of the charmed hadrons via the enhancement of the non-leptonic decay width, but offers no solution to the inequality of B_{sl}, τ between different charmed hadrons. For this we are forced to consider additional diagrams which contribute with different weights for different hadrons.

1.2.2: Flavour Annihilation

An additional diagram available for charged charmed meson decay is the flavour annihilation diagram of figure 1.8. In flavour annihilation the quark-antiquark pair annihilate to form a W^\pm , which then decays to either a lepton-antilepton pair or a quark-antiquark pair.

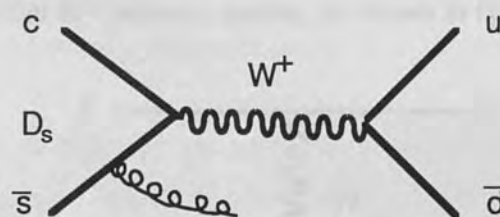


Figure 1.8: flavour annihilation diagram in D_s decay.

Initial expectations were that this diagram would be helicity suppressed, since a pseudoscalar meson cannot decay into a massless (or low mass) fermion-antifermion pair if only left-handed fermions and right-handed antifermions couple to the W^\pm . However, the importance of the QCD corrections indicates that there is the possibility of gluon emission from one of the initial state quarks, which would alleviate the helicity suppression. The meson wave function is then $|D_s\rangle = a_1|cs\text{-bar}\rangle + a_2|gcs\text{-bar}\rangle + \dots$, but the problem is now that the a_j

are not known. The probability of annihilation also depends on the overlap of the quark wavefunctions at the origin, which again is not well known.

The annihilation diagram is only Cabibbo-favoured for D_S decay, and not available at all for neutral meson and charmed baryon decay. The net effect would be to shorten the lifetime of the D_S relative to the other charmed hadrons and reduce the semi-leptonic branching ratio, by increasing the non-leptonic decay width. Quantitative predictions are subject to large uncertainties, but the contribution of annihilation diagrams to the total width is believed to be small. [SILVERMAN 88] calculates that the non-spectator contribution in D_S decay is only ~5% of the spectator decay width. That the non-spectator contribution is small is in agreement with the small measured branching ratios $D_S \rightarrow \pi\pi$ and in particular $D_S \rightarrow \rho\pi$, 1.0% and <0.28% respectively as measured by E691 [HITLIN 87].

1.2.3: W Exchange

Under certain conditions charmed hadron decay may also proceed via the exchange of a virtual W^\pm between quarks, as shown in figure 1.9.

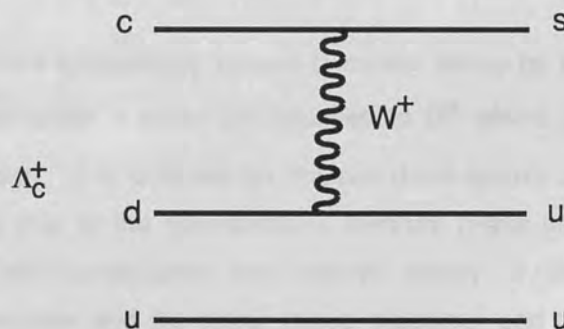


Figure 1.9: W^\pm exchange in Λ_c^+ decay.

The W^\pm diagram is Cabibbo-allowed in D^0 decay and charmed baryons also containing a d quark. However, for D^0 decays it is helicity suppressed unless a gluon is included in the meson wave function in the same argument as in section 1.2.2. Again the effect is expected to be small for mesons. The W exchange process has been

calculated to enhance D^0 decay by ~25% [SILVERMAN 88], which the authors point out would then require a destructive Pauli interference reduction of the D^+ decay of ~60% in order to explain the observed meson lifetime hierarchy. For the Λ_c there is no helicity suppression (ie a Qq subsystem may be in a spin 1 or a spin 0 state) and the diagram is expected to be significant. The net effect of the W^\pm exchange process is to reduce the lifetime of the Λ_c and less so the D^0 relative to the other charmed hadrons by increasing the non-leptonic decay widths, and therefore also decreasing the semileptonic branching ratios.

1.2.4: Pauli Interference

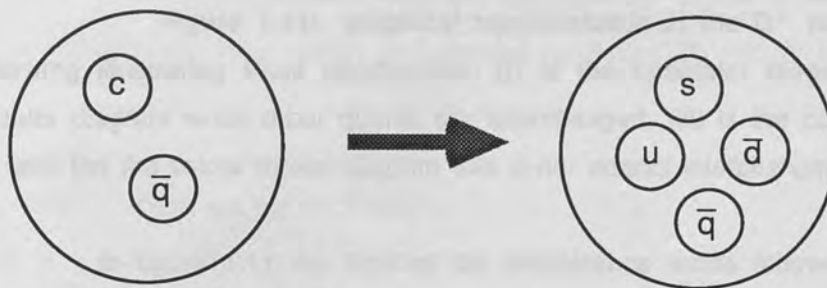


Figure 1.10: symbolic representation of charm meson decay.

If we symbolically denote D meson decay by figure 1.10, then in the case of D^+ , where $q\text{-bar} = d\text{-bar}$ (as opposed to D^0 where $q\text{-bar} = u\text{-bar}$, and D_s where $q\text{-bar} = s\text{-bar}$), it is possible for the two $d\text{-bar}$ quarks in the final state of D^+ decay to interfere due to the spin-statistics theorem (Pauli interference)[GUBERINA 79]. Thus for Cabbibo-favoured non-leptonic decay of the D^+ four diagrams contribute, the spectator and the colour mixed diagrams, and their counterparts when identical $d\text{-bar}$ quarks are interchanged [RUCKL 83]:

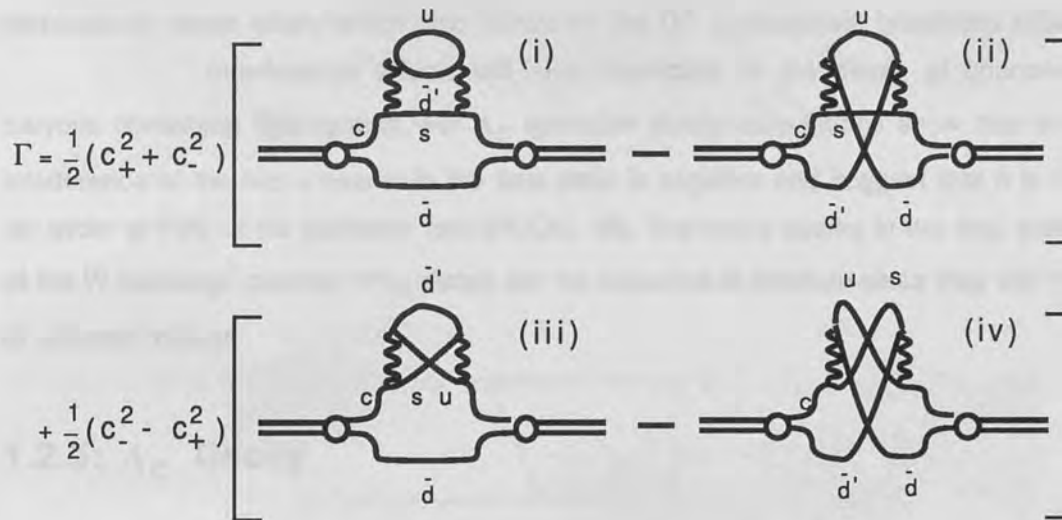


Figure 1.11: graphical representation of the D^+ non-leptonic width showing illustrating Pauli interference: (i) is the spectator diagram, (ii) is the spectator diagram when d-bar quarks are interchanged, (iii) is the colour mixed diagram, and (iv) the colour mixed diagram with d-bar quarks interchanged.

In figure 1.11 the sign of the interference terms follows from the fermi-dirac statistics ($\Psi \rightarrow -\Psi$ under interchange of identical fermions), and the factor 1/2 because there are two identical fermions in the final state. As stated in section 1.2.1 the result of the short distance QCD corrections to the weak interaction is that the left hand diagrams in figure 1.11 are proportional to $(2c_+^2 + c_-^2)$, and the interference terms can be shown [RUCKL 83] to be proportional to $(c_-^2 - 2c_+^2)|\phi|^2$, where ϕ is the overlap of the interfering quark wavefunctions. Since $c_-^2 > 2c_+^2$ the interference is destructive and the non-leptonic decay rate of the D^+ is suppressed, although note that if the strong interaction were turned off ($c_+ = c_- = 1$) then the interference would be constructive. Whilst the sign of the interference term is unambiguous, the magnitude depends on the degree of overlap of the d-bar quark wavefunctions, which is not well known. Typical estimates put the level of interference in D^+ decay between 10 and 40% of the spectator decay rate, using non-relativistic models [RUCKL 85].

In D^+ decay the interference is destructive and the net result is to lengthen the D^+ lifetime relative to other charmed hadrons via suppression of its

non-leptonic decay width, which also increases the D^+ semileptonic branching ratio.

Interference effects will also contribute to the decay of charmed baryons containing light quarks. For Λ_c spectator decay calculations show that the interference of the two u quarks in the final state is negative and suggest that it is of the order of 70% of the spectator rate [RUCKL 85]. The two u quarks in the final state of the W exchange process in Λ_c decay are not expected to interfere since they will be of different colour.

1.2.5: Λ_c Decay

The Cabbibo-allowed diagrams available for Λ_c decay are shown in figure 1.12. Charmed baryon decay, in particular Λ_c decay, is somewhat easier to treat from a theoretical point of view since the non-spectator amplitudes are not helicity suppressed at the valence quark level, so that estimates of the gluon content of the hadron wavefunction are not as critical as in meson decay. The major uncertainties arise from the lack of knowledge of the strong coupling (α_s) and from the error in the estimate of the overlap of the c and d quarks participating in the W exchange process, which is typically estimated from the hyperfine splitting of the Σ_c^+ and Λ_c^+ masses. The relative contribution of the different processes to the total decay width of the Λ_c have been calculated in a non-relativistic model [GUBERINA 86] to be:

$$\Gamma_{\text{spectator}} : \Gamma_{\text{interference}} : \Gamma_{\text{Wexchange}} \approx 1.04 : -0.65 : 1.98 \quad (1.19)$$

(the quoted widths are in units of 10^{12}GeV). This leads to an estimate of $\tau(\Lambda_c) \sim 2.3 \times 10^{-13}\text{s}$, which is in reasonably good agreement with the current experimental results, but note that since the contribution of the W exchange amplitude is large these results are very sensitive to the estimate of the c and d quark wavefunction overlap.

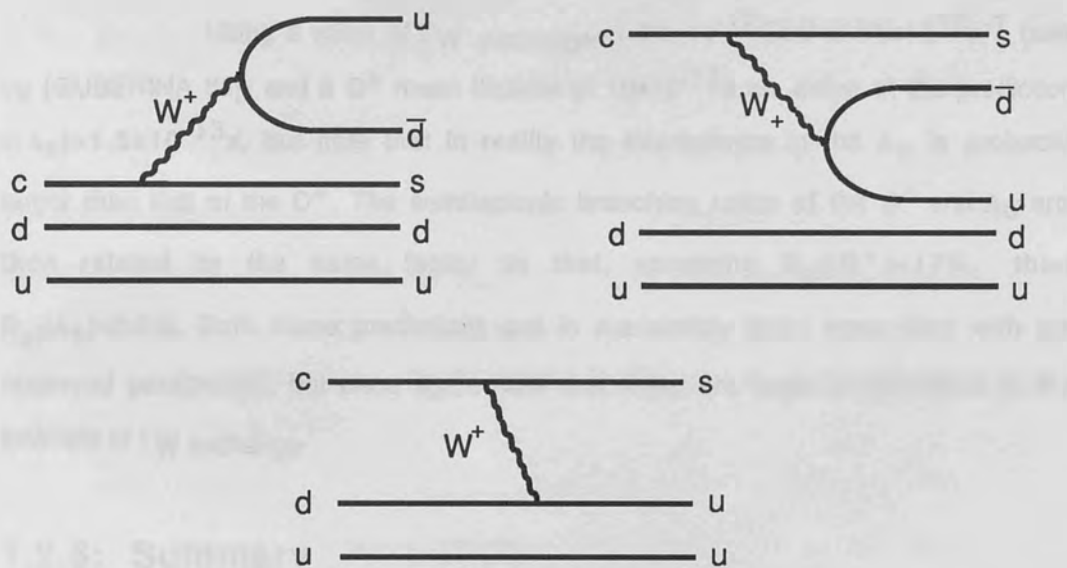


Figure 1.12: diagrams available for Cabibbo-allowed Λ_c decay.

A particularly simple method for estimating the Λ_c lifetime, once the D^+ lifetime is known and an estimate of the non-spectator decay width is calculated, has been given by [BARGER 80]. Writing the Λ_c total decay width as

$$\begin{aligned} \Gamma(\Lambda_c) &= \Gamma_{\text{spectator}}(\Lambda_c) + \Gamma_{W \text{ exchange}}(\Lambda_c) + \Gamma_{\text{interference}}(\Lambda_c) \\ &\approx \Gamma(D^+) + \Gamma_{W \text{ exchange}}(\Lambda_c) \end{aligned} \quad (1.20)$$

where the second identity follows from the equivalence of the spectator rates for different charmed hadrons (since it is the free field approximation), and also assumes that the d quark interference is the same for the D^+ and Λ_c , which is probably true within a factor of two. This leads to the lifetime relation

$$\tau(\Lambda_c) \approx \frac{\tau(D^+)}{[1 + \Gamma_{W \text{ exchange}}(\Lambda_c) \cdot \tau(D^+)]} \quad (1.21)$$

Using a value of $\Gamma_{W \text{ exchange}} = 1.98 \times 10^{-12} \text{ GeV} = 0.51 \times 10^{13} \text{ s}^{-1}$ (see eg [GUBERINA 86]) and a D^+ mean lifetime of $10 \times 10^{-13} \text{ s}$ we arrive at the prediction $\tau(\Lambda_C) \approx 1.6 \times 10^{-13} \text{ s}$, but note that in reality the interference in the Λ_C is probably larger than that of the D^+ . The semileptonic branching ratios of the D^+ and Λ_C are then related by the same factor so that, assuming $B_{\text{sl}}(D^+) \approx 17\%$, then $B_{\text{sl}}(\Lambda_C) \approx 2.8\%$. Both these predictions are in reasonably good agreement with the observed parameters, but once again note that there are large uncertainties in the estimate of $\Gamma_{W \text{ exchange}}$.

1.2.6: Summary

Departure of the observed lifetimes and branching ratios of the charmed hadrons from the simple heavy quark β -decay model has led to a better understanding of the weak interactions of quarks bound in hadrons and of the QCD nature of the hadron bound states.

Destructive interference in D^+ decay is now favoured as the most important mechanism for the D meson lifetime inequality, although W^\pm annihilation and exchange are believed to contribute to some small degree. The shorter Λ_C lifetime is believed to be due to the additional (unsuppressed) W^\pm exchange amplitude. Using the QCD corrected effective weak Hamiltonian, Pauli interference, W exchange, and dropping all non-leading terms in a $1/N_C$ expansion of the non-leptonic rates (N_C is the number of colours) [BURAS 86], a lifetime ratio $\tau(D^+)/\tau(D^0) > 1.6$ has been obtained [RUCKL 87]. Moreover, the same conditions predict a semileptonic branching ratio of $< 12\%$ for the D^0 and $\sim 19\%$ for the D^+ . The situation is even more favourable for the Λ_C , where predictions of the lifetime are of the order $2 \times 10^{-13} \text{ s}$, and the semileptonic branching ratio of order 5% , both of which are consistent with the available experimental data.

Although the theoretical agreement with the data can now be arranged to be fairly good, there is need for a consistent theoretical picture quantifying the contribution of the different processes to charm decay, particularly in the case of charmed meson decay.

1.3: Branching Ratios

The measured Λ_c branching ratios are summarised below in table 1.5 [HITLIN 87]. Note that only ~10% of the Λ_c branching ratios are accounted for. The semileptonic branching ratio of the Λ_c is $4.5 \pm 1.7\%$ [PDG 86]. Also, in table 1.4 are the Mark III results on the D^+, D^0 semileptonic branching ratios. References have not been given in the table unless used elsewhere in the text - the reader is referred to the original review by D. Hitlin.

Decay Mode	Branching Ratio (%)
$D^0 \rightarrow e^+ X$	$7.5 \pm 1.1 \pm 0.4$
$D^+ \rightarrow e^+ X$	$17.0 \pm 1.9 \pm 0.7$

Table 1.4: Mark III results on D meson semileptonic branching ratios.

Λ_c^+ Hadronic Branching Ratios		
Decay Mode	Experiment	Branching Ratio (%)
$\Lambda_c^+ \rightarrow pK^-\pi^+$	Mark II	2.0 ± 0.8
$\Lambda_c^+ \rightarrow p\bar{K}^0$	Mark II	1.4 ± 0.9
	ARGUS	1.2 ± 0.6
	CLEO	1.3 ± 0.8
$\Lambda_c^+ \rightarrow p\bar{K}^{*0}$	Mark II	0.36 ± 0.25
	BASILE 81	0.84 ± 0.59
	ARGUS	$< 1.18 @ 90\% \text{ CL}$
	NA32	0.56 ± 0.26
$\Lambda_c^+ \rightarrow \Delta^{++}K^-$	Mark II	0.34 ± 0.2
	BASILE 81	0.8 ± 0.47
	ARGUS	$< 0.89 @ 90\% \text{ CL}$
$\Lambda_c^+ \rightarrow p\bar{K}^0\pi^+\pi^-$	ARGUS	$< 1.9 @ 90\% \text{ CL}$
	BIS-2	3.9 ± 1.1
	CLEO	1.3 ± 1.0
$\Lambda_c^+ \rightarrow \Lambda\pi^+$	Mark II	$< 0.5 @ 90\% \text{ CL}$
	Baltay <i>et al</i>	1.3 ± 1.8
	Kitagaki <i>et al</i>	1.0 ± 1.4
	ARGUS	$< 0.33 @ 90\% \text{ CL}$
	CLEO	0.4 ± 0.6
$\Lambda_c^+ \rightarrow \Lambda\pi^+\pi^+\pi^-$	ARGUS	1.2 ± 0.6
	CLEO	1.6 ± 0.9

Table 1.5: Λ_c hadronic branching ratios.

1.4: Charm Photoproduction

Experiment NA1 is concerned with the diffractive coherent photoproduction of charmed states on complex nuclei, ie the process $\gamma+N \rightarrow c\bar{c}+N$, shown in figure 1.13. NA1 does not measure the charm photoproduction cross-section itself, but certain predictions of the existing models are of some relevance.

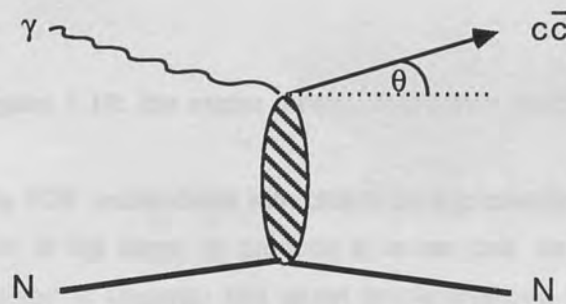


Figure 1.13: coherent charm photoproduction

The coherent process occurs for small four-momentum transfer squared, $t=(P_\gamma-P_{c\bar{c}})^2$, or equivalently high elasticity, $z=E_{c\bar{c}}/E_\gamma$, in order that there be no change of state in the target nucleus. The photon couples to the charm quarks via the electric charge, so that the production rate is proportional to q_c^2/M_c^2 . Experimental measurement puts the photoproduction cross-section of $c\bar{c}$ pairs at between 0.5 and 1.0 μb for $E_\gamma > 100\text{GeV}$ [HOLMES 85].

Two models exist to explain the charm photoproduction process: the vector meson dominance model (VDM), and the photon gluon fusion model (PGF). VDM (figure 1.14) treats photoproduction as the virtual transitions of the photon state into hadronic states, which then interact with the target and diffractively dissociate into open charm. Because the photon has $q = B = S = C \text{ etc} = 0$ the virtual transitions are dominated by the vector meson states (eg Ψ), and the photon beam is effectively considered as a vector meson beam of reduced intensity.

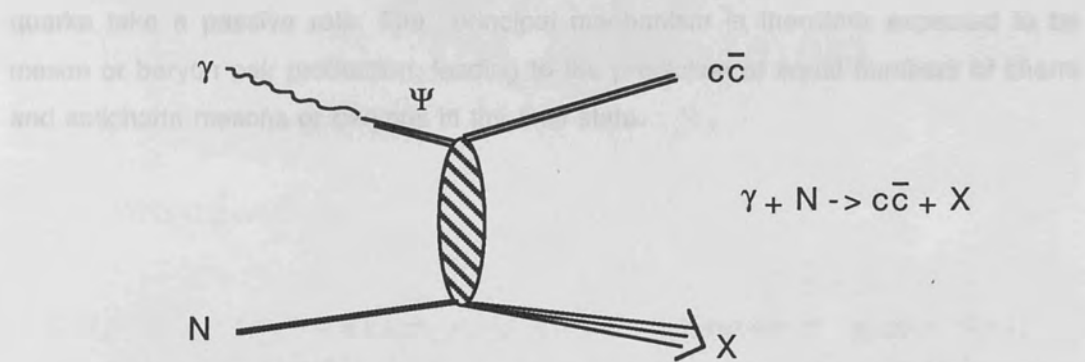


Figure 1.14: the vector meson dominance model

The PGF model deals with charm photoproduction as the fusion of the photon with a gluon in the target to produce a $c\bar{c}$ pair, as in figure 1.15. The $c\bar{c}$ pair is assumed to undergo soft gluon bremsstrahlung before hadronisation, since the gluon is in a coloured state.

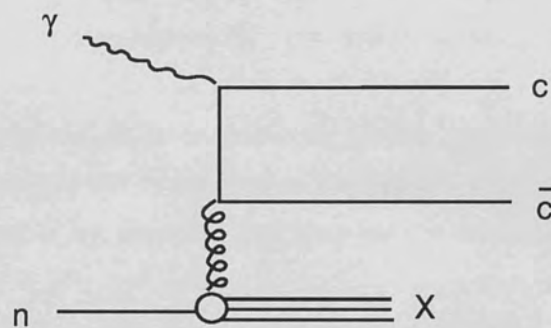


Figure 1.15: the photon gluon fusion model

Current experiments are not sensitive enough to discriminate between the two models.

For NA1 the most important feature of both models is that in the dominant processes the c and c -bar quarks are created symmetrically and the target

quarks take a passive role. The principal mechanism is therefore expected to be meson or baryon pair production, leading to the prediction of equal numbers of charm and anticharm mesons or baryons in the final state.

2.0: Introduction

As the text suggests, an earlier target extends the function of a target for high energy production from being simply a passive piece of material with which the beam interacts, to being at the same time an active component that contributes to the measuring process of the experiment. Commonly employed examples of active targets are equilibrium stacks, bubble chambers and, more recently, solid-state semiconductor devices.

As discussed in chapter one, the weak decays of the longest-lived charmed hadrons are in the 10^{-12} s regime, and are thus classified as short-lived. The measurement of particle lifetimes on such a fine scale presents obvious difficulties. Two distinct approaches have developed:

(i) using high resolution detectors to measure the decay length of the particles in fixed target experiments; and

(ii) measurement of the mean impact parameter in e^+e^- collision experiments.

Method (i) is conceptually simple and direct, since it relies on the fact that the laboratory decay length, i.e. the separation of the production and decay vertices, is related to the proper decay time via the relationship

$$l = \gamma \beta c t \quad (21)$$

and furthermore, since

$$\gamma \beta = p/mc$$

we have

$$l = \frac{p}{m} t \quad (22)$$

2: The Active Target

2.0: Introduction

As the term suggests, an *active* target extends the function of a target for high energy production from being simply a passive piece of material with which the beam interacts, to being at the same time an active component (i.e. detector) contributing to the measuring process of the experiment. Commonly employed examples of active targets are emulsion stacks, bubble chambers and, more recently, solid-state semiconductor devices.

As discussed in chapter one, the weak decays of the lowest lying charmed hadrons are in the 10^{-13} s regime, and are thus classified as short-lived. The measurement of particle lifetimes on such a time scale presents obvious difficulties. Two distinct approaches have developed:

- (i) using high resolution detectors to measure the decay length of the particles in fixed target experiments; and
- (ii) measurement of the mean impact parameter in e^+e^- collider experiments.

Method (i) is conceptually simple and direct, since it relies on the fact that the laboratory decay length, i.e. the separation of the production and decay vertices, is related to the proper decay time via the relationship

$$l = \gamma \beta c t \quad (2.1)$$

and furthermore, since

$$\gamma \beta = p / m$$

we have

$$t = \frac{l m}{p c} \quad (2.2)$$

the active target

It is clearly sufficient to measure the laboratory decay length in a high resolution detector, along with the momentum of the particle reconstructed from its decay products in a multiparticle spectrometer.

Method (ii) is possible, despite the spatial resolution being much greater than the decay length, because the mean of the impact parameter distribution will be different from zero if the production and decay vertices are separated. The precision goes as σ / n , where σ is the resolution and n the number of events, and thus the measurement requires high statistics.

The technique employed in this experiment is that which we have called (i). With regard to vertex detectors, emulsions provide the best spatial resolution ($\sim 1\mu\text{m}$), and for decay paths of 1mm or so are highly effective. However, as the decay path increases, and in particular in the case of neutral decays, the scanning time becomes very large. In order not to obscure interesting events with large backgrounds emulsions are typically employed in low rate situations, for example using neutrino beams. Bubble chambers can achieve resolutions of $\sim 10\mu\text{m}$ and require less scanning, when used as part of a hybrid detector, since a picture may be triggered by an interesting event in the associated spectrometer, but suffer also from low rate capability. Considerations of event rate become important in charm physics due to the small charm cross-section relative to the total hadron cross-section. The relative ratio of charm to non-charm production above threshold is dependent on the nature of the beam and is summarized in table 2.1.

Semiconductor detectors, on the other hand, are capable of both high spatial resolution and at the same time rates in excess of 10^5 , and are therefore in principle ideally suited to the measurement of charm particle lifetimes. Before describing in detail the semiconductor device employed in this experiment it is appropriate to emphasise that there are two different philosophies in this application of semiconductor detectors:

(a) ionization sampling telescopes counting charged particle multiplicity (this experiment); or

(b) high resolution tracking devices (silicon microstrip detectors, SMD's, and charged coupled devices, CCD's).

Table 2.1: Relative ratio of charm to non-charm production	
Beam type	relative ratio
e+e-	1
ν	10^{-1}
γ	10^{-2}
hadron	10^{-3}

Devices of type (b) can achieve space point resolutions of a few μm [DAMMERELL 84], and, as best exemplified by experiment E-691 at Fermilab, MSDs can achieve vertex resolution of $\sigma_z \sim 300 \mu\text{m}$ in the beam direction, and $\sigma_x \sim 20 \mu\text{m}$ orthogonal to the beam [ANJOS 87a].

We note in passing that considerable progress has been made in the use of yet another detector technology, scintillating optical fibres bunches, capable of high rates and reported spatial resolutions of $\sim 35 \mu\text{m}$ [CHARPAK 85].

The NA1 collaboration pioneered the use of the active semiconductor targets in charm physics, measuring for the first time by purely electronic means the lifetime of the D^+ meson [ALBINI 82]. The NA1 active target is of the type we have called (a) above: a fine grained, structured dE/dx telescope of semiconductor detectors. The charge released by ionization when charged particles cross each detector in the telescope allows the charged particle multiplicity of the event along the beam axis to be determined. Schematically, the technique is shown in figure 2.1.

Inspection of this figure reveals the limitation of the NA1 technique: whilst the production and decay points may be clearly seen and yield the required decay length, the association of a given charmed particle in the spectrometer to a given decay length in the target is only unambiguous in the case where both charm decays in the event are reconstructed and each charmed particle decays into a different number of charged particles in the final state. When this is not the case a careful treatment of the possible bias due to the misassociation of decay path with reconstructed particle

momentum must be considered in the final result. Furthermore, because individual final state particles cannot be associated with a decay vertex, all possible combinations of the final state particles must be considered in the mass analysis, with a corresponding large combinatorial background.

The dE/dx telescope is not without its advantages, however. A high laboratory momentum produces a strong forward boost, dilating the laboratory decay time and consequently extending (and hence allowing a more precise determination of), the decay length. The resolution in the beam direction σ_z is fixed by the granularity of the telescope and is therefore constant, and the relative precision (using equation 2.1) depends only on the decay length:

$$\frac{\sigma_z}{L} = \frac{k}{\gamma \beta c t} \quad (2.3)$$

2.1: Semiconductor Detectors

Solid state detectors behave essentially along the same lines as gas ionization chambers, but with a markedly lower ionization energy. Qualitative understanding of the principle of operation can be achieved by appealing to a simple model (see for example [DAMMERELL 84]) in which the semiconductor is considered as containing two distinct bands of energy levels (the conduction and valence bands) separated by a band gap E_g , reflecting the energy level structure of the individual atoms. The magnitude of the band gap defines the conduction properties of the material, since it is the excitation of a 'fixed' electron from the nominally filled valence band across the energy gap into the conduction band, where it becomes quasi-free, which allows conduction. Note also that the excitation process leaves a hole in the valence band, and there are thus two effective charge carrier types, negative electrons and positive holes.

the active target

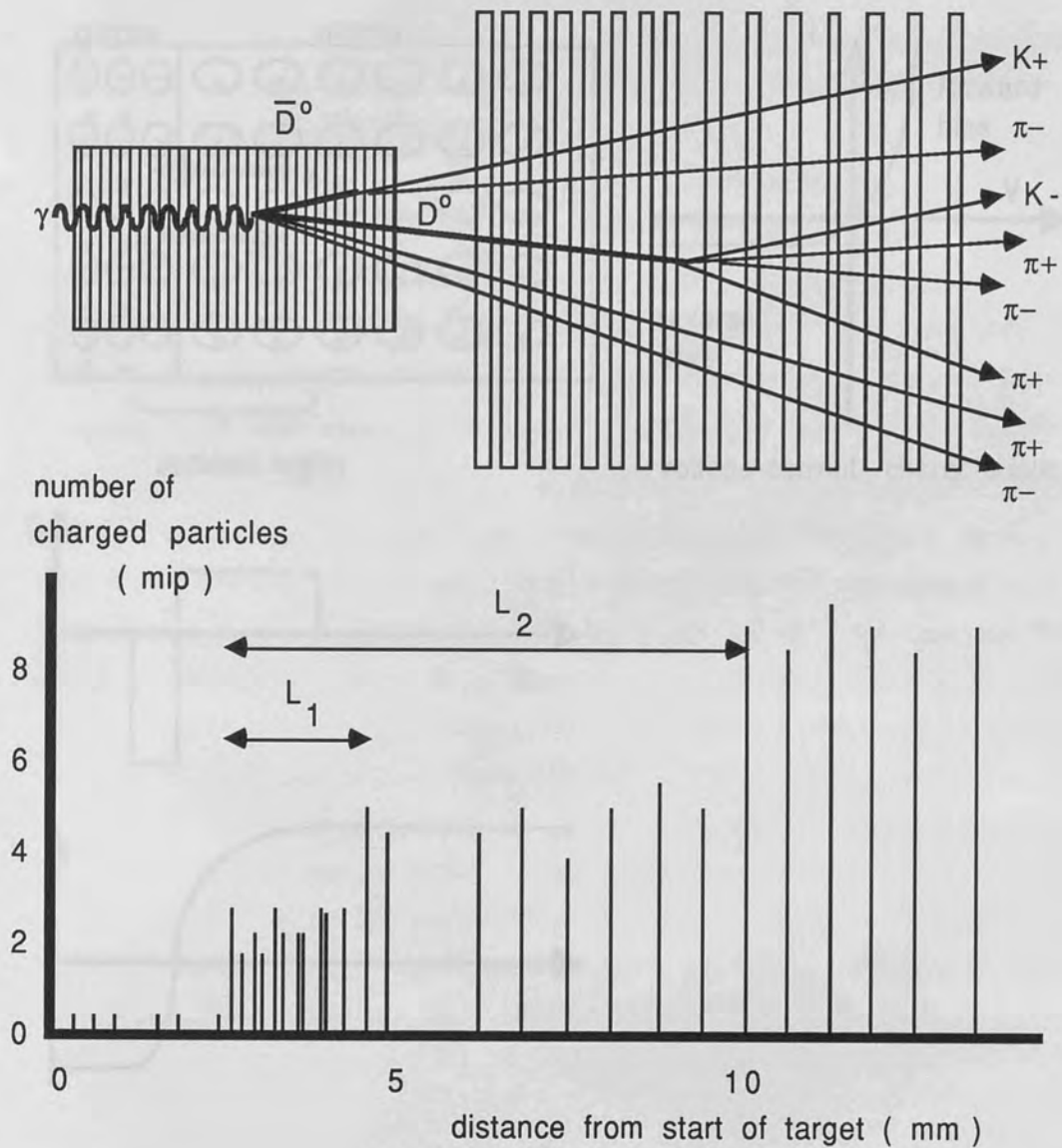


Figure 2.1: principle of operation of the active target

The *principle* of the semiconductor detector is then simple: a charged particle passing through a semiconducting crystal excites $n \sim E_{\text{LOSS}} / E_I$ electron-hole pairs via the ionization process, where E_{LOSS} is the energy lost by the particle and E_I is the energy required to excite one electron-hole pair. If the crystal is sandwiched between two electrodes then the charge released can be collected and processed.

the active target

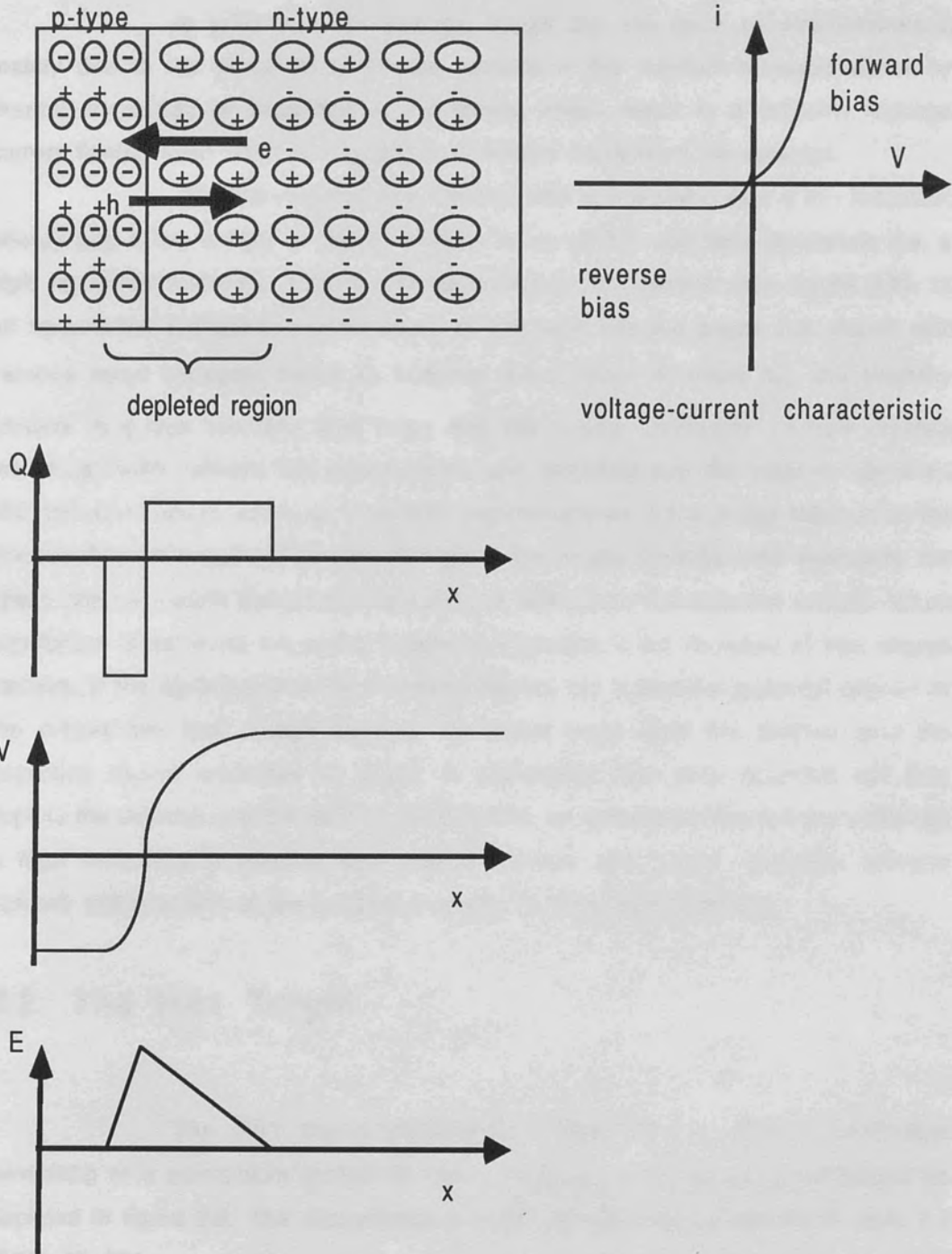


Figure 2.2: the pn junction

In practice, unfortunately, things are not quite so straightforward, mainly due to the presence of charge carriers in the medium released either by thermal excitation or impurities in the lattice, which result in a massive leakage current flowing even when no charged particles are incident on the detector.

What is required is a detector with at the same time a low ionization energy and a low density of charge carriers in the normal operating conditions (i.e. a high resistivity material). This is effected using an np junction (see figure 2.2). In an np junction a diffusion current flows, of electrons into the p-type (i.e. doped with valence three acceptor atoms to increase the number of holes n_h , the majority carriers in p-type crystals) and holes into the n-type (similarly n-type crystals are doped with valence five donor atoms and electrons are the majority carriers). This diffusion current leaves an excess of negative charge in the p-type adjacent to the junction and an excess of positive charge in the n-type material until eventually the space charge around the junction is sufficient to balance the diffusion current. When equilibrium is achieved the region around the junction is left depleted of free charge carriers. If the np junction is then reverse biased, i.e. a positive potential applied to the n-type, the free charge carriers are swept away from the junction and the depletion region increases in depth. A sufficiently high bias potential will fully deplete the detector and the desired conditions for an operational detector are achieved: a high resistivity (negligible free charge carriers and hence negligible leakage current) material with a low ionization energy (a large output pulse).

2.2: The NA1 Target

The NA1 target [AMENDOLIA 84a] is a structured telescope, consisting of a germanium monolithic block, followed by fifteen planes of silicon, as depicted in figure 2.3. The characteristics of the detector are summarized in table 2.2 [BELLINI 81].

In order for the target to be sensitive to short lifetimes it is necessary to demand close spacing (high granularity) of the detectors in the telescope. At the same time the requirement of a good signal to noise ratio must be observed. The noise sources may be shown schematically [GATTI 86] as in figure 2.4, where the charge Q released in the detector is represented by an ideal current source,

the active target

e_N is the total rms noise represented by an ideal voltage source at the amplifier input, and C_D is the detector capacitance.

At the amplifier output, when an infinitely narrow detector charge pulse Q is delivered to the input, the amplified pulse appears as a Gaussian with a variance $(ENC)^2$, where ENC is the equivalent noise charge defined by

$$ENC = \left[e_N^2 C_D^2 \right]^{1/2} \quad (2.4)$$

If the ENC is not small compared to the separation of the noise line and the pulse height spectrum for ionizing particles then it becomes impossible to discriminate with high efficiency between a particle in the detector and spurious pulses due to the noise, and indeed between different multiplicities of charged particles crossing the detector.

As can be seen from equation 2.4 the noise seen at the pre-amplifier output is essentially due to two sources, which are:

- (i) Intrinsic noise of the detector, resulting from the small leakage current, and from poor contacts;
- (ii) Noise in the pre-amplifier itself, which is proportional to the detector capacitance.

The latter is by far the dominant contribution. The capacitance of the detector, which behaves in the manner of a parallel plate capacitor, is inversely proportional to the detector thickness d . Moreover, because there is no charge amplification in the device, the signal delivered to the electronics is simply proportional to the thickness d . Hence the signal to noise ratio goes as

$$\frac{\text{signal}}{\text{noise}} \propto d^2 \quad (2.5)$$

which deteriorates rapidly as the detector thickness is reduced, and thus the necessary requirements of high granularity and good signal to noise conflict.

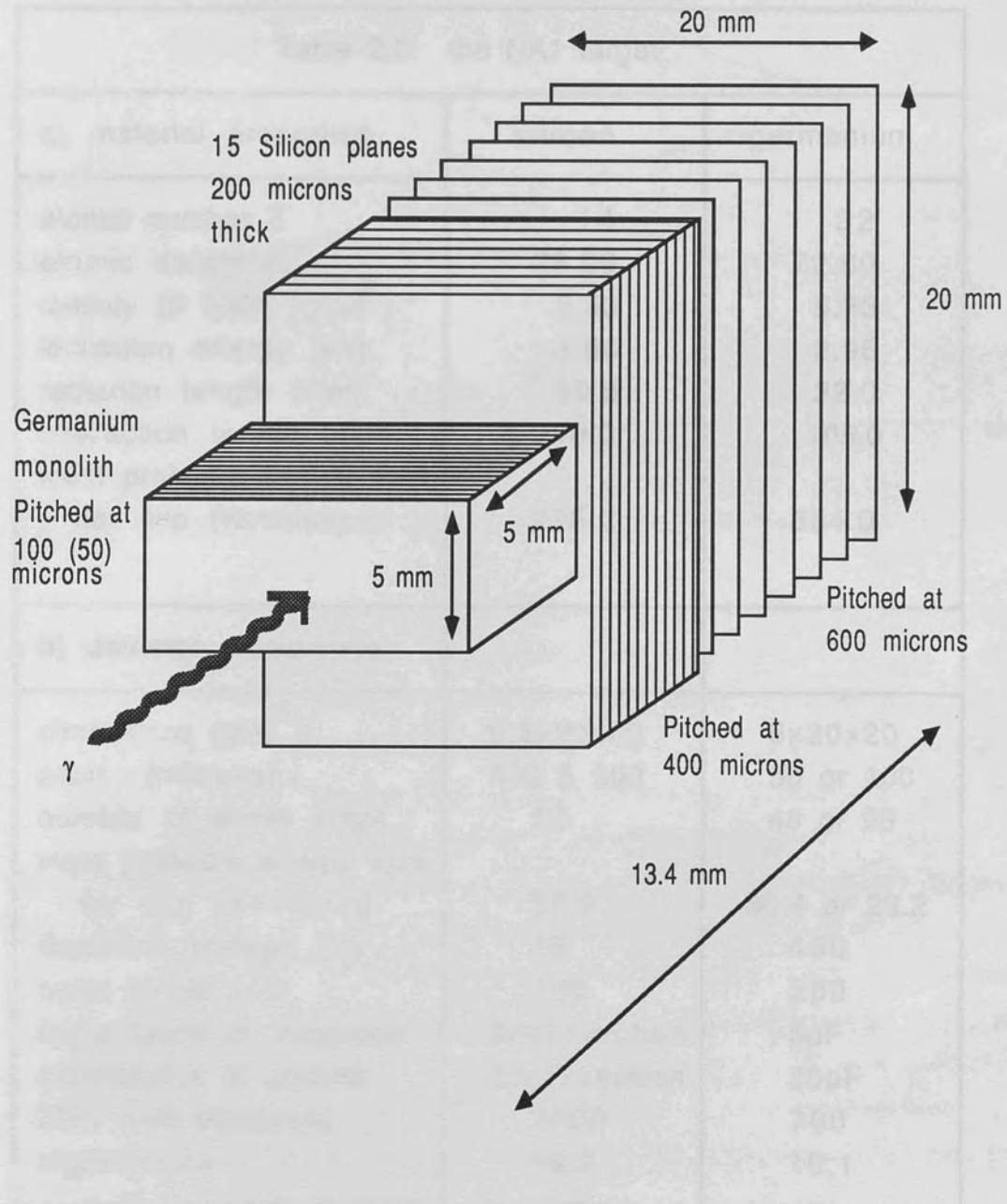
the active target**Figure 2.3:** the NA1 1983/84 active target

Table 2.2: the NA1 target		
a) material properties	silicon	germanium
atomic number Z	14	32
atomic weight A	28.06	72.60
density @ 300K (g/cm ³)	2.33	5.33
ionization energy (eV)	3.66	2.96
radiation length (mm)	98.0	22.0
interaction length (mm)	240.0	105.0
most probable energy loss for mip (Kev/mm)	285.0	584.0
b) detector parameters		
dimensions (mm ³)	0.2x20x20	5x20x20
pitch (microns)	400 & 600	50 or 100
number of active strips	15	48 or 96
most probable energy loss for mip (KeV/strip)	57.0	58.4 or 29.2
depletion voltage (V)	15	450
pulse length (ns)	100	200
capacitance at electrode	55pF/section	5pF
capacitance at preamp	80pF/section	30pF
ENC (rms electrons)	2200	700
signal:noise	10:2	10:1

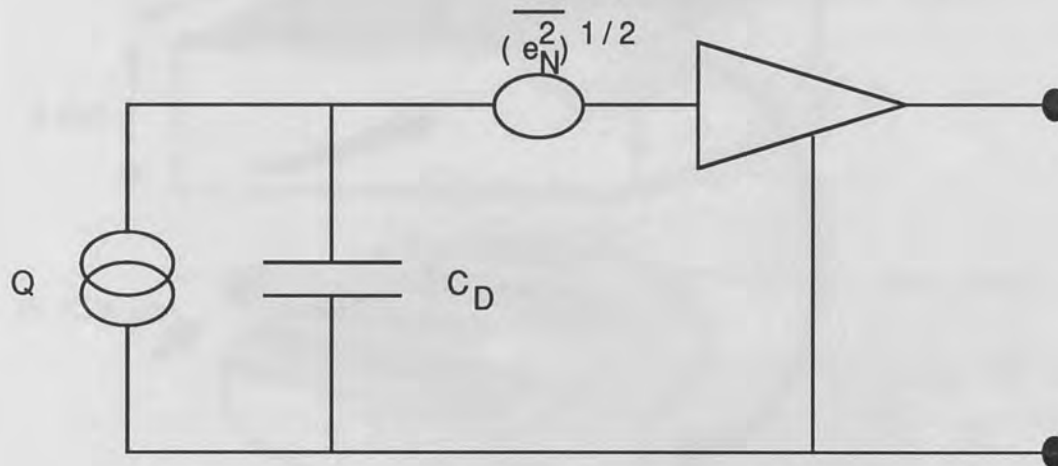


Figure 2.4: noise sources for the target readout

This problem has been solved by using the germanium monolith [AMENDOLIA 83],[AMENDOLIA 84b],[AMENDOLIA 84c], which has 96 (48) electrodes $25\mu\text{m}$ ($50\mu\text{m}$) wide and $25\mu\text{m}$ ($50\mu\text{m}$) apart, deposited on the upper face, orthogonal to the beam direction. On the opposite face a continuous contact has been deposited. This device operates as an effective telescope of detectors of $50\mu\text{m}$ ($100\mu\text{m}$) pitch orthogonal to the beam direction, since the charge cloud released by a minimum ionizing particle is drifted on to the finely grained electrodes by the potential which serves to reverse bias the detector. Germanium has been used because of its higher density and atomic number, and lower ionization energy than silicon, which conspire such that the germanium delivers ~ 2.5 times the charge than the equivalent thickness of silicon. Each electrode is connected to a different pre-amplifier, which sees a small capacitance because of the small electrode area and the large (5mm) thickness of the block. The first and last electrodes are not used to avoid the field non-uniformity at the ends.

The manufacture of the germanium monolith has been reported in [AMENDOLIA 84b],[AMENDOLIA 84c] and is summarised in figure 2.8. A total of six germanium targets were manufactured, three at $50\mu\text{m}$ pitch and three at $100\mu\text{m}$ pitch. The $100\mu\text{m}$ pitch version can resolve times down to $0.3 \times 10^{-13}\text{s}$ for a gamma factor of 30, if three strips are required to define a stable level .

the active target

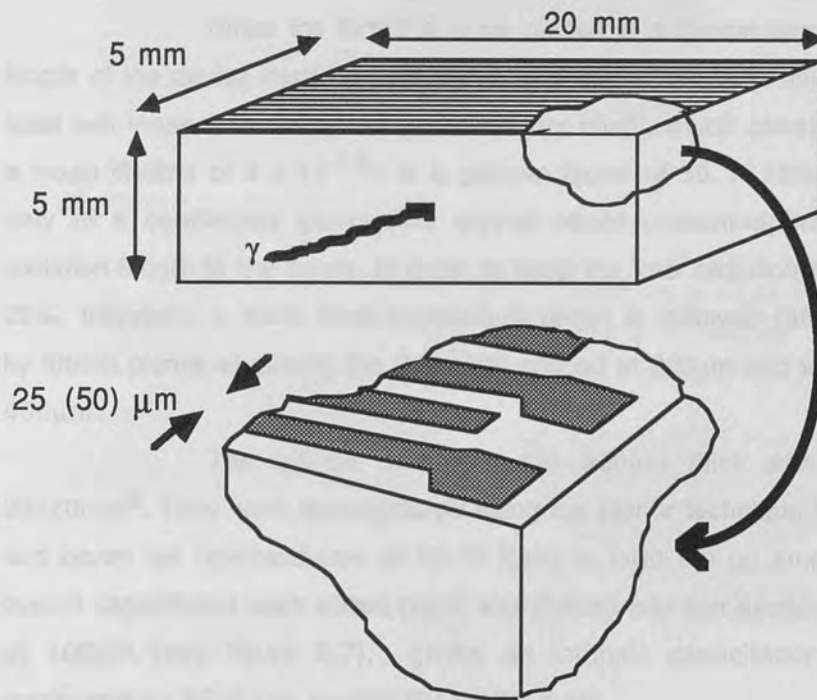


Figure 2.5: Detail of the germanium monolith.

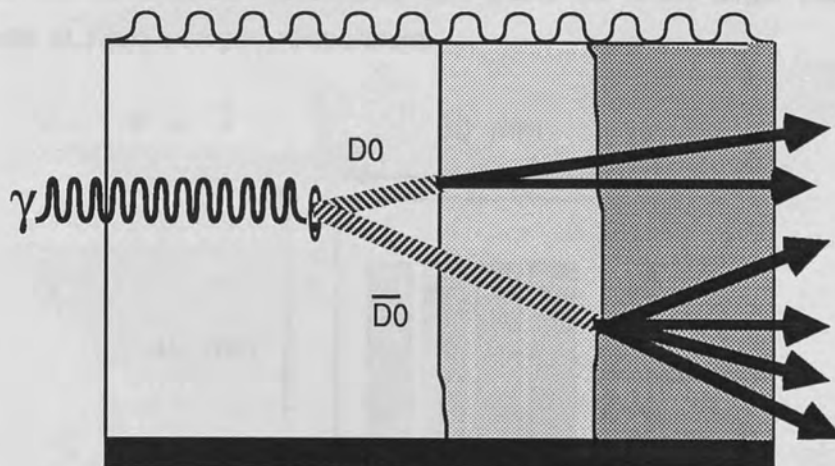


Figure 2.6: schematic section through the Ge monolith. The shaded regions represent the charge cloud in the detector bulk, the darker the shading the greater the density of charge carriers.

Since the target is to be placed in a photon beam, the total radiation length of the device must be kept low. At the same time, it is desirable to measure at least two mean lifetimes of the particle under study, which corresponds to $\sim 12\text{mm}$ for a mean lifetime of $4 \times 10^{-13}\text{s}$ at a gamma factor of 50. A 12mm target constructed only of a continuous germanium crystal would present approximately 50% of a radiation length to the beam. In order to keep the total radiation length at the order of 20%, therefore, a 5mm thick germanium target is followed (after a gap of 1.2mm) by fifteen planes of silicon, the first eight spaced at $200\mu\text{m}$ and the following seven at $400\mu\text{m}$.

The silicon detectors are $200\mu\text{m}$ thick with an active area of $20 \times 20\text{mm}^2$. They were manufactured using the planar technique i.e. oxide passivation and boron ion bombardment at 10-15 KeV, to form the pn junction. To reduce the overall capacitance each silicon plane was divided into four sections $5 \times 20\text{mm}^2$ spaced at $100\mu\text{m}$ (see figure 2.7), giving an intrinsic capacitance at the contact of approximately 55pF per section [RANCOITA 82].

With this target design, where most of the production occurs in the germanium (with a probability of 6:1), an approximately constant precision is maintained, with short decay lengths well resolved in the high granularity sector, and longer decay lengths in the sector with greater pitch. In order to reduce the noise due to the thermal excitation of electron hole pairs, the whole target was placed in a cryostat at liquid nitrogen temperature.

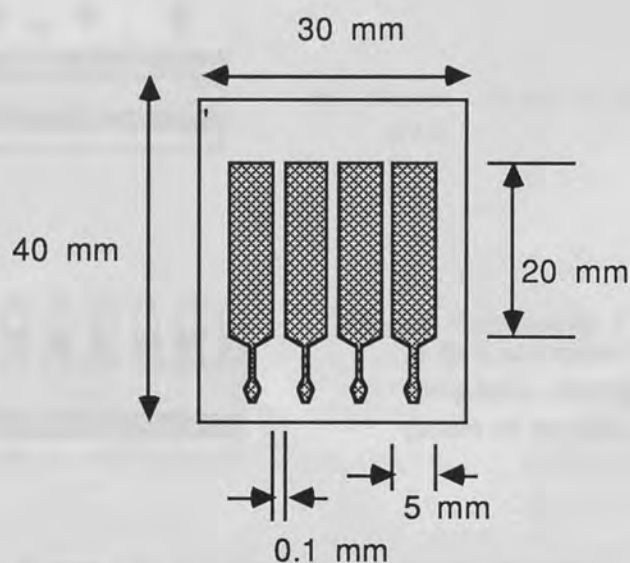


Figure 2.7: detail of the silicon detectors

the active target

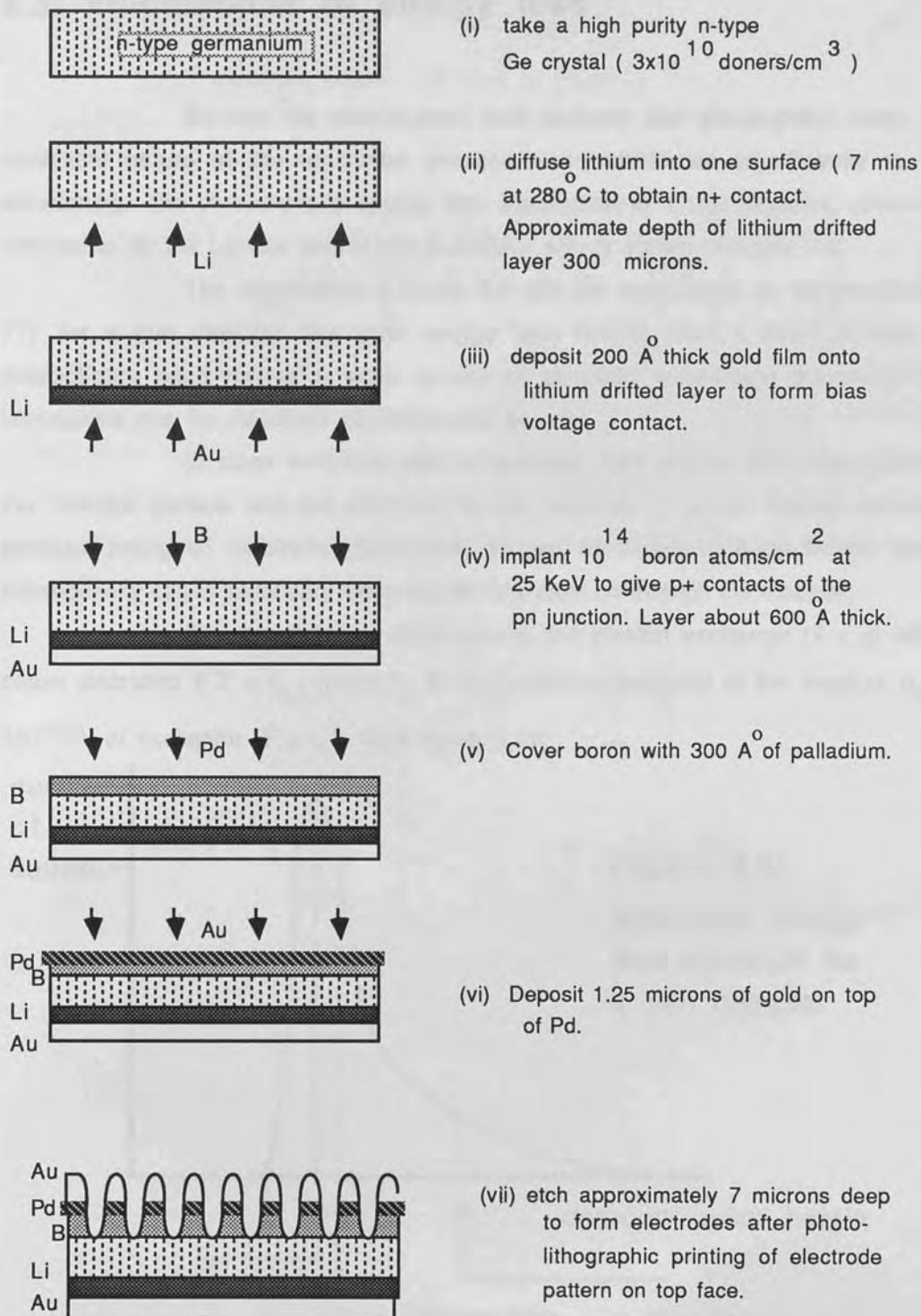


Figure 2.8: Recipe for germanium monolith

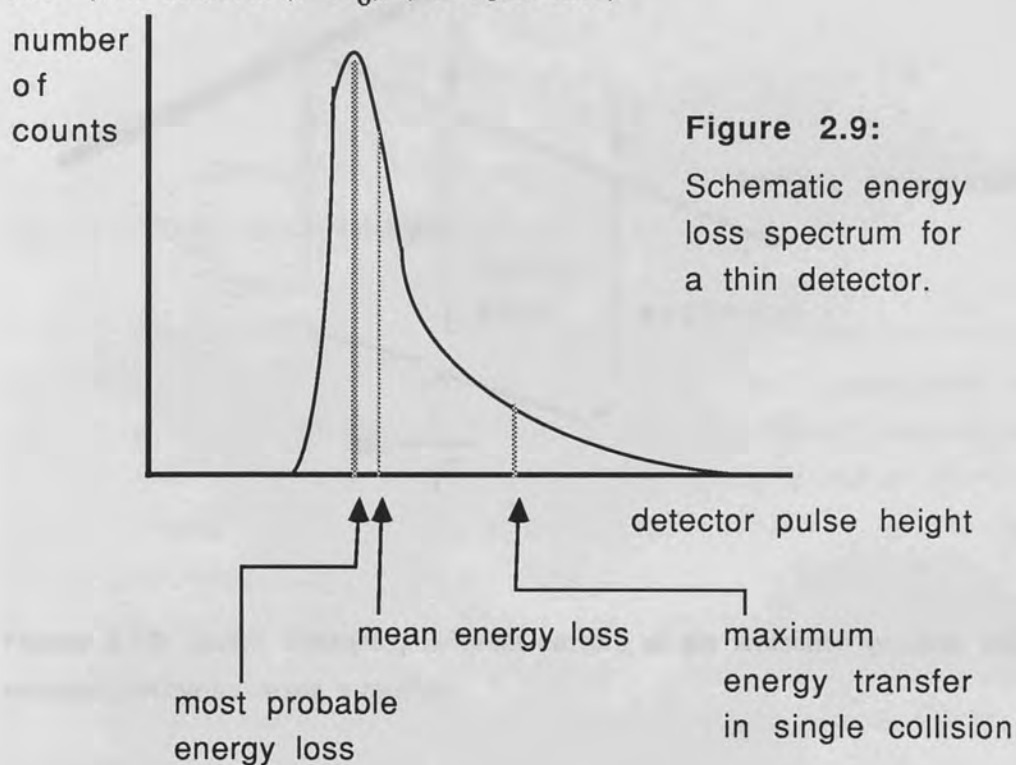
2.3: Fluctuations of energy loss

Besides the contributions from detector and pre-amplifier noise, the statistical nature of the ionization process also contributes significantly to line broadening. The characteristic energy loss distribution in a thin detector, commonly referred to as the Landau distribution [LANDAU 44], is shown in figure 2.9.

The distribution in figure 2.9 can be understood as follows [SAULI 77]: for a thin detector, the total energy loss results from a small number of interactions, each having a wide spread of possible momentum transfers. The interactions may be classified into two broad groups:

(i) close collisions due to relatively hard photon exchange between the incident particle and the electrons in the medium. ($T > \eta$). These collisions produce energetic electrons (historically known as δ -rays or δ -electrons) which subsequently cause secondary ionization as they pass on through the medium;

(ii) long distance collisions via soft photon exchange ($T < \eta$) which cause ionization if $T > I_0$, where I_0 is the ionization potential of the medium ($I_0 \sim 16Z^{0.9}$), or excitation ($T < I_0$). (see figure 2.10)



In general, the energy loss is given by the Bethe-Bloch formula, corrected for density effects:

$$\frac{dE}{dx} = \frac{4\pi e^4 N Z}{m_e c^2 \beta^2 A} \cdot \rho \left[\ln \left(\frac{2 m_e \gamma^2 \beta^2 c^2}{I_0(Z)} - D \right) - \beta^2 \right] \quad (2.6)$$

The long tail in figure 2.9 is therefore due to one or more δ -electrons depositing significantly above average energy in a single strip. The problem is compounded for telescopes of thin detectors at small pitch by δ -electrons crossing from one strip to adjacent strips, thereby smearing or obscuring the spatial information. There was a probability of a few % of a δ -ray occurring in a target strip, per minimum ionizing particle.

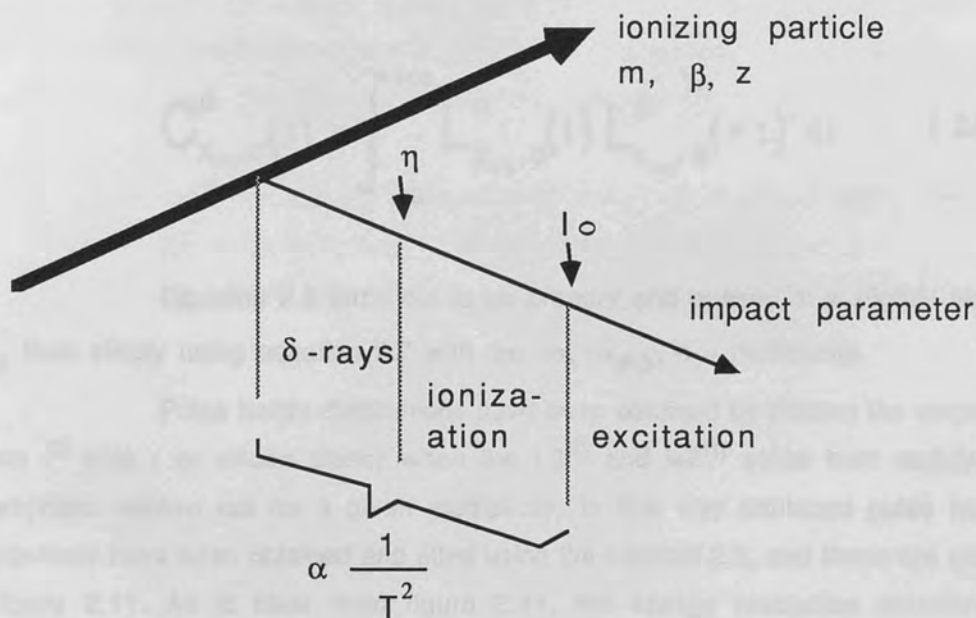


Figure 2.10: sketch illustrating different sectors of the ionization process when a charged particle traverses a medium.

The single minimum ionizing particle energy loss spectrum may be

approximated by the Moyal function [MOYAL 55], which reproduces the essential features of the Landau distribution:

$$L_{x_{mp}, \sigma}^{\alpha} = A_{\sigma}^{\alpha} e^{-\alpha \left(\frac{x-x_{mp}}{\sqrt{\alpha} \sigma} + e^{-\frac{x-x_{mp}}{\sqrt{\alpha} \sigma}} \right)} \quad (2.7)$$

where x is the energy loss, x_{mp} is the most probable energy loss, σ is the variance, and α is a shape parameter, and

$$A_{\sigma}^{\alpha} = \frac{\alpha^{(\alpha-\frac{1}{2})}}{\sigma \Gamma(\alpha)}$$

is the normalisation. Higher multiplicity energy loss distributions are obtained from the convolution of equation 2.7:

$$C_{x_{mp}, \sigma}^{\alpha}(x) = \int_{-\infty}^{+\infty} L_{x_{mp}, \sigma}^{\alpha}(t) L_{x_{mp}, \sigma}^{\alpha}(x-t) dt \quad (2.8)$$

Equation 2.8 turns out to be broader and peaked at a slightly higher x_{mp} than simply using equation 2.7 with $n\alpha$, $n\sigma$, nx_{mp} , n = multiplicity.

Pulse height distributions have been obtained by plotting the response of the i^{th} strip (or silicon plane) when the $i-2^{\text{th}}$ and $i+2^{\text{th}}$ strips both satisfy an appropriate window cut for a given multiplicity. In this way unbiased pulse height distributions have been obtained and fitted using the function 2.8, and these are shown in figure 2.11. As is clear from figure 2.11, the energy resolution deteriorates rapidly for higher multiplicities. This makes the choice of the discriminator cut in the analysis software crucial, as we shall see.

For the purpose of the NA1 experiment, the natural unit of the target pulse height is the most probable energy deposit in a detector by a minimum ionizing particle. The target pulse heights for each strip were therefore calibrated in mips via the relationship:

the active target

$$n_{\text{mip}} = \frac{Ph_n - Ph_0}{Ph_2 - Ph_0} \quad (2.9)$$

where Ph_0 and Ph_2 are the most probable number of ADC counts for zero (pedestals) and two minimum ionizing particles respectively.

The relative consistency of the target response and calibration has been ascertained by plotting together the sum of the pulse heights (with any saturation effects unfolded) in each strip (see example in figure 2.12), for each data taking period. This involves an average over a combination of various non-trivial production and decay distributions, the quantitative behaviour of which is not known. Nonetheless, the expected qualitative behaviour is that the average multiplicity will increase with detector number (the first active strip is detector number one, and so on), that is, with depth into the target. From figure 2.12 it can be seen that this increase is approximately linear for the germanium monolith but for the silicon no definite conclusion can be drawn, due to the inhomogeneous spacing of the detectors and the effect of the gaps. Deviations from the linear form are due to either:

- (a) a detector not functioning for part or all of a data taking period;
- (b) a low efficiency for a particular detector;
- (c) a poor calibration of a strip.

Figure 2.12: Plot of the sum of the pulse heights in each strip versus strip number for the germanium monolith and the silicon detector.

the active target

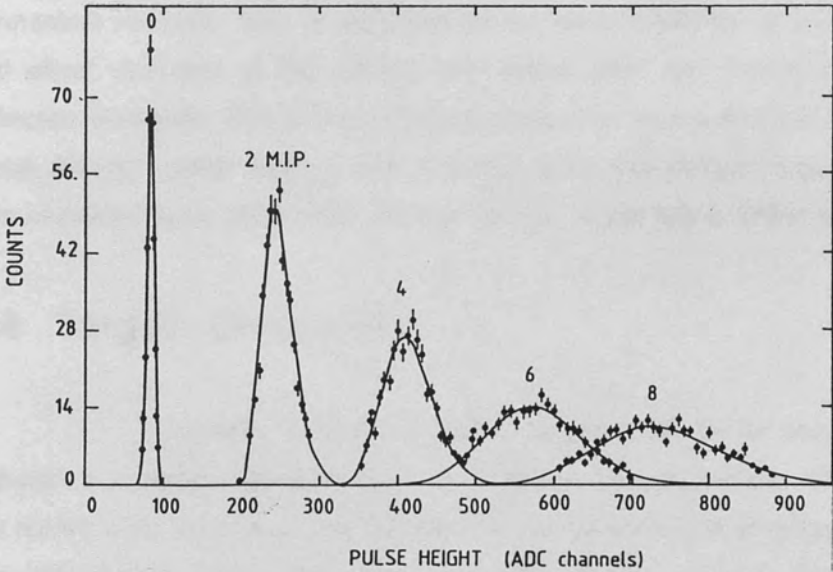
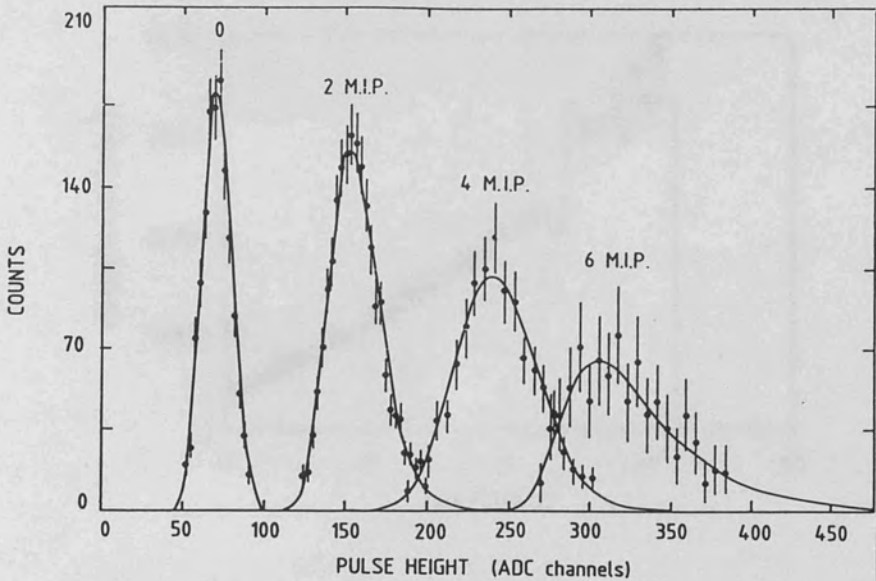


Figure 2.11: Pulse height distributions for the target. Top, 50µm pitch version; bottom, 100µm pitch version.

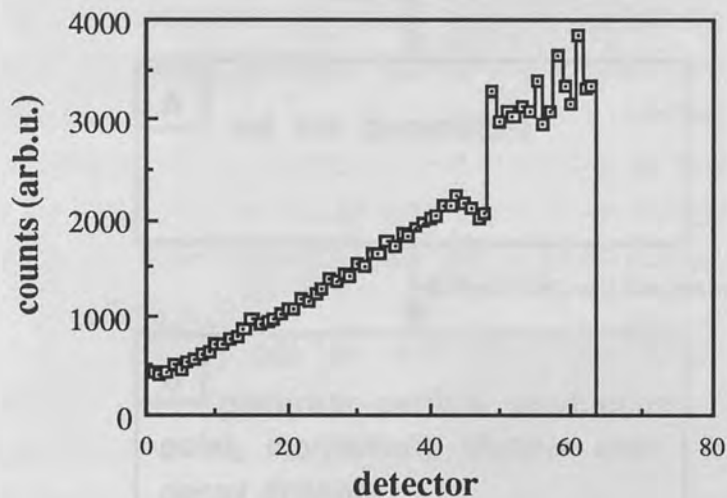


Figure 2.12: period 1b sum of pulse height of target detectors.

Occurrences of non-functioning detectors were known and taken into account as appropriate. This leaves the only significant deviation at the end of the germanium monolith. This is attributed to the lower efficiency of these strips due to end effect distortion of the electric field which drifts the charge carriers onto the collection electrode. This trend was compensated for in the analysis by renormalising these detector pulse heights with a small factor determined from the appropriate sum-of-pulse-height distribution for the period, assuming a linear behaviour.

2.4 Target Simulation

In order to study the performance of the target and of the scanning software a simulation program (the GS monte carlo) was written. The program uses the monte carlo technique [JAMES 68], i.e. the behaviour is assessed by integrating over the diverse contributing processes using random numbers generated from the probability distributions appropriate to each process. In the limit of a large number of generated events the simulation converges on the behaviour of the real system. The program has been written in modular form. For clarity the gross structure of the GS simulation program is shown in figure 2.13, in reality each box represents a number of program units.

the active target

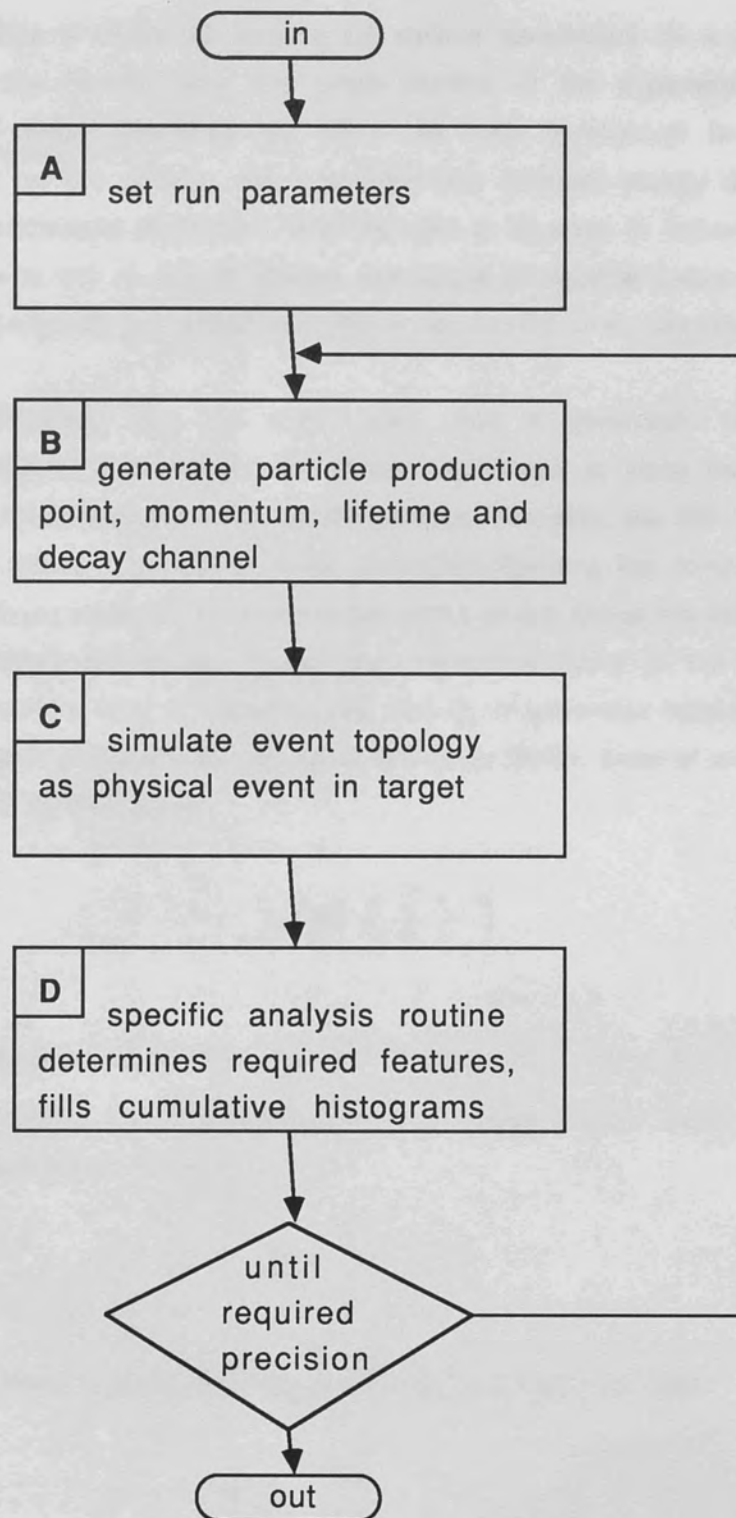


Figure 2.13: principal operations in the GS simulation program.

the active target

Box A allows the user to set various parameters for a given run. These include the particle type, the mean lifetime of the exponential decay distribution, the target geometry (eg 48 or 96 strip germanium target), the branching ratios for the particle, the bremsstrahlung (photon) energy distribution or the particle momentum distribution. Also included is an array of logical switches allowing the user to turn on and off various simulations of physical processes in the target, such as δ -electron production and photon conversion of the photons from π^0 decay.

Entering into the event loop, box B generates the event characteristics. Since it is not the aim of this experiment to study the detailed production and dynamical properties of the charmed particles, the GS simulation program uses a simple approach to event generation, ignoring the complexities of QCD, and for the purposes of the analysis presented in this thesis the approximate treatment is entirely satisfactory. First, the production point in the target is generated. This may be fixed in a specific strip (box A), or generated according to the following prescription [HUGHES 85]: the intensity I of the photon beam at a depth x in the target is given by the relation

$$I = I_0 \exp\left(-\frac{7}{9} \frac{x}{x_R}\right) \quad (2.10)$$

where x_R is the radiation length and I_0 the normalisation. Additionally the relative rate of photoproduction in the germanium to the silicon is required. If the production rate R is

$$R \propto N \sigma(\gamma \rightarrow X) \quad (2.11)$$

where N is the number of particles/unit area in the target

$$N = \frac{N_A}{A} \rho t \quad (2.12)$$

(N_A is the Avagadro constant, A the atomic number, ρ the density and t the thickness of material) and assuming an A dependence of $A^{2/3}$ for the

the active target

photoproduction cross section $\sigma(\gamma \rightarrow x)$, we arrive at the relative rate of photoproduction for unit thickness

$$\frac{R_{\text{Ge}}}{R_{\text{Si}}} = \left(\frac{A_{\text{Ge}}}{A_{\text{Si}}} \right)^{\frac{1}{3}} \frac{\rho_{\text{Ge}}}{\rho_{\text{Si}}} \quad (2.13)$$

Finally, the production position is generated from the following distribution

$$F(x) = \begin{cases} \exp(-7/9) \cdot (x/X_{R,\text{Ge}}) & ; x \leq T \\ l' \cdot R_{\text{Si}}/R_{\text{Ge}} \cdot \exp(-7/9) \cdot (x/X_{R,\text{Si}}) & ; x > T \end{cases} \quad (2.14)$$

where T is the end of the germanium and l' is the beam intensity at T . The production distribution is shown in figure 2.14, where the horizontal coordinate is strip number. Note that the silicon strips are twice as thick as the germanium strips.

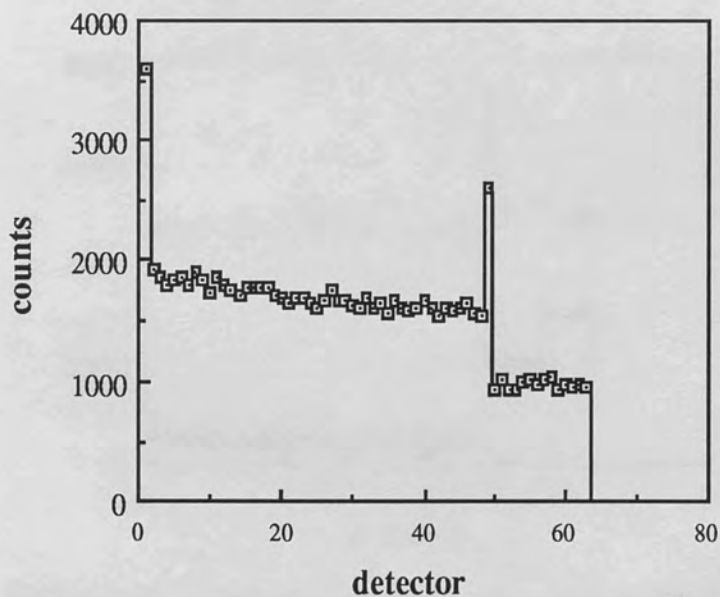


Figure 2.14: photoproduction distribution in the NA1 target (simulation).

the active target

Clearly visible are the steady decrease in production due to the radiation length of the target, and the relative photoproduction cross-sections of germanium and silicon. The abscissae in figure 2.14 is the detector or strip number, and care must be taken not to confuse this with distance from the start of the target. In addition it must be remembered that the silicon detectors (detector numbers 49 onwards) are twice as thick as the germanium strips in this case (48 strip germanium block). The large peaks in the distribution are due to the first and last inactive germanium strips, the production in which is only observed in the next down beam detector.

The relationship of the inhomogeneous geometry to the detector number is best illustrated in figure 2.15, where a uniform random distribution between the start and end of the target has been transformed into the detector number in which it would be observed. This shows the first and last dead germanium strips, and the effect of the different pitches in the target. Note that figure 2.15 includes the spaces between the silicon planes, and thus represents a flat decay distribution where a particle can decay in flight in the gaps, in contrast to the distribution in figure 2.14 where production may only occur on the material of a detector. Thus the large peak in figure 2.15 includes the 1.2mm gap between the germanium and the silicon.

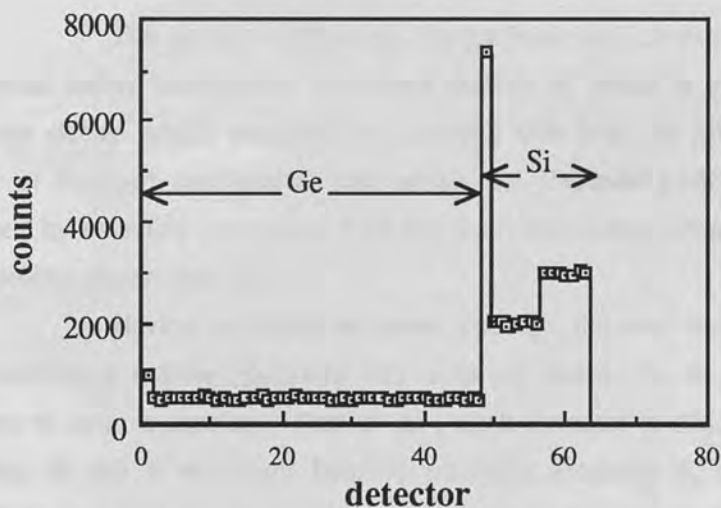


Figure 2.15: a uniform decay distribution seen by the NA1 target (see text).

Kinematics of the particles produced are generated either from a known distribution or by an approximate model. In the former case, the energies of the particles are selected from, for example, the measured energy distribution for D

mesons obtained in the exclusive analysis, shown in figure 2.16. In the latter case a photon, with energy generated from an appropriate $1/E$ bremsstrahlung distribution, converts into an intermediate Ψ vector resonance, which is immediately decayed using the CERN Library routine Genbod (n-body monte carlo generator) into the desired charmed particles, for example $\gamma \rightarrow \Psi'' \rightarrow D$ anti-D.

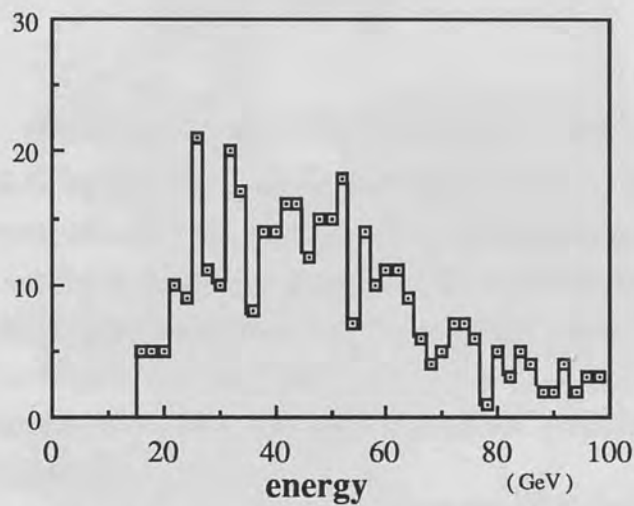


Figure 2.16: D^0 energy spectrum from exclusive analysis.

The proper lifetimes of the particles are generated according to the exponential decay distribution, the mean lifetime of which is set (box A), and the laboratory decay length obtained by boosting this into the laboratory frame. The number of charged secondaries into which the charmed particle decays is either generated by selecting at random from the input branching ratios, or may be fixed at the beginning (again, box A).

Having generated an event topology, the next step is to transform this in as realistic a manner possible into a target event, i.e. to simulate the target response to such a topology. First of all, each detector is allocated a pulse height according to the n minimum ionizing particles crossing it, generated from the appropriate n -particle energy loss spectrum. These spectra were obtained using the window cut described on page 57. Special attention is paid to detectors containing production and decay points: a fraction of the n -particle energy loss is used according to the distance into the detector at which the multiplicity increment occurs.

If the difference between the actual energy loss and the most probable

the active target

energy loss is above a given threshold, i.e. $dE/dx - dE/dx_{mp} > \eta$, then a δ -electron is considered to have been produced. The threshold η is set by the granularity of the detector: the δ -electron must have sufficient energy to traverse the detector to justify specific treatment. The effective range of a δ -electron is [SAULI 77]:

$$R_{\text{eff}} = 0.71 \frac{E^{1.72}}{\rho} \quad (2.14)$$

where R_{eff} is in cm if E is in MeV and ρ in g/cm^3 . Thus the thresholds are $\eta = 148$ KeV for the $100\mu\text{m}$ germanium target and $\eta = 137$ KeV for a silicon plane. If the threshold cut is satisfied then the most probable energy loss is used in that detector and the δ -electron is propagated in a random direction (the original angle is soon lost in multiple scatters), and the secondary energy deposit added to the ionization in the relevant detector. This is an important process to simulate since a δ -electron crossing more than one strip can smear the multiplicity information delivered by the target.

A further source of background considered is the conversion of photons from π^0 decay, since these cause increments in ionization which may be misidentified as charm decays. The probability of conversion is calculated using the radiation length, see equation 2.10.

An example of a simulated target event is shown in figure 2.17, and should be compared with examples of real target events in figure 4.22.

Box C contains the analysis routines for a specific task. These will be outlined in the thesis whenever the results of a particular analysis are presented. The format of the final generated event is also cast in an identical way to that of the real target events to facilitate the integration and testing of the target scanning software.

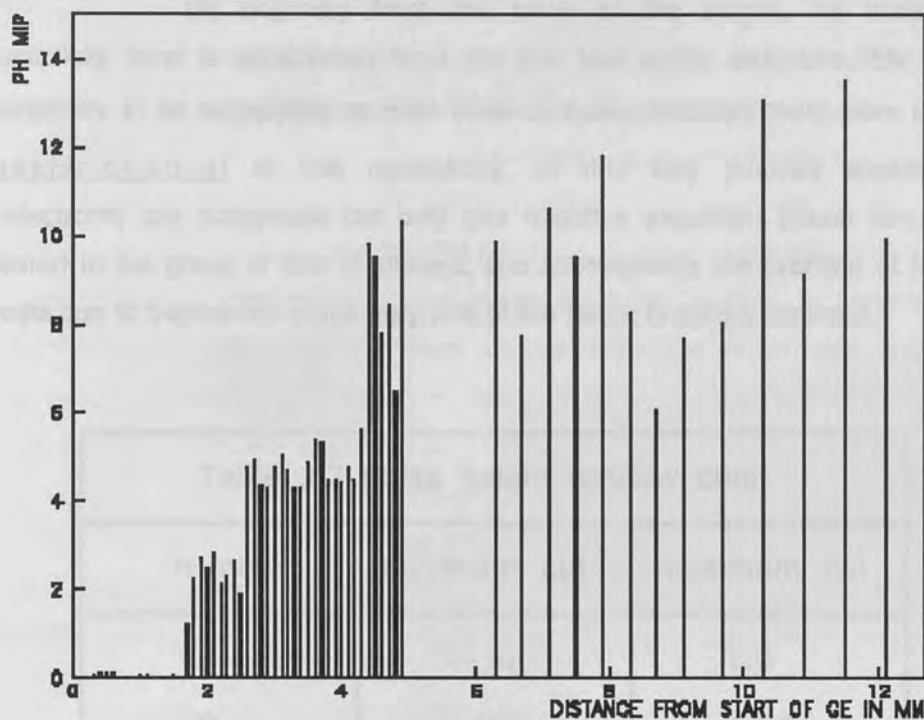


Figure 2.17: An example of a monte carlo generated target event.

2.5: The target scanning software

Central to the target analysis is the routine which scans each target event and establishes the topology. The ability to scan with acceptable efficiency, reasonable computer time and without human bias large numbers of decay topologies is crucial to the NA1 technique for electronically measuring charm lifetimes, and in this sense represents a major departure from the more traditional visual techniques, namely bubble chamber and emulsion targets. The algorithm for target scanning discussed below is different from that presented elsewhere [SACKS 87], and combines the advantage of higher efficiency with reduced execution time.

The essential elements of the target scanning algorithm are as follows:

(i) a best estimate $\langle Ph_n(i) \rangle$ of the number of minimum ionizing particles in each detector is obtained by testing whether the calibrated detector pulse height falls in the window cuts defined from the n -particle dE/dx distributions in table 2.3.

the active target

(ii) beginning from the back of the target, an initial starting multiplicity level is established from the first four active detectors. For a starting multiplicity to be acceptable at least three of these detectors must have a $\langle Ph_n(i) \rangle$ greater-or-equal to this multiplicity. In this way positive excursions (eg δ -electrons) are acceptable but only one negative excursion (much rarer than the former) in the group of four is allowed, and subsequently the problem of falsely high levels due to δ -electrons at the very end of the target is greatly reduced.

n mips	minimum cut	maximum cut
0	-1.0	1.0
2	1.0	3.25
4	3.25	5.35
6	5.35	7.5
8	7.5	12.0
saturation	12.0	-

(iii) Proceeding from this initial starting level at the back of the target towards the front, successive detector $\langle Ph_n(i) \rangle$'s are tested for consistency with this level. If two adjacent detector $\langle Ph_n(i) \rangle$'s are less-than this level then a change in multiplicity is accepted and a new current level defined. The request of two adjacent detectors with a lower $\langle Ph_n(i) \rangle$ than the current level allows multiplicity changes to be defined without confusion with isolated negative excursions deriving from the energy loss distribution. The program continues in this way until the front of the target is reached. The chosen direction of progression along the detector telescope has been made so that the program can 'cut under' positive excursions in levels due to δ -electrons, once an initial level choice has been made.

the active target

(iv) Various quality cuts are applied to the located levels. Each level is required to be at least three detectors in length, not including negative excursions, in order to be defined as stable. If a level is defined as unstable then it is considered as part of the adjacent lower level. In addition quality cuts are applied to the event as a whole. A zero level consistency test on the three detectors following the first is made, to ensure that the production occurred inside the target and not, for example, on the cryostat window. (The first strip is not used to avoid end effect bias). A test on the percentage of saturated detectors is made: if 50% or more detectors in non-zero levels saturated then the event was rejected.

(v) Using the information obtained in (iii) which passed the filter (iv) the topology of the target event is established and written to the output common block. This information consists essentially of the number of levels, and the initial detector and multiplicity of each level, from which the level length and multiplicity increment can be deduced.

The statistics of the target scanning program for events (with at least four charged tracks in the spectrometer) for each period are presented in table 2.4 below, where the topology 0-2-6, for example, indicates an event with three levels, the first of multiplicity 0, the second of 2 and the third of 6. All percentages quoted in table 2.4 are of the total event sample used in a period. Note that the classifications 'flat target' (ie no changes in multiplicity), 'no zero level' and 'noisy' (i.e. more than 50% saturation) for rejected events are not mutually exclusive. The performance of the targets can be seen to be consistent across periods 1B, 2A, 2B, and 2C which all used the 48 strip Ge version, whilst period 5A, which used the 96 strip Ge version, operated with greater efficiency, mainly due to less saturation in dealing with high multiplicity events.

the active target

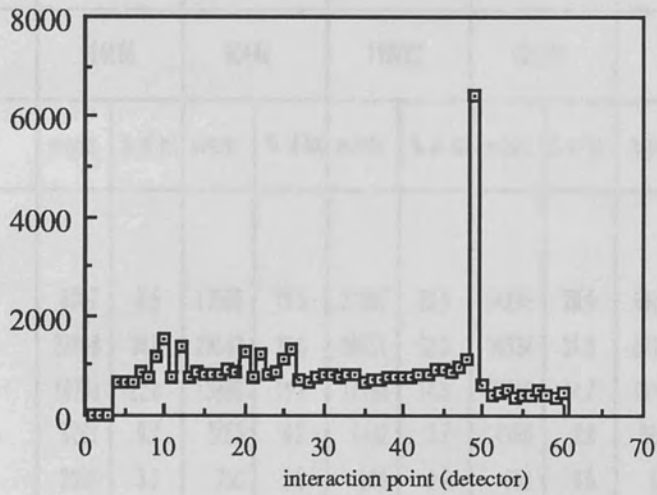


Figure 2.18a: period 2B distribution for the first step found by the scanning software.

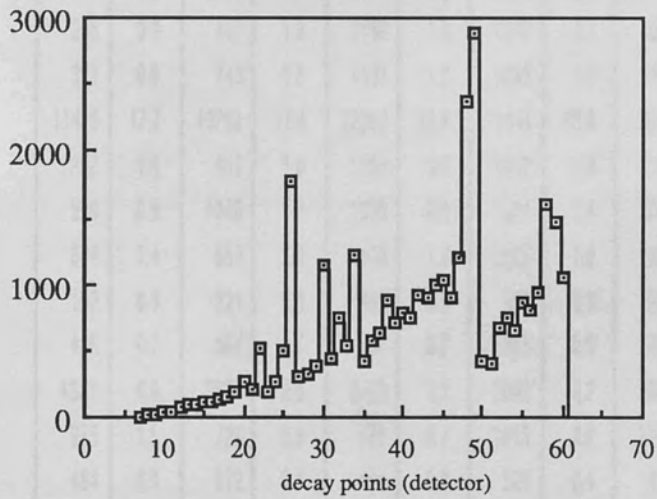


Figure 2.18b: period 2b distribution for the second and third steps found using the scanning software.

the active target

PERIOD	5A		1B		2A		2B		2C		ALL	
Total events	64668		90146		119282		121391		96446		491933	
Classification	events	% of tot	events	% of tot	events	% of tot	events	% of tot	events	% of tot	events	% of tot
<u>Steps</u> <u>Levels</u>												
0 1	6307	9.8	17569	19.5	23987	20.0	24285	20.0	18254	18.9	90402	18.4
1 2	22018	34.0	29342	32.6	38651	32.0	38334	31.6	27135	28.0	155480	31.6
2 3	14768	22.8	13886	15.4	17199	14.0	17782	14.7	14140	14.7	77775	15.8
3 4	6261	9.7	3753	4.2	4442	3.7	4666	3.8	3944	4.1	23066	4.7
4 5	2092	3.2	700	0.8	849	0.7	952	0.8	686	0.7	5279	1.1
<u>Recognized topologies</u>	44901	69.0	47674	53.0	60785	51.0	61734	51.0	45901	48.0	262996	53.5
0 - 2	18948	29.3	24973	27.7	32839	27.5	31934	26.3	22513	23.0	131207	26.7
0 - 4	1906	3.0	2759	3.0	3519	3.0	3810	3.1	2747	2.9	14741	3.0
0 - 6	555	0.9	867	1.0	1162	1.0	1342	1.1	983	1.0	4909	1.0
0 - 8	371	0.6	743	0.8	1131	1.0	1248	1.0	886	0.9	4379	0.9
0 - 2 - 4	11415	17.7	10233	11.4	12398	10.4	12444	10.3	9141	9.5	55631	11.3
0 - 2 - 6	1232	1.9	917	1.0	1051	0.9	1112	0.9	1121	1.7	5433	1.1
0 - 2 - 8	599	0.9	1040	1.2	1029	0.9	1681	1.4	2001	2.1	8351	1.7
0 - 4 - 6	884	1.4	884	1.0	1138	1.0	1227	1.0	809	0.8	4942	1.0
0 - 4 - 8	192	0.3	221	0.3	345	0.3	350	0.3	365	0.4	1473	0.3
0 - 6 - 8	446	0.7	584	0.7	882	0.7	968	0.8	703	0.7	3583	0.7
0 - 2 - 4 - 6	4371	6.8	2337	2.6	2772	2.3	2663	2.2	1985	2.1	14128	2.9
0 - 2 - 4 - 8	975	1.5	726	0.8	772	0.7	1018	0.8	1175	1.2	4666	1.0
0 - 2 - 6 - 8	488	0.8	372	0.4	404	0.3	526	0.4	492	0.5	2282	0.5
0 - 4 - 6 - 8	427	0.7	318	0.4	494	0.4	459	0.4	294	0.3	1992	0.4
0 - 2 - 4 - 6 - 8	2092	3.2	700	0.8	849	0.7	952	0.8	686	0.7	5279	1.1
<u>Rejected events</u>	19767	31.0	42472	47.0	58497	49.0	59657	49.0	50545	52.0	228937	46.5
flat target (no steps)	6307	9.8	17569	19.5	23987	20.1	24285	20.0	18254	18.9	90407	18.4
no zero level	9065	14.0	25207	28.0	32796	27.5	34468	28.4	32258	33.5	133794	27.2
noisy	4644	7.2	23141	25.7	33457	28.1	34388	28.3	27212	28.2	122842	25.0

Table 2.4: (previous page) target event statistics

2.6: Scanning efficiency

The scanning efficiency of the software was established using two independent methods:

(i) using the GS target simulation in conjunction with the scanning program;

(ii) by a visual scan of a random sample of events in each period.

Method (i) is free from human bias but only reliable so long as the simulation realistically mirrors the data. The results of the analysis of one hundred thousand simulated events using the scanning program described in section 2.5 above are presented in table 2.5. The events were generated according to the energy spectrum of figure 2.16, the production distribution of figure 2.14, a mean lifetime of 4.0×10^{-13} s, and the δ -ray routine where appropriate, but with the $\pi^0 \rightarrow \gamma\gamma$; $\gamma \rightarrow e^+e^-$ routine disabled. Efficiencies for the principal topologies expected to be of interest in charm events are also shown.

Table 2.5 illustrates the high efficiency of the scanning software for recognizing a wide variety of topologies. As expected, the simplest events have the highest detection efficiency, but nevertheless for the more complicated topologies involving two or three changes in multiplicity the detection efficiency stabilises around 80%. With respect to individual topologies of, for example, events with two changes in multiplicity inside the target volume, the lower multiplicity events and the events where the multiplicities are well separated (eg 0-4-8) are most efficiently recognized, a result anticipated in section 2.3 from consideration of the separation of the different multiplicity distributions in figure 2.11. The column 'found to +-1 strip' contains the statistics for the case where the event was 'very well recognized', i.e. the number of steps, the multiplicity of the steps and the position of the steps (to within +-1 detector) found were exactly as generated by the simulation program.

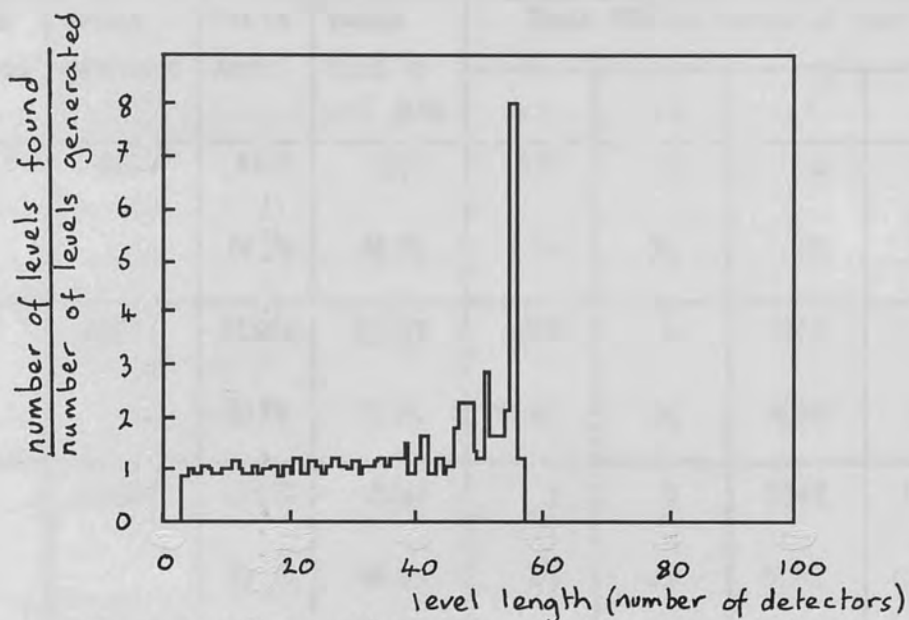


Figure 2.19: "efficiency" for finding levels of length n detectors.

The "efficiency" for *resolving levels of length n detectors* is shown in figure 2.19, which has been obtained by dividing the distribution of level lengths found using the analysis software by the distribution of generated level lengths. Large statistical fluctuations occur for long level lengths due to the low statistics at these lengths (eg level length > 40 detectors), and the tendency for the program to confuse a δ -ray at the end of the target with a genuine change in multiplicity. This effect has been reduced using the criterion for four stable detectors at the rear of the target for an initial starting level (section 2.5). However, there is a play-off between this effect and retaining a sufficient fiducial volume in order that the final result has a small error (see Chapter 4).

Table 2.5: (following page) target scanning efficiency as determined with the simulation program

the active target

number of steps	events generated	events found	events found to +- 1 strip	found different number of steps			
				+ 1	+ 2	- 1	- 2
1	6834	6444	5352	388	2	0	0
		94.3%	78.3%	5.7%	0%	0%	0%
2	43081	35620	23783	4635	0	2826	0
		82.7%	55.2%	10.8%	0%	6.6%	0%
3	21079	17422	9888	0	0	3542	115
		82.7%	46.9%	0%	0%	16.8%	0.6%
Topology		Events generated		Events found		Events found to +1 strip	
0 - 2		2737		2650 96.8%		2286 83.5%	
0 - 4		4097		3462 84.5%		3462 74.8%	
0 - 2 - 4		5190		4569 88.0%		4356 83.9%	
0 - 2 - 6		6385		4063 63.6%		3794 59.4%	
0 - 4 - 6		6527		4341 66.5%		3140 48.1%	
0 - 4 - 8		19626		16668 84.9%		10234 52.1%	
0 - 6 - 8		5353		4127 77.1%		2259 42.2%	
0 - 2 - 4 - 8		4165		3546 85.1%		2873 69.0%	
0 - 2 - 6 - 8		8407		6656 79.2%		3703 44.1%	
0 - 4 - 6 - 8		8507		6699 78.8%		3312 38.9%	

the active target

What this level length efficiency means in terms of finding decay times is assessed by passing the level lengths found by the scanning program along with the momenta of the generated particles to the analysis routine which calculates the proper time according to equation 2.2. This time efficiency was obtained by dividing the distribution of measured proper times by the distribution of generated proper times, and is shown in figure 2.20a. Again, poor statistics result in large fluctuations at long proper times, but the principal features are a loss of efficiency at short lifetimes due to the finite target granularity, and a tail off of efficiency at long lifetimes due to the finite dimensions (length) of the target. Such effects can be compensated for in fitting the data to an exponential function, as discussed fully in chapter 4. When the effects of the minimum observable decay length (i.e. three strips) and the maximum observable decay length are unfolded, i.e. events are generated only within these limits, the time efficiency is as shown in figure 2.20b. The time efficiency with known effects unfolded is essentially flat, to within 3%, illustrating the low bias and high efficiency of the target scanning software.

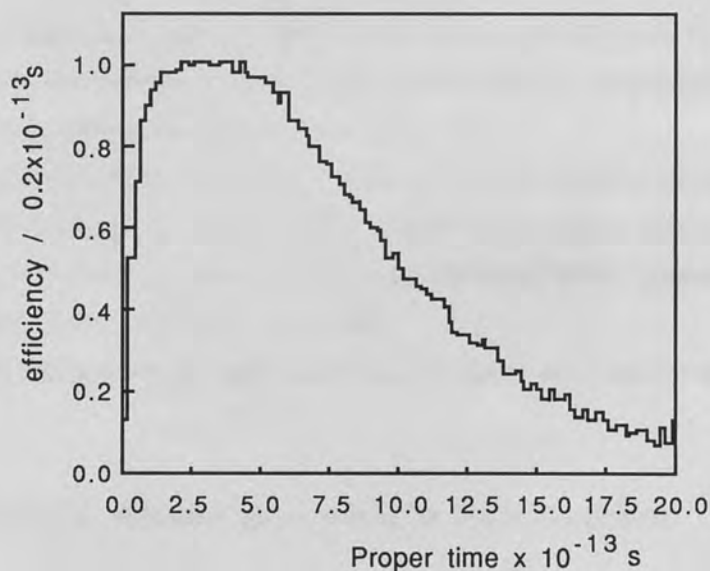


Figure 2.20a time efficiency using the target scanning software

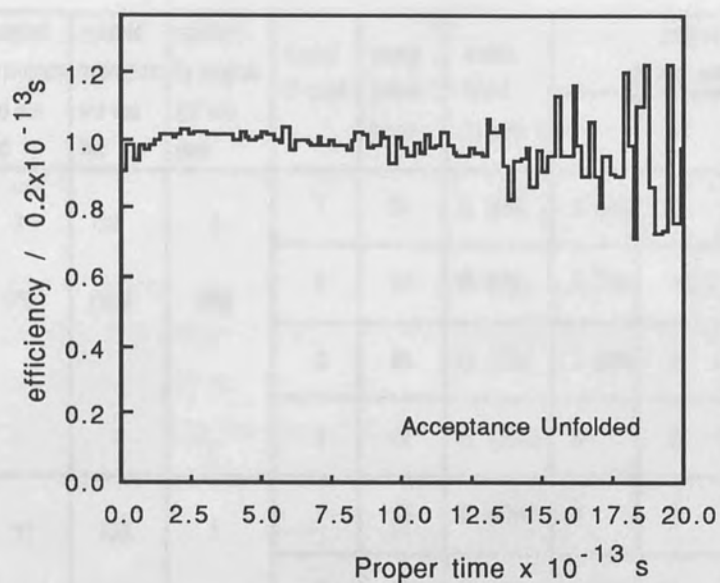
the active target

Figure 2.20b: the same efficiency with max-min effects unfolded (see text).

The efficiency of the target scanning software has been independently assessed by visual scanning of random events from each period. In order to reduce the time required to examine batches of events and yet still achieve reasonably significant statistics the following simple categories were looked for:

- (a) the program rejected the event and it was indeed a bad event;
- (b) the program rejected what appeared to be a good event;
- (c) the program recognized as good an event which appeared to be a good event when scanned visually;
- (d) the program recognized as good an event which looked bad.

Table 2.6: (following page) results of target visual scan

the active target

period	accepted by program and was good	accepted by program and was bad	rejected by program and was bad	rejected by program and was good	number of steps	events judged by eye	events found by prog+ 1	program found a different number of steps			
									+2	- 1	-2
5 A	165 (60%)	3 (1%)	104 (38%)	3 (1%)	1	64	55 (86%)	9 (14%)	0	0	0
					2	59	49 (83%)	9 (15%)	1 (2%)	0	0
					3	30	23 (77%)	7 (20%)	0	0	0
					4	12	12 (100%)	0	0	0	0
1 B	110 (40%)	11 (4%)	153 (56%)	1 (0%)	1	45	45 (100%)	0	0	0	0
					2	43	40 (93%)	3 (7%)	0	0	0
					3	19	17 (90%)	2 (11%)	0	0	0
					4	3	3 (100%)	0	0	0	0
2 A	98 (36%)	4 (2%)	171 (62%)	2 (1%)	1	53	49 (93%)	4 (8%)	0	0	0
					2	35	32 (91%)	3 (9%)	0	0	0
					3	10	9 (90%)	1 (10%)	0	0	0
					4	0	0	0	0	0	0
2 B	104 (38%)	6 (2%)	164 (60%)	1 (0%)	1	49	44 (90%)	5(10%)	0	0	0
					2	42	41 (98%)	1(2%)	0	0	0
					3	13	10 (77%)	1 (8%)	0	1(8%)	0
					4	0	0	0	0	0	0
2 C	80 (29%)	14 (5%)	176 (64%)	5 (2%)	1	46	43 (94%)	2 (4%)	1 (2%)	0	0
					2	27	21 (77%)	5 (19%)	1 (4%)	0	0
					3	6	3 (50%)	3 (50%)	0	0	0
					4	1	1 (100%)	0	0	0	0

The events accepted by the program which appeared good were further examined as to whether the program had recognized the correct number of steps. The result of this visual scan is presented in table 2.6. The first four columns give the general performance of the scanning program, the percentages quoted being of the total events scanned (275 events from each period). The proportion of accepted events judged good by visual scan is in general agreement with the figures in Table 2.4 (total target statistics), the notable feature being that period 5A (96 strip Ge) has a higher proportion of 'good' events.

The loss due to the program rejecting an event which appeared good is approximately 1% of the total sample, or about 2% of the good events in the sample. The scanning program accepted bad events as good at a level of 3% in the total sample, or about 5% of the bad events in the sample. These figures are acceptable insofar as they ensure negligible loss of data and do not introduce a large background when the target topology selection is applied to the data.

The right-hand side of Table 2.6 shows the breakdown of those events 'accepted by program and were good' in terms of the number of multiplicity changes (steps) in the event. In this case the percentages are the scanning efficiencies i.e. the number of the events recognised by visual scan that were also recognised as events *with the same number of steps* by the program. Also shown are the cases where the program did not recognise the event and in almost all cases this was due to the program inventing an extra step.

Bad events were also examined during the visual scan to assess the reason for their rejection. For the most part these events were either saturated, empty, or had no stable zero level, i.e. that the production was in the target could not be guaranteed. Examples of bad target events are displayed in figure 2.21, and statistics for the reason the bad events were rejected in table 2.7. Again these are in agreement with the results from the scanning program in table 2.4. The saturated events, like figure 2.21 lower left, are believed to be the result of incoherent interactions and event pile-up. In addition to events in which the whole target is saturated there are approximately 30% of all events where the silicon only is saturated, see for example figure 2.21 upper right (which also exhibits no stable zero level). This is attributed to event pile-up (the dead time for the silicon is about twice that of the germanium), which is possibly compounded by radiation damage, and events where charged particles miss the germanium but still impinge on the larger area silicon planes.

the active target

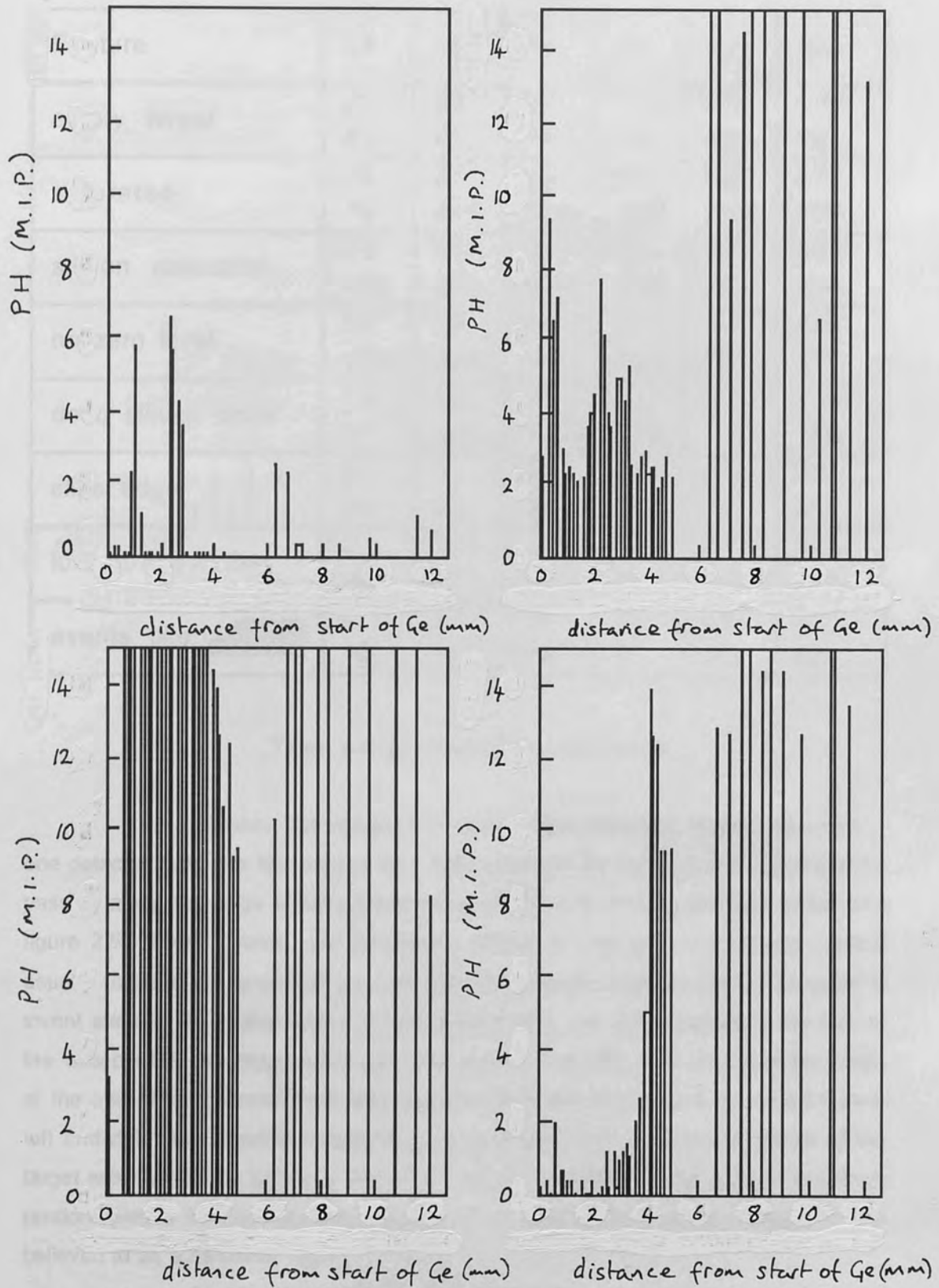


Figure 2.21: sample bad events rejected by the scanning program.

the active target

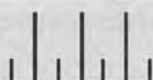

Feature	5A	1B	2A	2B	2C	ALL
empty target	21 8%	20 7%	20 7%	17 6%	23 8%	100 7%
saturated	20 7%	65 24%	62 23%	68 25%	62 23%	277 20%
silicon saturated	28 10%	91 33%	88 32%	98 36%	88 32%	393 29%
no zero level	35 13%	79 29%	60 22%	81 29%	77 28%	332 24%
dead silicon block	24 9%	23 12%	31 11%	25 10%	35 13%	148 11%
clips edge 	8 3%	5 2%	9 3%	7 3%	10 4%	39 3%
loss at end of Ge	6 2%	134 49%	166 60%	126 46%	127 46%	559 41%
events like 	2 1%	27 10%	17 6%	12 4%	19 7%	77 6%

Table 2.7: summary of rejected events

Events like figure 2.21 lower right illustrate 'spiked structure' - one detector high, one low, and so on - believed to be the result of a charged particle passing along the edge of the germanium monolith and missing alternate strips (see figure 2.5). These events are particularly difficult for the scanning program: whilst usually rejected on saturation grounds it is nevertheless possible for the program to invent steps in the region where the ph is increasing and these constitute the bulk of the 'accepted by the program but were bad' events. The feature of a lower pulse height at the end of the germanium is also in evidence in the visual scan, figure 2.21 lower left and right (the effect is exaggerated in saturated events). A further failure of the target was that blocks of two to five silicon planes were found to be zero at seemingly random places in otherwise good events (at a level of 10% of all events). This is believed to be a hardware fault.

All scanning software efficiencies from the visual scan are in broad agreement with the results from the simulation program (Table 2.5), and the

proportion of types of events found in the visual scan matches the results for the total data found by the scanning program in table 2.4. From this it is concluded that: the scanning software is capable of finding events with high efficiency; and that the simulation program provides a realistic model of the target. The effect of the scanning efficiency on the final lifetime result is discussed in chapter 4.

2.7 Nuclear Recoil

It was anticipated, from experience with the NA1 1980 silicon target, that the production point would reveal itself as a 'spike' in ionization produced by the recoiling nucleus after the coherent photon-nucleus interaction. However, an approximate calculation shows that this will not be the case for germanium.

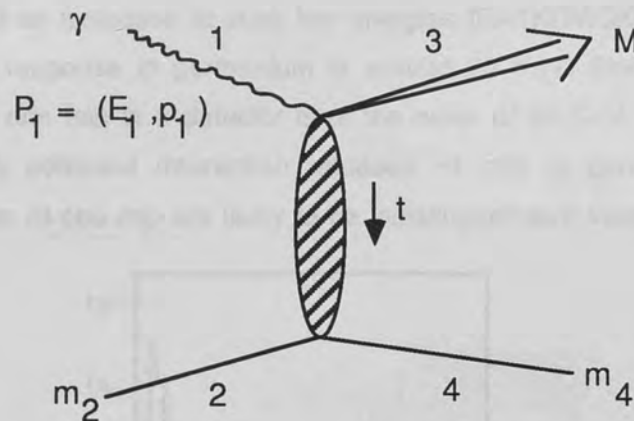


Figure 2.22: variables for recoil calculation

Appealing to figure 2.22, the four momentum transfer squared t is given by

$$t = (P_2 - P_4)^2 = (E_2 - E_4)^2 - (p_2 - p_4)^2$$

Using $p_2=0$, $E_2=m_2$ and $m_2=m_4$ in the lab frame, and the tools $E^2=p^2+m^2$ and $E=(T+m)$ where T is the kinetic energy, this reduces to

the active target

$$|t| = 2m_2 T_4$$

which is simply the expression for the classical kinetic energy in the limit that $t \rightarrow p^2$. Suppose that particle 1 (= particle 2) is a nucleon, or, more precisely, a proton (neutrons do not concern us since they will not obscure the target readout if knocked out in an incoherent interaction), with mass $\approx 1 \text{ GeV}/c^2$. If we approximate that the proton just getting across the Coulomb barrier has a kinetic energy $\sim 10 \text{ MeV}$, then we arrive at an estimate of $|t| \approx 2 \times 10^4 \text{ MeV}^2$.

In calculating the nucleus kinetic energy it is valid to assume that $t = p^2$ since $t \ll 2M_N$, where M_N is the mass of the nucleus, so that the kinetic energy of the nucleus is given by the classical relation $T_N = t/2M_N$. For germanium, $2M_N \approx 140 \text{ GeV}/c^2$, so $T_N = 140 \text{ KeV}$. Using the approximation that half the nucleus energy will manifest as ionization at such low energies [RATKOWSKI 75, LINDHARD 63], the ionization response in germanium is around 70 KeV. Since the ionization energy dumped by one mip in a detector is of the order of 60 KeV, we see that the nuclear recoil in a coherent interaction releases ~ 1 mip in germanium. Energy deposits of the order of one mip are likely to be indistinguishable from the noise.

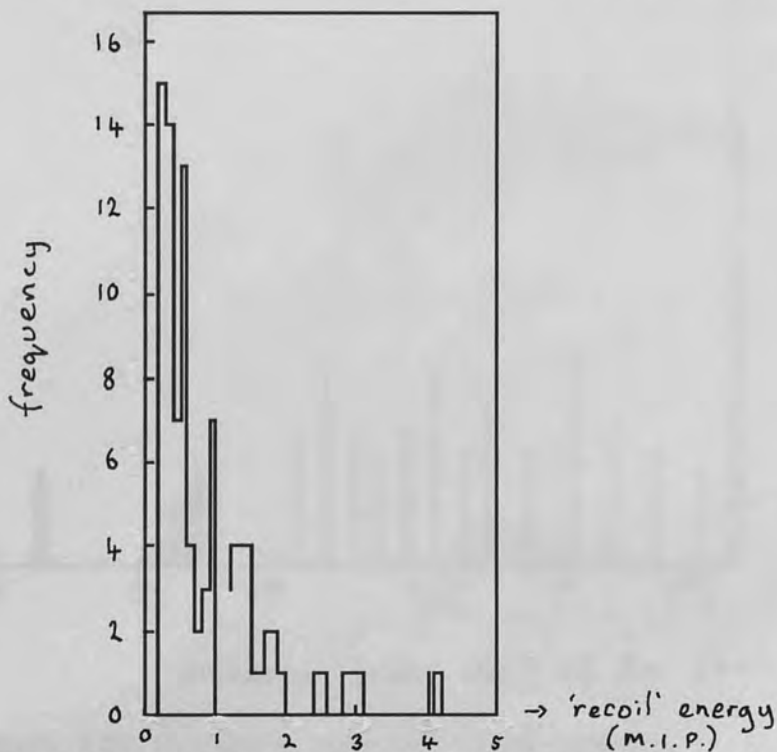


Figure 2.23: distribution of 'recoil' candidate energies in m.i.p.s

the active target

Nevertheless, a visual scan of 275 events in each period has been made searching for recoils. The events were scanned for activity in the zero level, subdivided into thin 'recoils' (one strip) and thick 'recoils' (two to six strips). These results are shown in table 2.8, along with the number of events with more than one 'recoil' candidate in the zero level. Shown in figure 2.23 is the distribution of energy per recoil (in mips) for the thick 'recoils'. Shown in figure 2.24 is an example target event with a candidate 'recoil' in the zero level.

Feature	5A	1B	2A	2B	2C	ALL
thin recoils	22 8%	22 8%	23 8%	19 7%	24 9%	110 8%
thick recoils	35 13%	18 7%	10 4%	9 3%	25 9%	97 7%
> 1 recoil candidate	9 3%	5 2%	4 2%	3 1%	8 3%	29 2%

Table 2.8: results of the recoil visual scan.

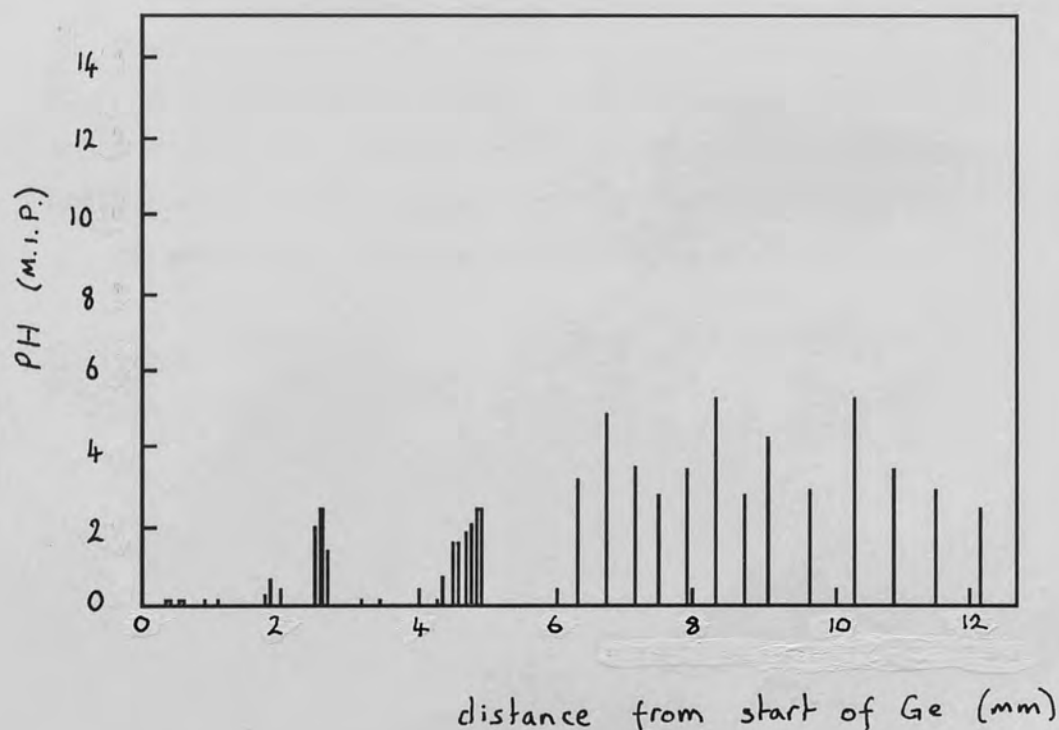


Figure 2.24: example of event with 'recoil' candidate.

The scanning program is capable of identifying recoil candidates in the zero level. However, since such excursions in the zero level cannot be positively associated with the interaction point they are not used as a selection criterion or in the lifetime measurement (instead, advantage is taken of the high proportion of charmed particles produced in association with charged pions in order to locate the interaction point of neutral particles, eg D^0 s). In particular the presence of more than one recoil candidate in some events, and the observation of similar positive excursions in the zero level of target patterns from identified ρ production events, indicate that these are unlikely to be ionization due to the nucleus recoiling. A more credible hypothesis is that they are e^+e^- produced from soft bremsstrahlung photons.

3.1 Initial State

The NA1 initial state, a photon in the energy range 70-225 GeV, was prepared in the photon radiating system up beam of the active target (figure 3.2). The H₄ beam line delivered around 2×10^{10} electrons per burst (at an electron energy of 178 GeV) with a momentum spread of $\Delta p/p = 1.4\%$. The electron was produced via the interaction of 460 GeV protons from the CERN SPS on 40 cm of beryllium in the process $p^+ \rightarrow \mu^+ + e^+ + X$ with the subsequent conversion of the photons from μ^+ decay to e^+e^- in a lead converter, see figure 3.1.

3: The FRAMM Spectrometer

3.0 Introduction

This chapter briefly summarises the NA1 apparatus other than the active target, which was described in detail in the preceding chapter. For a more detailed description the reader is referred to [SACKS 87]. The essential components are the beam, the active target, the vertex region (directly down beam of the target), the FRAMM spectrometer, and the trigger/data acquisition systems. The chapter concludes with a summary of the offline data production process, and the final event statistics.

3.1 Initial State

The NA1 initial state, a photon in the energy range 70-225 GeV, was prepared in the photon radiator/tagging system up beam of the active target (figure 3.2). The H4 beam line delivered around 2×10^6 electrons per burst (at an electron energy of 175 GeV) with a momentum spread of $\Delta p/p \sim 1.4\%$. The electrons were produced via the interaction of 450 GeV protons from the CERN SPS on 40 cm of beryllium in the process $p^+ + \text{Be} \rightarrow \pi^0 + X$ with the subsequent conversion of the photons from π^0 decay to e^+e^- in a lead convertor, see figure 3.1.

the FRAMM spectrometer

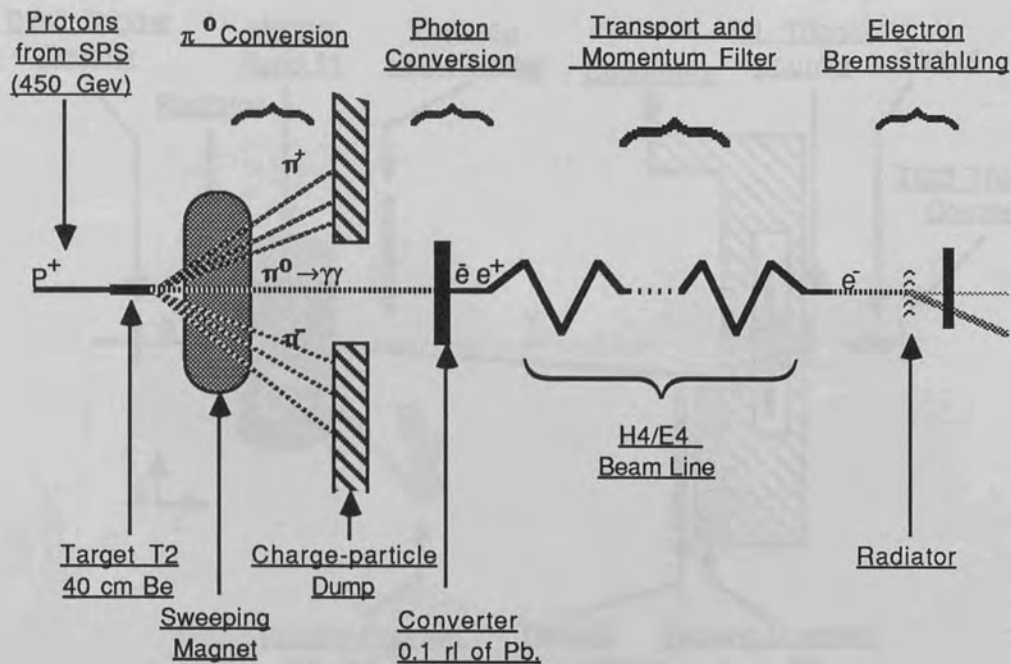


Figure 3.1: The H4 beam line - preparation of the NA1 initial state.

The electrons produced bremsstrahlung photons in a lead converter (10% of radiation length) and the photon energy was determined as the difference between the known beam energy and the scattered electron energy measured in the tagging system, consisting of a 4.4 Tesla metre magnet which kicks the scattered electron into the tagging drift chambers and lead glass hodoscope (figure 3.2). The energy resolution of the tagging system is 5%, and approximately 6×10^5 photons per burst pass through the collimator to the target.

3.2.1: Vertex Region

The vertex region is the region where the beam enters the target and the interaction takes place. It consists of a drift chamber and a lead glass hodoscope. The drift chamber is used to measure the position of the interaction vertex, and the lead glass hodoscope is used to measure the energy of the scattered electron.

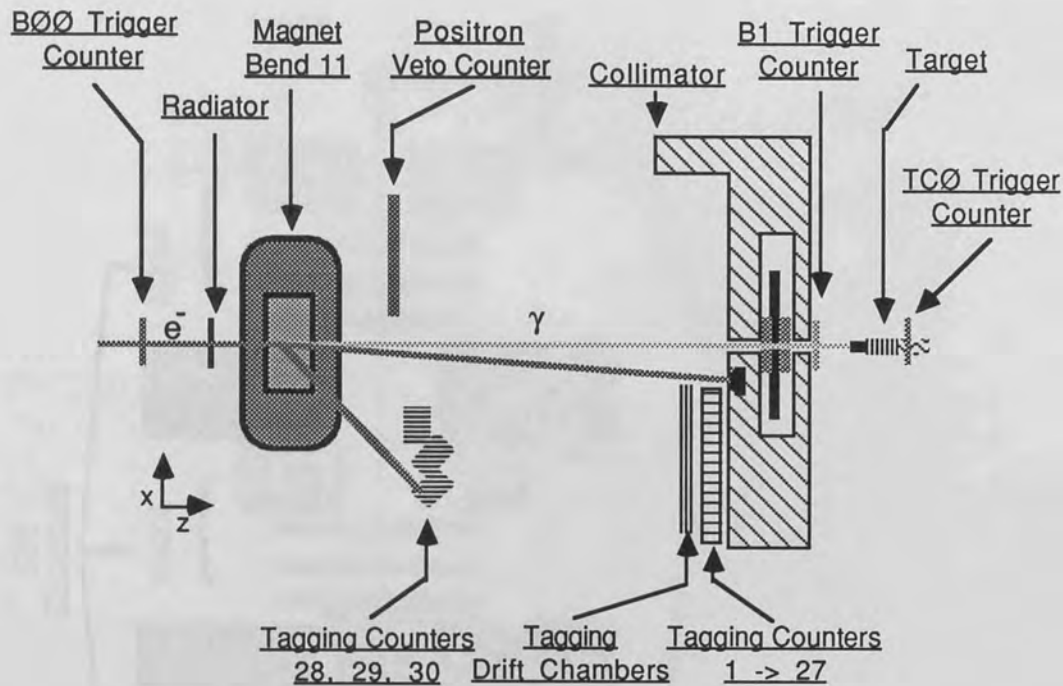


Figure 3.2: NA1 Photon tagging arrangement.

3.2: Final State

The final state is produced in the interaction of a photon in the NA1 active target, which also contributes to the measurement process, and which has been described in detail in chapter 2. The final state is analysed in the FRAMM Spectrometer and additional instrumentation positioned between the target and FRAMM to provide the connexion between these components of the measurement. Figure 3.3 gives a schematic overview of the FRAMM spectrometer.

3.2.1: Vertex Region

The equipment located directly down beam of the target consists of a high resolution circular drift chamber sandwiched between two stacks of multiwire proportional chambers (figure 3.4).

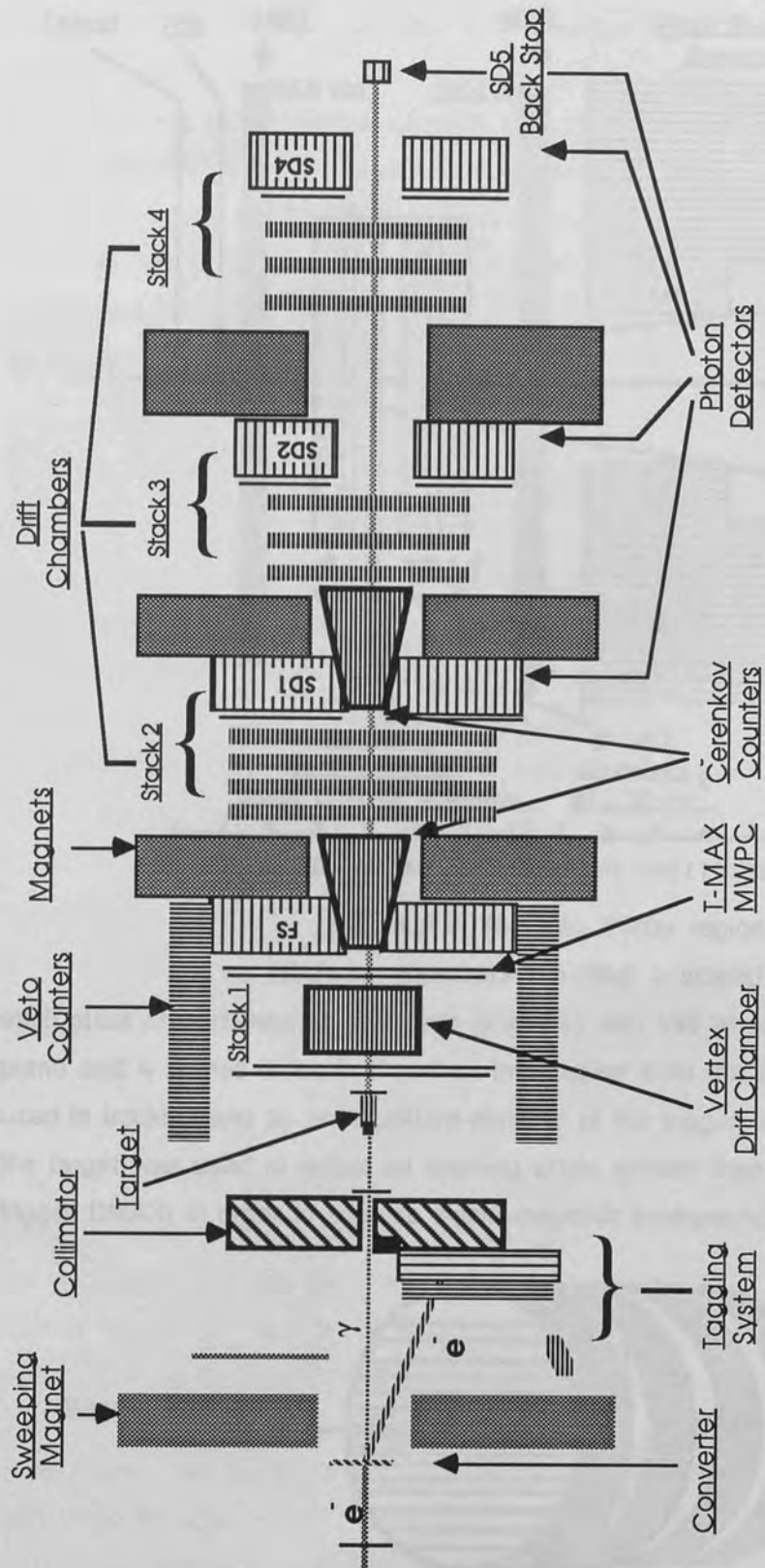


Figure 3.3: schematic representation of the FRAMM spectrometer (not to scale)

the FRAMM spectrometer

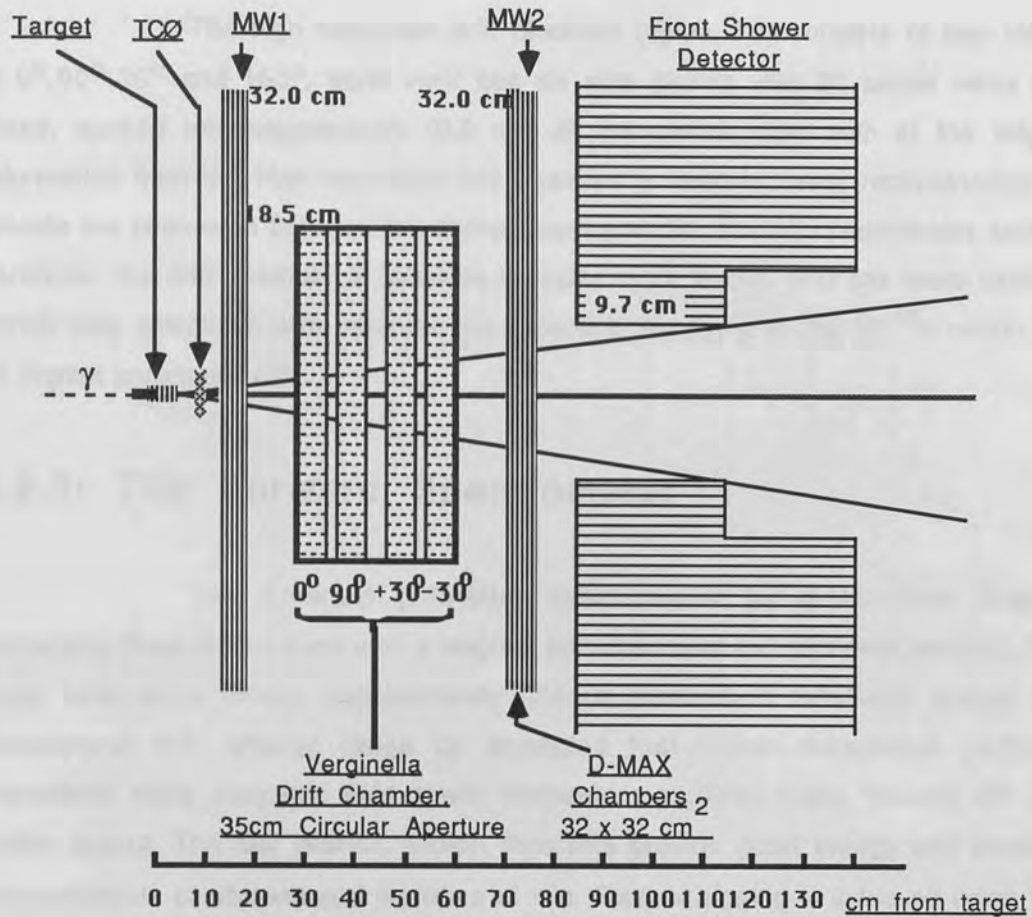


Figure 3.4: The NA1 Vertex region.

The multiwire chambers provided a spatial resolution of 0.5 mm, each stack comprising two chambers (x and y) with 100 wires (spaced at 2 mm) per plane and 4 planes in each chamber. Information from the multiwire chambers was used in tracking and as an important element of the trigger: the MWPC furthest from the target was used to select an opening angle greater than a given threshold (see trigger DMAX) in order to suppress electromagnetic background.

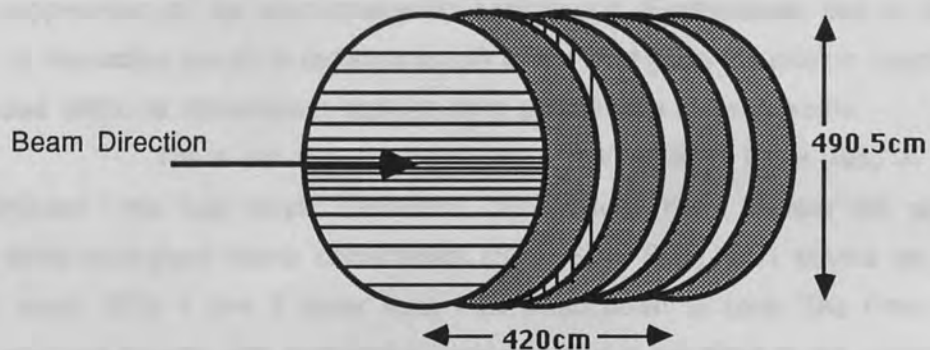


Figure 3.5: The high resolution vertex drift chamber.

The high resolution drift chamber (figure 3.5) consists of four views at 0° , 90° , 30° and 150° , each view has six wire planes with 20 sense wires per plane, spaced inhomogeneously (0.5 mm at the centre, 25.0 mm at the edge). Information from the high resolution drift chamber is used in event reconstruction to provide the connexion between the active target and the forward spectrometer and, in particular, the drift chamber is sensitive to wider angle tracks, and has been used to enrich data selections with particles (eg hyperons) decaying in the 10^{-10} s region via an impact parameter cut.

3.2.2: The Forward Spectrometer

The Forward (FRAMM) spectrometer is of modular design, comprising three stacks each with a magnet, drift chambers and a photon detector. The three lever arms ensure approximately uniform momentum resolution across the (secondary) NA1 energy range by arranging that higher momentum particles experience more magnetic field, lower momentum particles being "peeled off" into earlier stacks. The fine grained photon detectors provide good energy and positron measurements of photons and therefore of π^0 s. Flavour tagging is achieved using two threshold gas Cerenkov counters.

3.2.3: The Photon Detectors

The electromagnetic calorimeters play an important role in NA1: not only do they provide information on π^0 s, common decay products of charmed particles, they also contribute to the trigger selection of hadronic events and hence to the suppression of the electromagnetic background. Furthermore, due to the large ratio of interaction length to radiation length of the lead glass the photon detectors may be used offline to discriminate hadrons from photons via shower profile.

There are five electromagnetic calorimeters in all used in the NA1 experiment - two lead-acrylic sandwich calorimeters (Front Shower FS, and SD1), and three lead-glass matrix calorimeters (SD2, SD4, SD5). SD1 covers an angle of ± 90 mrad, SD's 4 and 5 cover from $+20$ mrad down to zero. The Front Shower detector was fraught with operational problems and is not used in the reconstruction of events, contributing only as a wide acceptance veto (to $\pm 30^\circ$) against incoherent

events in the trigger.

detector	structure	material	number of elements		length cm/RL		element area cm ²		hole size cm ²	start position cm
			front	back	front	back	front	back		
SD1	X,Y,W,X,Y hodoscope	Pb-scintillator	-	38x5 per view	-	-	-	-	19.2 x 19.2	528.9
SD2	matrix	Pb-glass	12	140	10/4	40/16	7 x 24.5	3.5 x 3.5	14 x 14	942.6
SD4	matrix	Pb-glass	10	108	10/4	50/20	7 x 24.5	3.5 x 3.5	7 x 7	1521.3
SD5	matrix	Pb-glass	1	4	10/4	50/20	7 x 7	3.5 x 3.5	-	1677.0

Table 3.1: Characteristics of the photon detectors.

3.2.3.1: Photon Detector SD1

Lead-scintillator photon detector SD1 was located 5.289 m from the target, had a total area $1.22 \times 1.22 \text{ m}^2$, save for a $19.6 \times 19.6 \text{ cm}^2$ hole in its centre, and was 17.7 radiation lengths in thickness. The detector was of "finger" construction, each scintillator finger being 10 mm x 32 mm (see figure 3.6).

The detector provides X, Y, W (45°), X, Y views, with each view consisting of a plane 5 fingers deep.

In addition, in order to aid position resolution ($\sim 2 \text{ mm}$) of showers, a pad chamber (a plane of streamer chambers read out by pads) was located before the W plane. SD1 had an energy resolution of

$$(40 / \sqrt{E}) \%$$

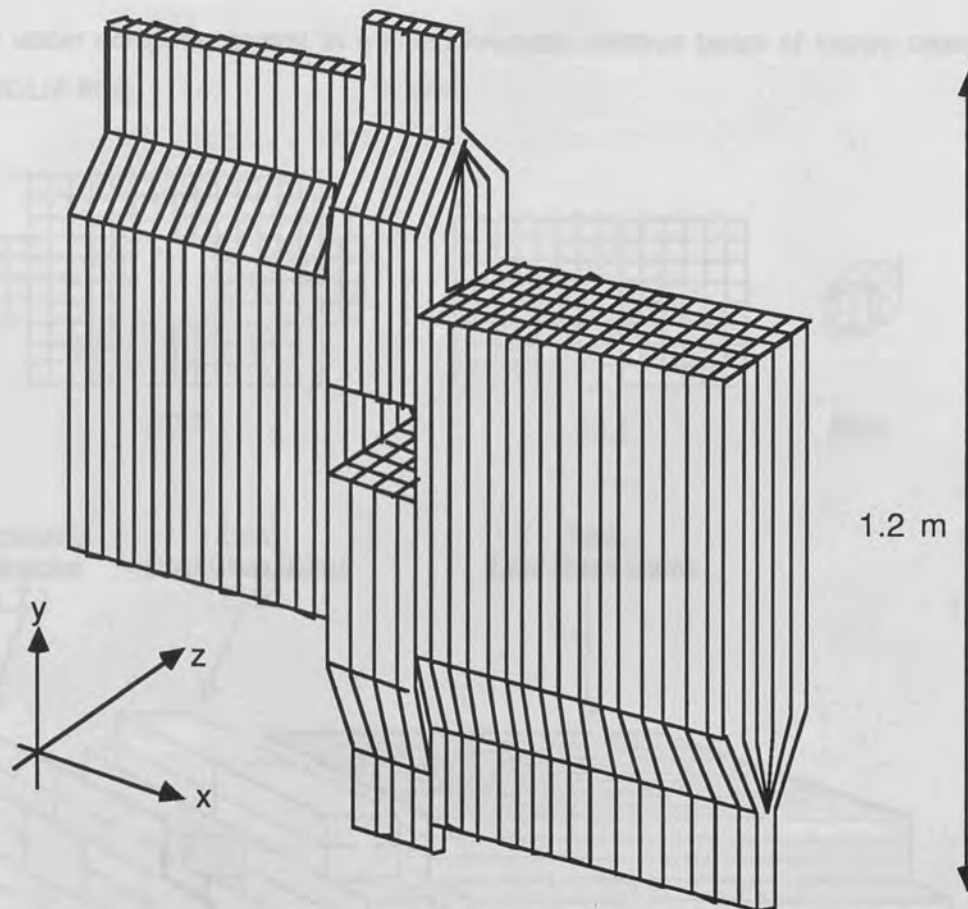


Figure 3.6: One plane of SD1 (front x coordinate).

3.2.3.2: Photon Detectors SD2, SD4 and SD5

Photon detectors SD2, 4 and 5 were of lead glass matrix construction. Details of the detectors can be found in [AMENDOLIA 80a]. A summary of the lead glass calorimeters is shown in table 3.1 and figure 3.7. Each detector comprises two parts, a "back" section of $3.5 \times 3.5 \text{ cm}^2$ SF5 lead glass blocks (SF5 glass has a radiation length of 2.45 cm and an interaction length 32.3 cm), and fronted by larger "front" lead glass blocks covering rows of ~ 14 back elements (figure 3.7), an arrangement allowing shower profile discrimination of electrons and hadrons. In addition, SD2 and SD4 were fronted by thin scintillator hodoscopes allowing photon/charged particle discrimination. Calibration of the photon detectors was accomplished by moving the

detector under computer control in a monochromatic electron beam of known energy [AMENDOLIA 80a].

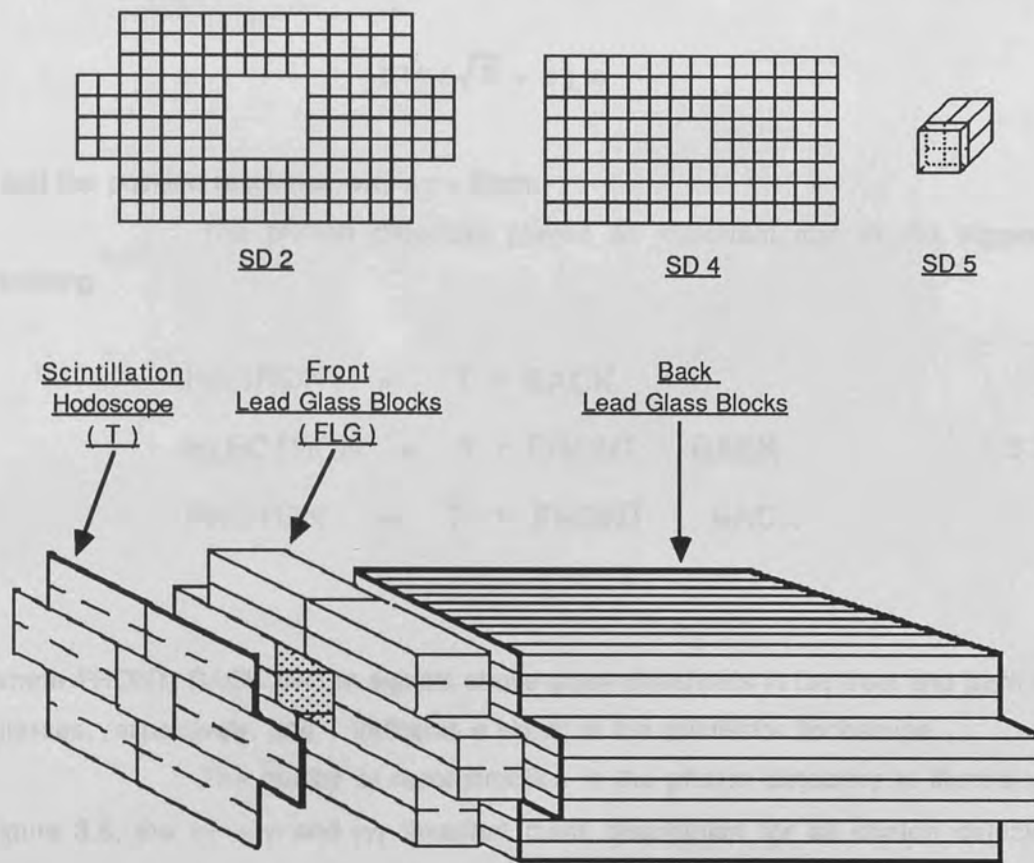


Figure 3.7: Lead glass electromagnetic calorimeters.

Reconstruction of the total shower energy has been discussed in detail in [SACKS 87]. Essentially, the total detector pulse height is given by

$$Ph_{SD} = \alpha Ph_{BACK} + \beta Ph_{FRONT} \quad (3.1)$$

where the parameters α and β , determined from calibration, compensate for the different response of the front and back lead glasses. The total energy is then related to the total pulse height in the photon detector via

$$E_{SD} = A Ph_{SD} + B \quad (3.2)$$

A, B being determined by a linear fit to calibration data.

The energy resolution of the lead glass shower detectors was

$$(14 / \sqrt{E} + 1) \%$$

and the position resolution was $\Delta x = 2\text{mm}$.

The photon detectors played an important role in the trigger by defining

$$\begin{aligned} \text{HADRON} &= T * \text{BACK} \\ \text{ELECTRON} &= T * \text{FRONT} * \text{BACK} \\ \text{PHOTON} &= \bar{T} * \text{FRONT} * \text{BACK} \end{aligned} \quad (3.3)$$

where FRONT, BACK denote signals above given thresholds in the front and back lead glasses, respectively, and T indicates a signal in the scintillator hodoscope.

The quality of reconstruction in the photon detectors is illustrated in figure 3.8, the $\pi^0 \rightarrow \gamma\gamma$ and $\gamma\gamma\gamma$ invariant mass distribution for all photon detectors, across all data periods. The FWHM is $70 \text{ MeV}/c^2$, as expected from the energy resolution.

3.2.4: Tracking

Charged particles are momentum analysed in FRAMM with a system of magnets and drift chambers. By arranging the magnets and drift chambers in the modular manner of FRAMM the momentum resolution remains uniform in the range 1 to 150 GeV/c, relevant to secondary decay products of BAs.

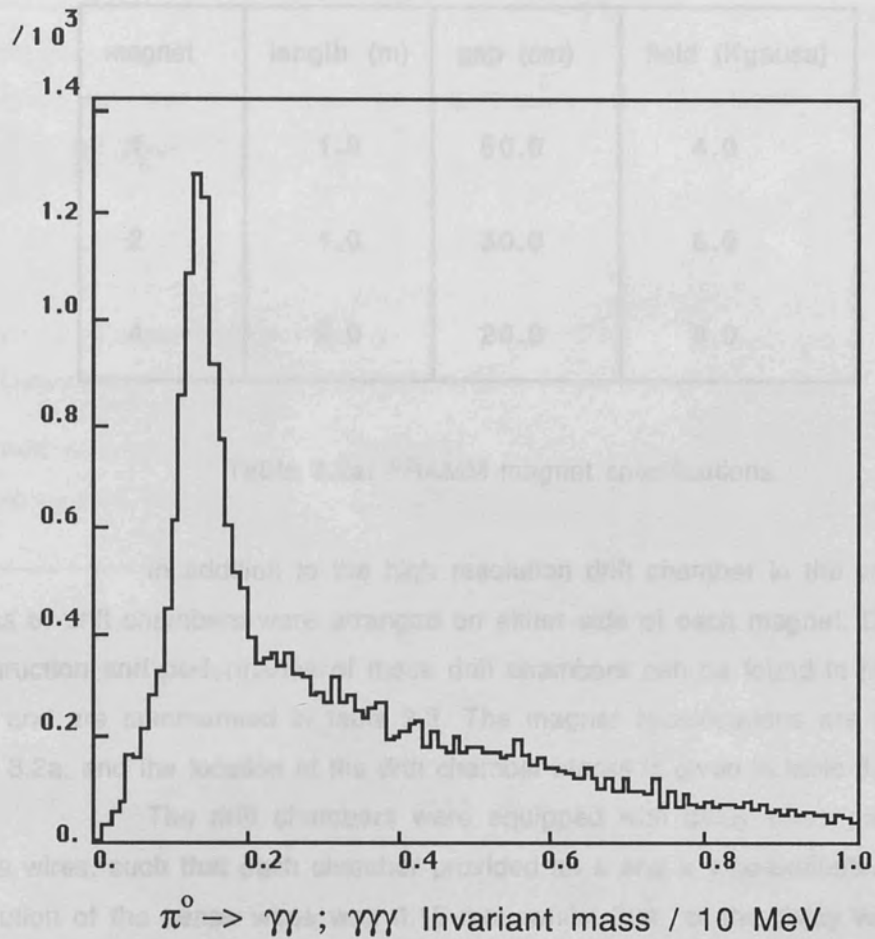


Figure 3.8: Neutral pion invariant mass distribution.

3.2.4: Tracking

Charged particles are momentum analysed in FRAMM with a system of magnets and drift chambers. By arranging the magnets and drift chambers in the modular manner of FRAMM the momentum resolution remains uniform in the range 1 to 150 GeV/c, relevant to secondary decay products in NA1.

the FRAMM spectrometer

magnet	length (m)	gap (cm)	field (Kgauss)
1	1.0	50.0	4.0
2	1.0	30.0	6.0
4	2.0	20.0	9.0

Table 3.2a: FRAMM magnet specifications.

In addition to the high resolution drift chamber in the vertex region, stacks of drift chambers were arranged on either side of each magnet. Details of the construction and performance of these drift chambers can be found in [AMENDOLIA 80b] and are summarised in table 3.3. The magnet specifications are contained in table 3.2a, and the location of the drift chamber stacks is given in table 3.2b.

The drift chambers were equipped with delay wires parallel to the sense wires, such that each chamber provided an x and a y co-ordinate. The spatial resolution of the sense wires was 0.15 mm, whilst that of the delay wires was 4.5 mm. Use of the delay wires in a combination of x and y orientated chambers further resolved ambiguities in the information furnished by the sense wires.

STACK	Start position from target (m)	Length (m)
2	3.2	1.76
3	7.68	0.84
4	12.858	2.058

Table 3.2b: location of the drift chamber stacks

the FRAMM spectrometer

dimensions	50 x 70 cm ²		
sensitive area	38.4 x 57.6 cm ²		
drift cell size	48 mm		
gap	11 mm		
+HV sense wires	1680-1730 V		
-HV field wires	3500-4000 V		
sense wires/chamber	16		
sense wire - delay wire separation	1 mm		
field wire spacing	2 mm		
delay wire propagation velocity	6 cm/ns		
stack	number of chambers	start position (cm)	length (cm)
2	10	320.0	176.0
3	8	768.0	84.0
4	6	1285.8	205.8

Table 3.3: Drift Chamber parameters.

Reconstruction of tracks involved the fitting of rettas to the space point information of each stack, under the constraint that the rettas project back to the target in the y-plane (no magnetic field). Rettas matched on either side of a magnet provide an angle θ , from which the momentum is determined via

$$p = \frac{0.299 e B l}{\theta} \quad (3.4)$$

where e is the electron charge, B is the magnetic field, and l is the magnet length. The ideal momentum resolution of the FRAMM spectrometer was $\Delta p/p \sim 2\%$ in the 1-150 GeV/c regime. However, in practice the average $\Delta p/p$ is estimated to be of the order of 4%, due to measurement inefficiency, which bears

comparison with the observed effective mass resolution (see chapter 4).

3.2.5: Cerenkov Counters

Flavour tagging is a crucial tool for enriching the charm signal relative to background - specifically, the identification of strangeness in the final state dramatically reduces the combinatorial mass permutations which must be considered. This is implemented in NA1 by the use of two multicell threshold Cerenkov counters [AMENDOLIA 80c], located in the gaps of the first two magnets for reasons of space economy. The design of the Cerenkov counters was made with the compromise of small cell size in order to cope with high multiplicity events against sufficient cell size to contain the Cerenkov light cone without multiple reflections. Additionally, with a view to minimizing the material seen by the secondaries and beam, the detectors are operated at atmospheric pressure, allowing the window to be made as thin as possible. Detail of the Cerenkov counters construction and operational parameters is displayed in figures 3.9a and 3.9b, and table 3.4.

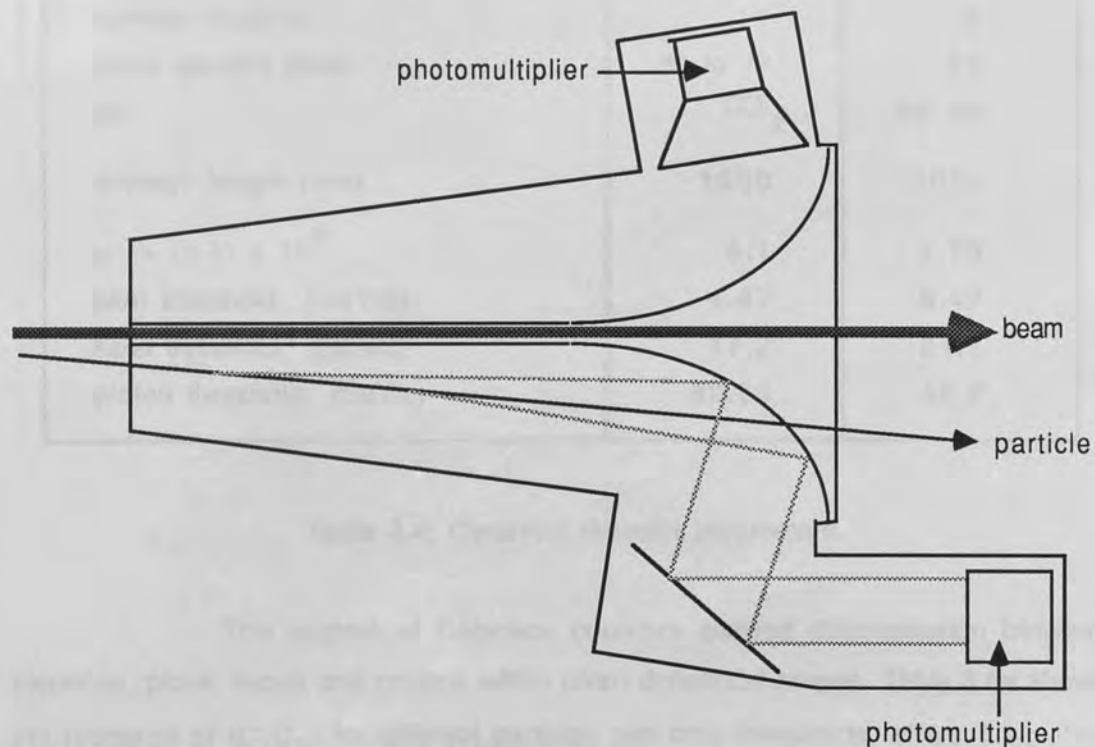


Figure 3.9a: schematic diagram of the Cerenkov counters.

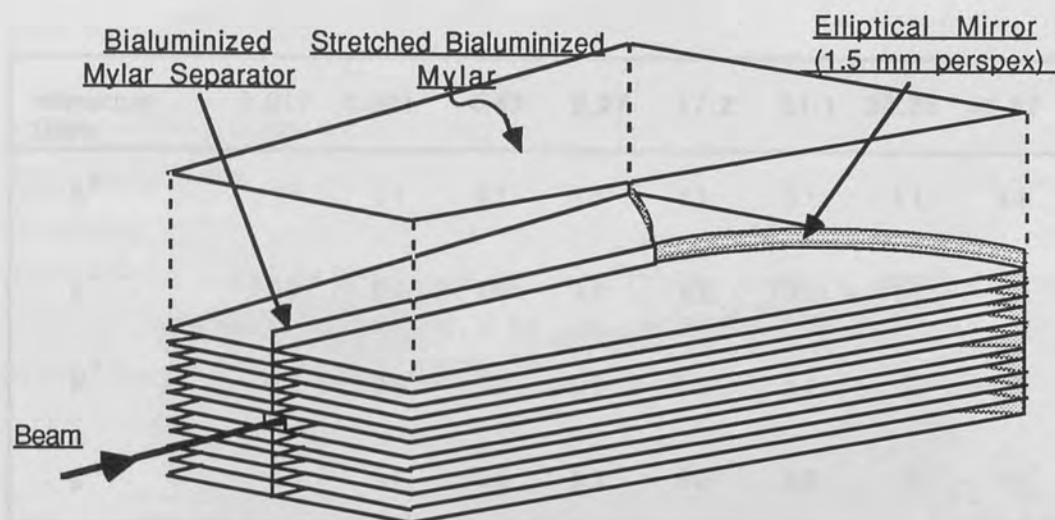


Figure 3.9b: Cerenkov counter construction.

	C ₁	C ₂
number of cells	22	10
number of planes	11	5
plane spacing (mm)	30 to 77	53
gas	CO ₂	dry air
average length (mm)	1500	2000
$\mu = (n-1) \times 10^4$	4.1	2.73
pion threshold (GeV/c)	4.87	5.97
kaon threshold (GeV/c)	17.2	21.1
proton threshold (GeV/c)	32.86	40.2

Table 3.4: Cerenkov detector parameters.

This system of Cerenkov counters allowed discrimination between electrons, pions, kaons and protons within given dynamical ranges. Table 3.5a shows the response of (C₁C₂) for different particles and their thresholds, where 1 signifies Cerenkov light seen and 0 denotes no Cerenkov light seen. Table 3.5b summarizes the dynamical ranges over which particles may be unambiguously identified.

the FRAMM spectrometer

momentum GeV/c	0.017	0.021	4.87	5.97	17.2	21.1	32.86	40.82
$e^{+ -}$	10	11	11	11	11	11	11	11
$\pi^{+ -}$	00	00	10	11	11	11	11	11
$K^{+ -}$	00	00	00	00	10	11	11	11
$p^{+ -}$	00	00	00	00	00	00	10	11

Table 3.5a: Response of Cerenkov counters to particles against momentum.

momentum GeV/c code	0.017	0.021	4.87	5.97	17.2	21.1	32.86	40.82
2	e →							
1	π →							
0	$pK\pi$ →	$pK\pi$ →			$K\pi$ →	$pK\pi$ →		
-1			Kp →	K →				
-2						p →		

Table 3.5b: Ranges in which Cerenkov counters discriminate $pK\pi$.

The Cerenkov detectors were observed to operate at high efficiency in test beam conditions (both over 99%). In practice, the efficiency was lower, principally due to the multibody nature of charm events, such that more than one particle was present in one cell or one particle crossed more than one cell. Also efficiency was reduced due to a particle being near the edge of the Cerenkov, and the

effect of the cell walls.

An estimate of the operating efficiency of the Cerenkov system for pions has been obtained via examining ω events. These events, obtained from the peak shown in figure 3.10, should contain only pions. Of charged tracks inside the region of acceptance for pions 86% were identified as pions and 14% as kaons. These efficiencies are expected to be lower for charm events, where the charge multiplicity is higher. Nevertheless, an estimate of the order of 85% efficiency has been made for kaons [SACKS 87], by examining the Cerenkov response in well reconstructed D events.

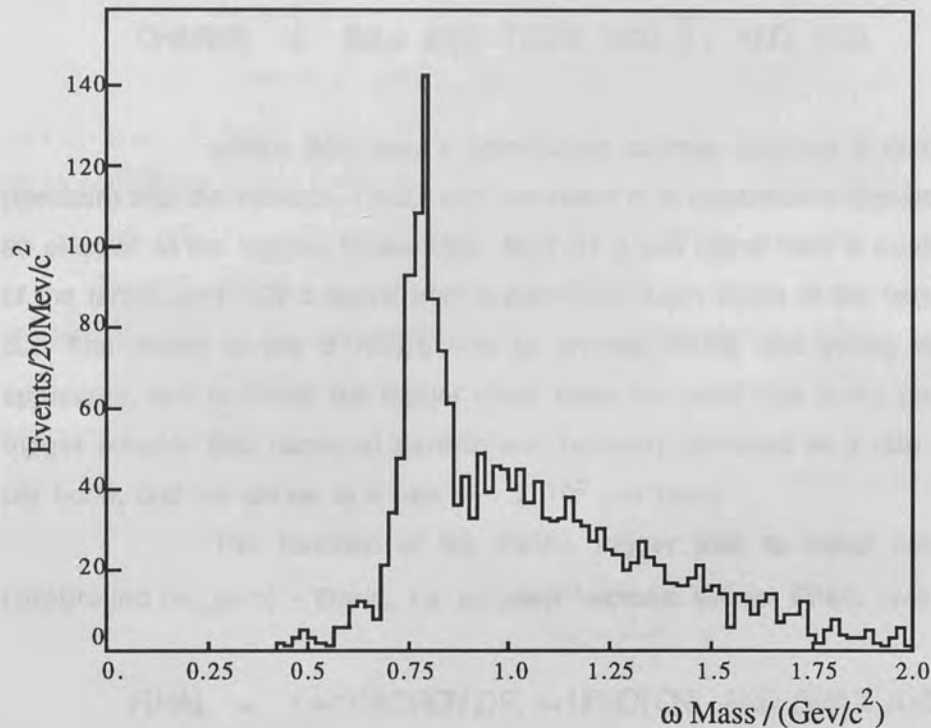


Figure 3.10: $\pi\pi\pi^0$ effective mass distribution.

3.2.6: The Trigger

Due to the small charm production cross section ($\sigma(\gamma p \rightarrow \text{charm}) \sim 1\mu\text{b}$) it is desirable to operate the apparatus at high rates, and it is the role of the trigger to efficiently reduce the background, in order that the data read out rate be reduced to proportions manageable by the data acquisition system. In NA1 the data acquisition was performed by CAMAC standard electronics under the control of two

the FRAMM spectrometer

PDP 11/34a's. The trigger was built of two components, known as STROBE, which signaled the production of an interesting system in the target; and FINAL, which voted as to whether or not the event in the forward spectrometer was worth recording. The trigger electronics were implemented using CAMAC standard programmable logic units, affectionately known as magic boxes. A given trigger configuration could be developed in a high level language and the output down loaded to the magic boxes, providing considerable flexibility without the necessity for hardware changes.

The STROBE's primary setting was to define "*neutral beam into target, charged particles out*". In practice this was defined by

$$\text{CHARGE} = \text{B00} \cdot \text{AND} \cdot \text{TAGG} \cdot \text{AND} \cdot \overline{\text{B1}} \cdot \text{AND} \cdot \text{TC0} \quad (3.5)$$

where B00 was a scintillation counter defining a charged particle (electron) into the radiator, TAGG was the result of a combination signals of indicating an electron in the tagging hodoscope, $\cdot \text{NOT} \cdot \text{B1}$ a null signal from a scintillator in front of the target, and TC0 a signal from a scintillator down beam of the target, see figure 3.2. The action of the STROBE was to provide timing and gating signals to the apparatus, and to inhibit the trigger chain while an event was being processed. The trigger counter B00 (charged particle into radiator) operated at a rate of $1.3 \cdot 10^6$ per burst, and the strobe at a rate of $1.5 \cdot 10^5$ per burst.

The function of the FINAL trigger was to reject electromagnetic background ($\sigma_{\text{tot}}(\text{em}) \sim 20\text{mb}$), i.e. to select hadronic events. FINAL was defined by

$$\text{FINAL} = (\geq 1\text{HADRON} \cdot \text{OR} \cdot \geq 1\text{PHOTON}) \cdot \text{AND} \cdot \text{DMAX} \cdot \text{AND} \cdot \text{TC0} \cdot \text{AND} \cdot \overline{\text{FA}} \cdot \text{AND} \cdot \overline{\text{SD5}} \quad (3.6)$$

$\geq 1\text{HADRON}$ ($\geq 1\text{PHOTON}$) denotes at least one hadron (photon) out of the horizontal plane (no magnetic field), where HADRON (PHOTON) is defined by the shower detectors as in equation 3.3. TC0 could discriminate charged particle multiplicities between 1 and 6 leaving the target, and in FINAL was required to register at least two. $\cdot \text{NOT} \cdot \text{FA}$ vetoed events with wide angle tracks (incoherent events) using the front shower detector. Flag $\cdot \text{NOT} \cdot \text{SD5}$ vetoed events where the beam killer (shower detector SD5) registered more than 5 GeV energy deposit, suppressing events with multiple bremsstrahlung. DMAX was a decision by the MWPC's following

the target (see figure 3.4) on the opening angle of the system leaving the target: e^+e^- pairs are produced with zero opening angle, in contrast to the more open hadronic events. The wire hit representing the maximum deviation from the zero axis was selected, and DMAX was set true if this deviation was greater or equal to 4mm, corresponding to an opening angle of 5.7 mrad.

The FINAL rate was approximately 900 per million STROBE's, or around 14 per burst, well within the capability of the data acquisition computer.

3.3 Offline Production

Some 5.2 million events passed the online trigger in useful data taking runs. A large proportion (~80%) of these events were electromagnetic background. In order to further reduce the number of events to manageable proportions the raw data was passed through an offline soft-trigger.

At this stage the calibration data was used to arrive at more reliable decisions on the nature of the event. Events were accepted if they had at least one hadron candidate or good photon candidate outside the horizontal plane (where most electromagnetic events will occur). Events were rejected where there was no energy deposited in the electromagnetic calorimeters outside the horizontal plane, or the only response outside the horizontal plane was either compatible with leakage from the horizontal plane or was contained in a single element in the lead glass matrix calorimeters (ie possibly due to a photon from electron bremsstrahlung). These cuts rejected approximately two thirds of the raw data passing the online trigger. Of the accepted events 60% were hadronic, as determined by visual examination of samples of the events passing the selection criteria. Of the rejected events 5% were hadronic, however these losses were of low multiplicity events and unlikely to have been charm.

The events satisfying the soft trigger were then passed through the production program. The production program used the calibration information to reconstruct the event properly. The drift chamber information was converted into space points, and within each stack these were fitted into a track, constrained to point back to the target in the y-plane (ie vertical plane). These tracks were then matched between stacks and a χ^2 calculated. The best fit was accepted and the momentum of the track calculated from equation 3.4. The hits in the electromagnetic calorimeters were clustered and the energy of the showers calculated from equations 3.1 and 3.2. The

the FRAMM spectrometer

target information was converted into minimum ionizing particle equivalents according to equation 2.9. The Cerenkov detector response (on or off) was determined using the calibration thresholds. The production program spent on average two seconds per event.

The output of the production program allowed more reliable hadron/electron discrimination via the shower profile, and therefore a better level of rejection against electromagnetic background. To select on the shower profile the ratio of the energy deposits in the front lead glass and the total energy deposit in the calorimeter (E_{front} and E_{total} respectively) are compared with the ratio of E_{total} and the particle energy (E_{particle}). When plotting $E_{\text{front}}/E_{\text{total}}$ against $E_{\text{total}}/E_{\text{particle}}$ electromagnetic showers are expected to be largely contained, so that $E_{\text{total}}/E_{\text{particle}}$ is close to 1, and the shower should start early, so that $E_{\text{front}}/E_{\text{total}}$ should be larger than for hadrons. Hadronic showers, on the other hand, are expected to punch through the back of the calorimeter and $E_{\text{total}}/E_{\text{particle}}$ should be less than 1, and the shower should start late in the calorimeter giving a small $E_{\text{front}}/E_{\text{total}}$. The $E_{\text{front}}/E_{\text{total}}$ vs $E_{\text{total}}/E_{\text{particle}}$ distribution for the FRAMM electromagnetic calorimeters is plotted in figure 3.11 below (note that events close to the origin in the pion plot have been removed to avoid saturation).

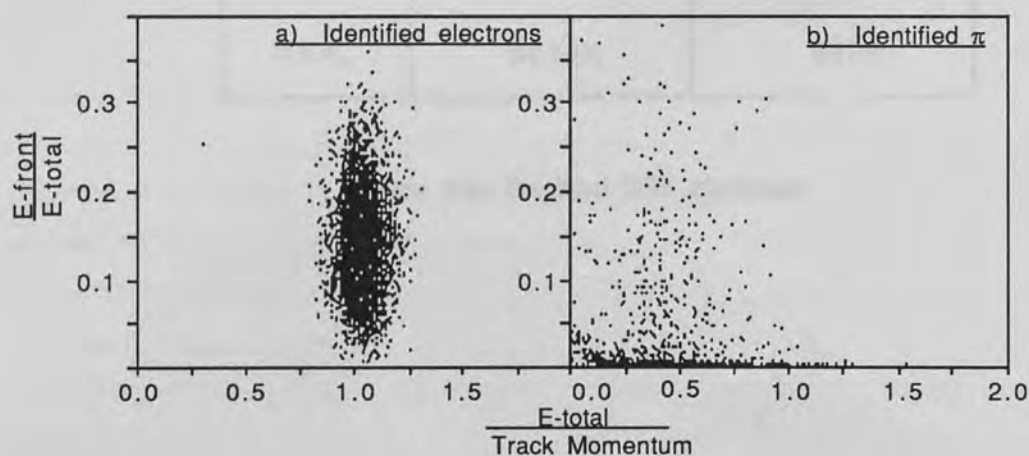


Figure 3.11: electron/pion discrimination using the electromagnetic calorimeters.

Events output from the production program were written to

the FRAMM spectrometer

micro-DST if they satisfied the following cuts:

- (i) there were at least 2 charged tracks;
- (ii) there was at least 30GeV of energy deposited in FRAMM;
- (iii) there were no more than 3 electron candidates in the horizontal plane;
- (iv) there was only one cluster in the tagging calorimetry.

The final DST statistics are shown in table 3.6.

PERIOD	RAW DATA	ON MICRO-DST
5A	600K	111K
1B	650K	90K
2A	1060K	136K
2B	1600K	196K
2C	1300K	96K
TOTAL	5210K	629K

Table 3.6: the final DST statistics.

4: Λ_c Analysis.

4.0 Introduction

The search for the Λ_c , the lowest mass charmed baryon state, was performed by analysing the effective mass distributions of the channels

$$\Lambda_c \rightarrow p^+ K^- \pi^+ + \text{c.c.}$$

$$\Lambda_c \rightarrow p^+ K^- \pi^+ \pi^0 + \text{c.c.}$$

The data satisfied the following general cuts:

- (i) $5 \leq \text{number of charged tracks} \leq 10$
- (ii) at least two changes in charged multiplicity detected in the target
- (iii) $-1 \leq \text{total charge of event} \leq 1$
- (iv) $90 \text{ GeV} \leq \text{photon tagging energy} \leq 225 \text{ GeV}$
- (v) $0 \text{ GeV} \leq \text{energy in forward spectrometer} \leq 225 \text{ GeV}$
- (vi) $0.5 \leq \text{ratio of tagging to spectrometer energy} \leq 1.1$
- (vii) no more than one electron in the event, as identified by the shower profile.

Just over 18000 events satisfy these conditions and a demand that the event must contain a proton identified by the Cerenkovs. These cuts are designed to ensure reasonably well-reconstructed hadronic events. In particular the ratio of spectrometer energy to tagging energy is asymmetric to allow for unreconstructed neutrals and reconstruction efficiency losses. It should be noted here that the target cut is loose, i.e. it requests two changes of charge multiplicity (at least) and a stable 0 level, but no cut is made on the level of noise in the target event. The target cut enriches the charm signal to noise. All Λ_c candidates are furthermore required to be within 0.5 degrees of the beam axis, in order to preferentially select coherent production.

In addition, the following particle identity criteria were applied

Λ_C Analysis

throughout the analysis unless otherwise stated:

- (a) π : a particle identified by the Cerenkovs as a pion, or a particle with an ambiguous flagging (generally one outside the Cerenkov dynamical range).
- (b) K : a Cerenkov flagged kaon or an ambiguous track with a momentum greater than 5 GeV.
- (c) p : a Cerenkov flagged proton.
Note that this restricts the momentum of the proton to the range 17-40 GeV.
- (e) e : tracks identified as electrons by their shower profile or in the Cerenkovs.

The $p^+K^-\pi^+$ + charge conjugate and $p^+K^-\pi^+\pi^0$ + cc effective mass distributions are shown in figure 4.0. The combinatorial background in both channels is overwhelming. In order to preferentially reduce the background two techniques were applied: (1) to require that the Λ_C be accompanied by a large impact parameter track, by hypothesis a signature for a Λ^0 in the event; and (2) to require that the secondaries from the Λ_C decay be consistent with decay via resonances, specifically the Δ and K^* resonances.

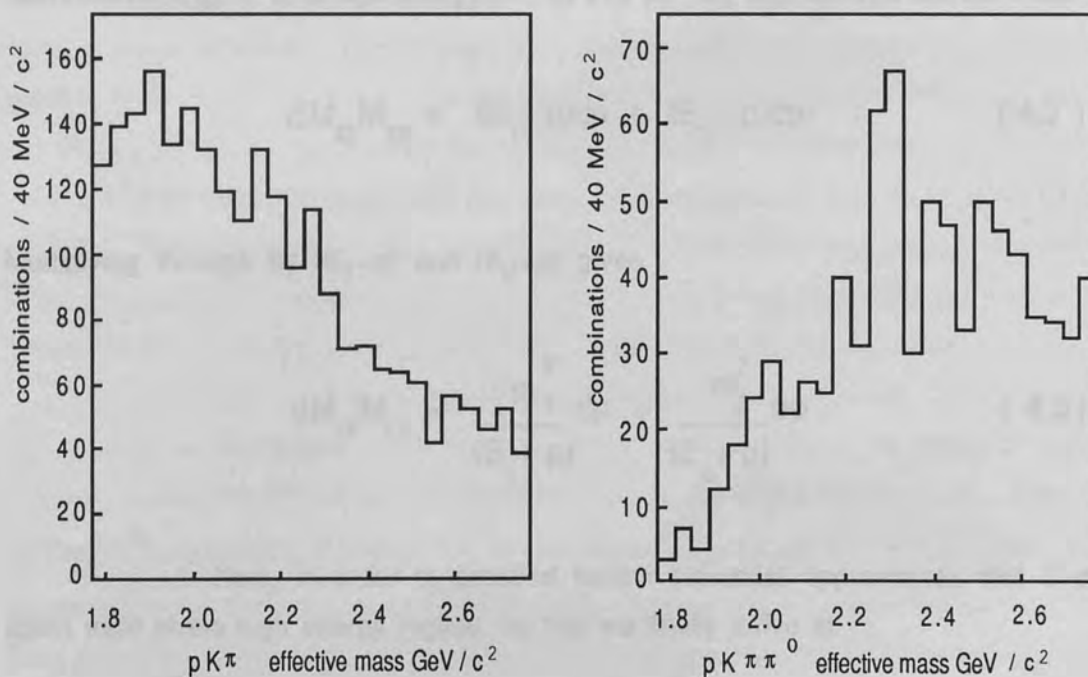


Figure 4.0: (previous page) the $p^+K^-\pi^+ + cc$ and $p^+K^-\pi^+\pi^0 + cc$ effective mass distributions after the general cuts. The most important cuts are the proton request and the target cut.

It is appropriate at this point to discuss the expected mass resolution. The fundamental equation $E^2 = p^2 + m^2$ expressed for the reconstruction of the effective mass of a parent particle decaying into n secondaries is

$$M_{12\dots n}^2 = \left(\sum_{i=1}^n E_i \right)^2 - \left(\sum_{i=1}^n p_i \right)^2 \quad (4.1)$$

In order to get a first order approximation on the expected mass resolution we need to differentiate equation 4.1 with respect to momentum, so that we get the mass resolution as a function of the momentum resolution, which we know. This becomes complicated in a rigorous treatment so we make the following assumptions: a) we consider a two body decay at 90° in the centre of mass so that both the particles have the same momentum in the lab; b) at high energy we may approximate $\theta_{lab}=0$; c) at high energy $\beta=1$ so that we may approximate $dE=dp$. Then

$$dM_{12} M_{12} = (E_1 - p)dp + (E_2 - p)dp \quad (4.2)$$

Multiplying through by (E_1+p) and (E_2+p) gives

$$dM_{12} M_{12} = \frac{m_1^2}{(E_1+p)} dp + \frac{m_2^2}{(E_2+p)} dp \quad (4.3)$$

Now, in order to proceed further we must approximate that $E=p$, again valid in the high energy regime, so that we finally arrive at

Λ_c Analysis

$$\Delta M_{12} = \frac{1}{2M_{12}} (m_1^2 + m_2^2) \frac{\Delta p}{p} \quad (4.4)$$

Thus for two body decay at 90° in the centre of mass, the dominant case for isotropic decay, we expect the effective mass resolution to be dominated by the momentum resolution of the heaviest particle. For decay at other centre of momentum angles the lab momenta are asymmetric and the effective mass resolution tends to be dominated by the momentum error of the secondary having the greatest momentum.

From equation 4.4 we may make our estimate. The modular design of FRAMM should ensure that $\Delta p/p$ is approximately constant. An estimate of $\Delta p/p$ may be made from

$$p \approx 0.299 q B l \frac{1}{\theta} \quad (4.5)$$

where q is electron charge, B is the magnetic field in Tesla, l the length of the magnet in metres, and θ the angle between two matched retta on either side of the magnet in radians, for p in GeV/c. Equation 4.5 implies that $\Delta\theta/\theta \approx \Delta p/p$. For chambers separated by one metre with a resolution of 0.2mm, $\Delta\theta$ is expected to be $\sim 0.2\text{mr}$. From equation 4.5, in a magnet of say 0.4 tesla (FRAMM first lever arm), a particle of 10GeV/c momentum will be deviated through $\sim 12\text{mr}$. This implies a $\Delta\theta/\theta \approx 1.6\% \approx \Delta p/p$. The treatment for higher energy particles is more complicated since they see more than one lever arm, but this should ensure that $\Delta p/p$ is approximately constant. Therefore we expect a $\Delta p/p \approx 2\%$ in the ideal case, and more realistically this figure might be set at something like 4% if allowances are made for less than perfect efficiency in the tracking chambers, imperfect calibration data etc.

Returning to the question in hand, the mass resolution, if we use our estimate of the momentum resolution $\Delta p/p \sim 4\%$ in equation 4.4 for the decay $\Lambda^0 \rightarrow p\pi$, then we obtain a mass resolution $16\text{MeV}/c^2$, or an expected FWHM of the order of $30\text{MeV}/c^2$. Extending equation 4.4 to the three body decay of the $\Lambda_c \rightarrow pK\pi$ (the approximation is becoming more tenuous here, since we are asking all the particles to have the same momentum), we can estimate by simply adding the mass squared of the third particle inside the bracket. Again we expect the effective mass resolution to be

Λ_C Analysis

dominated by the momentum resolution of the heaviest particle, ie the proton for the Λ_C , so it is essentially the same as for the two body case.

The mass resolution becomes more complicated still for the decay channel $\Lambda_C \rightarrow pK\pi\pi^0$, since the π^0 resolution depends on the electromagnetic calorimeters and will be different to that for the charged particles. The expected resolution on the π^0 mass is

$$\frac{\Delta_m^2}{m_{\pi^0}^2} \approx \frac{\Delta_E^2}{E_1^2} + \frac{\Delta_E^2}{E_2^2} + \frac{\Delta_\theta^2}{\theta^2} \quad (4.6)$$

where the energy resolution $\Delta E/E$ is $\sim 20\%/\sqrt{E}$ and the spatial resolution $\sim 2\text{mm}$ for the electromagnetic calorimeters (lead glass matrix). For a $20\text{ GeV}/c$ π^0 decaying into two photons at $\pi/4$ to the beam axis in the centre of mass, each $10\text{ GeV}/c$ photon will make an angle $\sim 7\text{mrad}$. Approximating the distance from the target to the first lead glass detector to be 8m , then the error in the angle is $\sim 0.25\text{mrad}$, and the resolution of the π^0 mass is therefore dominated by the energy resolution of the shower. Evaluating equation 4.6 then leads to a resolution in the π^0 mass of the order of $12\text{ MeV}/c^2$ for a $10\text{ GeV}/c$ π^0 in this scenario, or approximately $25\text{ MeV}/c^2$ for a $40\text{ GeV}/c$ π^0 . The situation is worse for showers which are not contained in a nonet of lead glass blocks, and particularly poor near the edges of the electromagnetic calorimeters. Therefore in reality we expect somewhat poorer mass resolution on the π^0 , of the order of $30\text{ MeV}/c^2$ on average, as judged from the π^0 signal in the $\gamma\gamma$ effective mass distribution. The net effect of the π^0 resolution on the $\Lambda_C \rightarrow pK\pi\pi^0$ decay channel is to degrade the mass resolution to a figure estimated to be of the order of $35\text{ MeV}/c^2$, and thus we expect a FWHM of the order of $70\text{ MeV}/c^2$ in this channel, which is in good agreement with the data.

4.1 Large Impact Parameter Tagging

The decay $\Lambda_C \rightarrow \Lambda^0 + X$ has a branching ratio of the order of 33% [PDG 86]. Whilst this channel is not expected to be useful in the lifetime

Λ_C Analysis

measurement (for example $\Lambda_C \rightarrow \Lambda^0 \pi$ is not detectable in the NA1 target), for a dominant pair production mechanism $\gamma N \rightarrow \Lambda_C^+ \Lambda_C^- N$, a " Λ^0 in event" tag should enrich the Λ_C sample.

That the production mechanism should be dominantly pair production follows from the coherent diffractive nature of the event. Since the initial and final state must have baryon number = 0, the most economic production mechanism is $\gamma N \rightarrow \Lambda_C^+ \Lambda_C^- N$. The next most economic mechanisms conserving both charm and baryon quantum numbers are $\gamma N \rightarrow \Lambda_C^+ D^0 p^- N$ and $\gamma N \rightarrow \Lambda_C^- D^+ n N$, both carrying considerable energy overheads in creating the additional rest mass for the associated charmed meson and anti-baryon.

These arguments are supported by the existing photoproduction data in the NA1 energy range [NASH 83]. Most convincing is the Fermilab E691 experiment, which finds associated $\Lambda_C D$ production to be less than 12% [NASH 87].

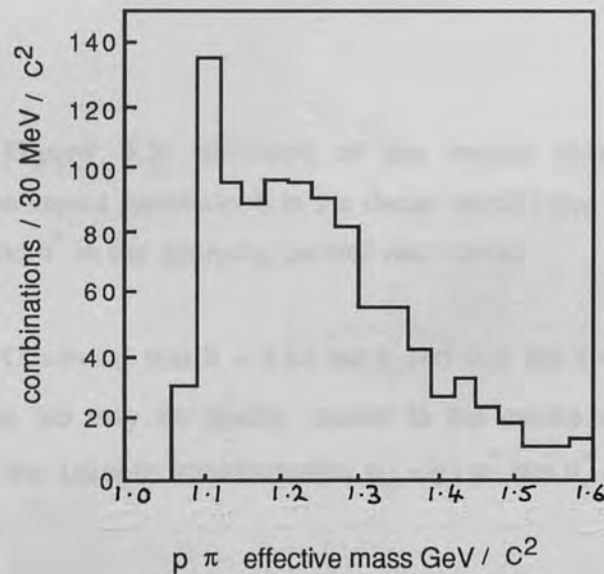


Figure 4.1: the $p\pi$ effective mass with no impact parameter cuts.

The Λ^0 is reconstructed via its $p\pi$ decay mode (branching ratio $\sim 64\%$ [PDG 86]). The $p\pi$ effective mass distribution is shown in figure 4.1 for the events satisfying the cuts (i) to (vii) outlined at the beginning of this chapter, with the added condition that the ratio of the pion momentum to the proton momentum must be less than one third, as required by the low Q value of the $\Lambda^0 \rightarrow p\pi$ decay. By exploiting the

relatively long lifetime of the Λ^0 (2.6×10^{-10} s) the background may be reduced, via a cut on the impact parameters b of the Λ^0 decay secondaries. (Note that the standard definition of the impact parameter is the length of the normal to the track projection at $z=0$, whereas here it is defined as the deviation from the track projection *in the xy plane* at $z=0$, as shown in figure 4.2. For small angles the two are approximately equivalent.)

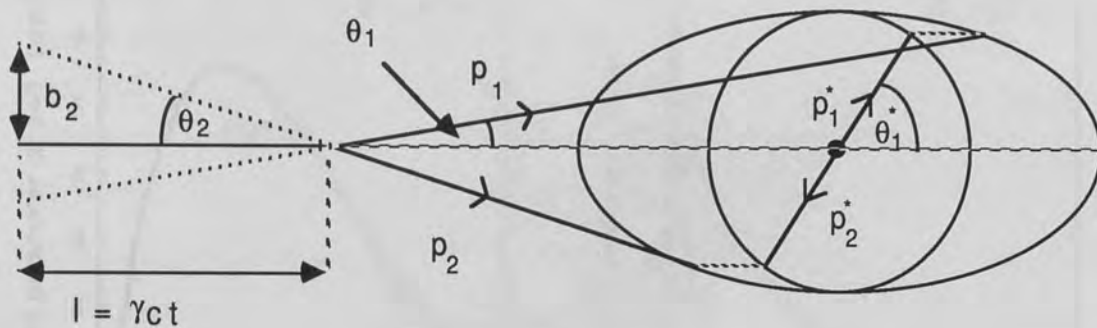


Figure 4.2: definition of the impact parameter, showing the relationship of the impact parameter b to the decay length l and polar decay angle θ in the laboratory and θ^* in the decaying particle rest frame.

Observing that $b = \gamma c t \tan \theta$ and that $\tan \theta = p_T / p_z$, the impact parameter in the lab may be readily related to the centre of mass frame decay parameters via the Lorentz transformation $p_z = \gamma (p^* \cos \theta^* + \beta E^*)$ and $p_T = p^* \sin \theta^*$, so that

$$b = \frac{c p^* t \sin \theta^*}{p^* \cos \theta^* + \beta \sqrt{m^2 + p^{*2}}} \quad (4.7)$$

Thus the impact parameter increases with the proper decay time and the decay angle, and decreases with the centre of mass energy of the secondary. Because the centre of mass energies of the secondaries are roughly in proportion to their masses in low Q value 2 body decays, the pion has the larger impact parameter.

Λ_c Analysis

For example, a break-up at 90° to the beam in the centre of mass of a 20 GeV Λ^0 will result in an angle of $\sim 0.36^\circ$ for the pion and $\sim 0.06^\circ$ for the proton. Furthermore, due to the fact that for high energy Λ^0 s the decay angle decreases linearly with energy whilst the decay length increases linearly with energy, it is clear from equation 4.7 that, in the high energy regime where β is close to 1, the impact parameter distribution is approximately independent of the energy of the decaying particle.

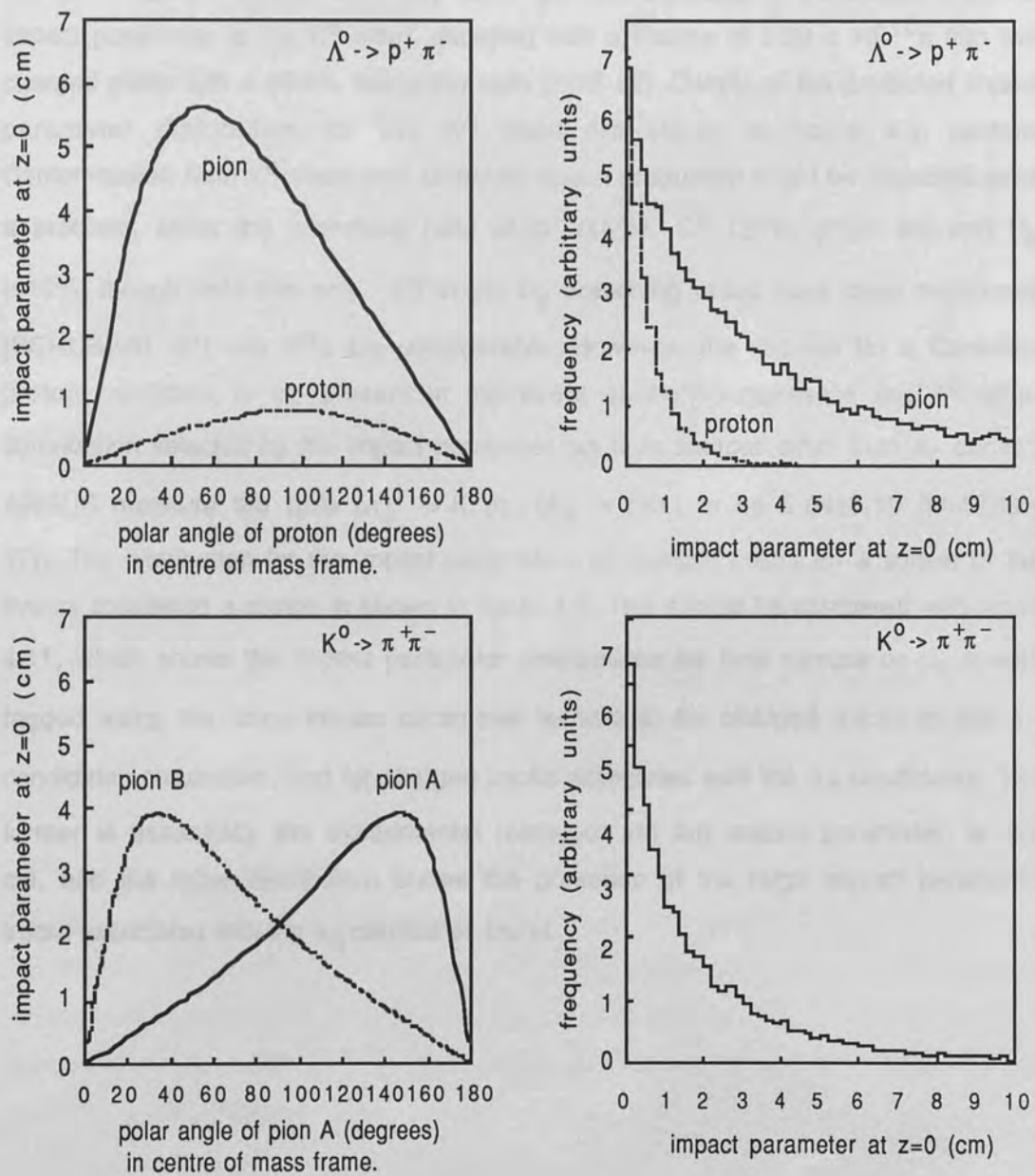


Figure 4.3: impact parameter details. Top: Λ^0 impact parameter. Below: K^0 impact parameter. The lefthand pictures illustrate the dependence of the

Λ_C Analysis

impact parameters of the decay products on the polar angle in the decaying particle's rest frame, calculated for a fixed lifetime (2.6×10^{-10} s for the Λ^0 , 0.89×10^{-10} s for the K^0). The righthand pictures show the impact parameter distributions of the decay products when the Λ^0 and K^0 lifetime distributions are used.

Details of the predicted impact parameter distribution for the Λ^0 are shown in figure 4.3, top. The only other particle expected to contribute a similar impact parameter is the K^0 short, decaying with a lifetime of 0.89×10^{-10} s into two charged pions with a 68.6% branching ratio [PDG 86]. Details of the predicted impact parameter distribution for the K^0 short are shown in figure 4.3, bottom. Contamination from K^0 short from charmed meson production might be expected to be a problem, since the branching ratio of D^+ (48%), D^0 (33%) [PDG 86] and D_s (>10%, though note that only $\sim 1/5$ of the D_s branching ratios have been measured) [SCHUBERT 87] into K^0 s are considerable. However, the request for a Cerenkov proton candidate to be present in the event strongly suppresses the K^0 short contribution selected by the impact parameter cut from sources other than Λ_C decay (ARGUS measure the ratio $(\Lambda_C \rightarrow K^0 p) / (\Lambda_C \rightarrow p K \pi)$ to be 0.84 ± 0.19 [McHUGH 87]). The distribution for the impact parameters of charged tracks for a subset of the events containing a proton is shown in figure 4.4. This should be compared with figure 4.11, which shows the impact parameter distributions for final sample of Λ_C events tagged using the large impact parameter technique; for charged tracks in the Λ_C candidate combination; and for charged tracks associated with the Λ_C candidates. The former is essentially the experimental resolution on the impact parameter, ie 0.2 cm, and the latter distribution shows the presence of the large impact parameter tracks associated with the Λ_C candidates found.

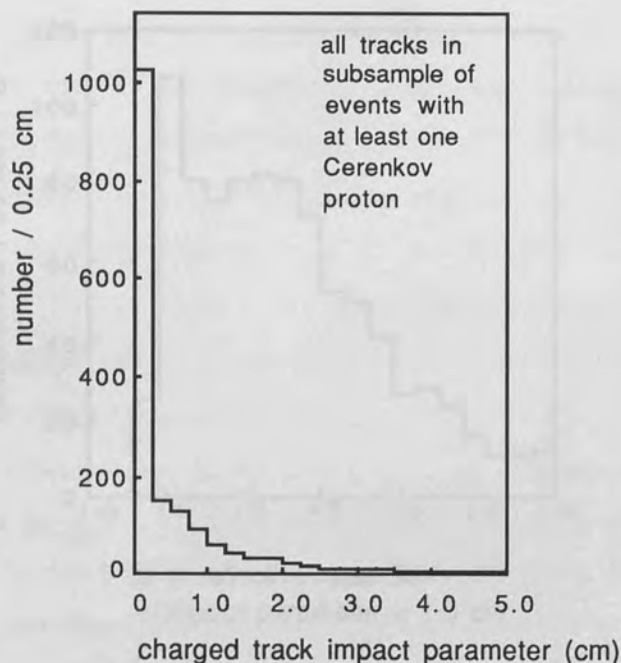
Λ_c Analysis

Figure 4.4: impact parameter distribution for charged tracks in a sample of events containing protons.

To test the hypothesis that the Λ^0 may be tagged using a large impact parameter track the $p\pi$ effective mass distribution has been studied. Note that in all the Λ^0 plots the proton is tagged by the Cerenkovs, and the pion is either identified in the Cerenkovs or of ambiguous identity. Figure 4.5 shows the distribution for both tracks with an impact parameter less than 1.0 cm. In contrast, figure 4.6 shows the $p\pi$ effective mass distribution when the pion is required to have an impact parameter greater than or equal to 1.0 cm. The Λ^0 , which was visible on a large background (the rapid tail-off at higher masses of this background is due to the $p_\pi/p_p \leq 0.35$ cut) in the plot with no impact parameter cut (figure 4.1), is clearly visible in both figures 4.5 and 4.6. However, in terms of signal to noise the Λ^0 obtained using the impact parameter cut is of superior quality. It is apparent therefore that the demand for a large impact parameter pion in an event is an effective way of selecting Λ^0 and rejecting background.

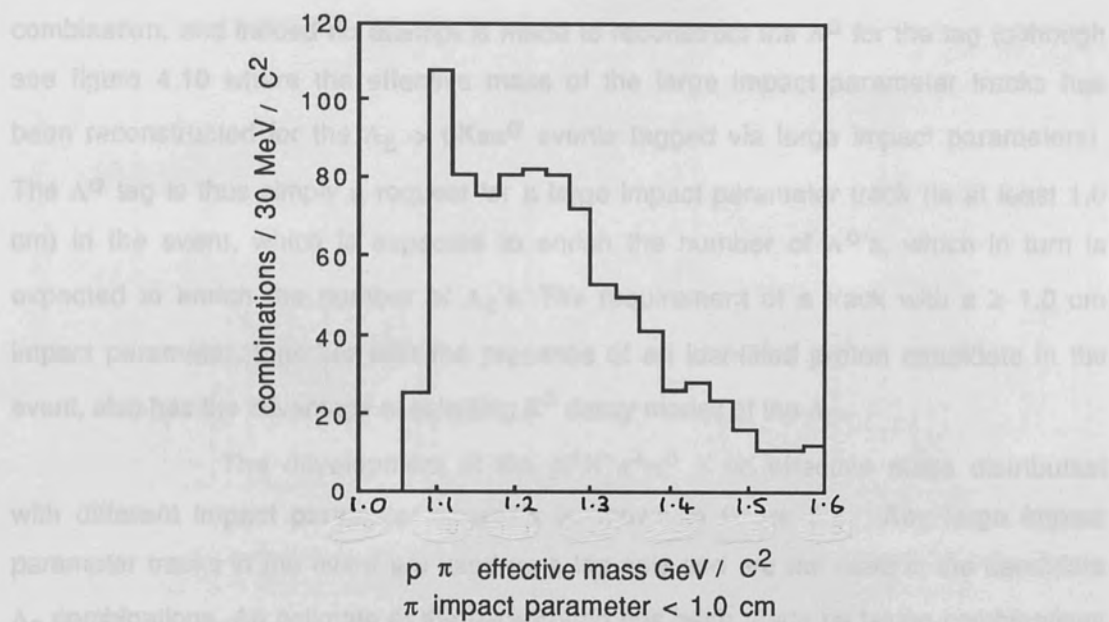
Λ_C Analysis

Figure 4.5

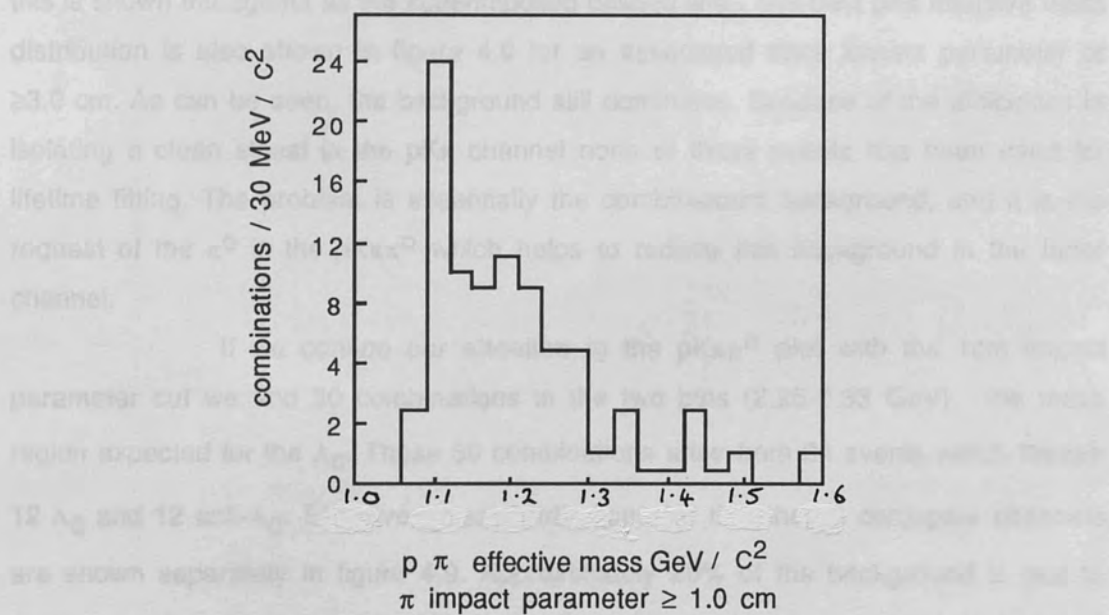


Figure 4.6.

The number of entries in the $p\pi$ effective mass distributions is dominated by the number of flagged protons. In the practical case of tagging Λ_C via a Λ^0 being present in the same event an unambiguous proton will not be required for the Λ^0

Λ_C Analysis

combination, and indeed no attempt is made to reconstruct the Λ^0 for the tag (although see figure 4.10 where the effective mass of the large impact parameter tracks has been reconstructed for the $\Lambda_C \rightarrow pK\pi\pi^0$ events tagged via large impact parameters). The Λ^0 tag is thus simply a request for a large impact parameter track (ie at least 1.0 cm) in the event, which is expected to enrich the number of Λ^0 's, which in turn is expected to enrich the number of Λ_C 's. The requirement of a track with a ≥ 1.0 cm impact parameter, together with the presence of an identified proton candidate in the event, also has the advantage of selecting K^0 decay modes of the Λ_C .

The development of the $p^+K^-\pi^+\pi^0 + cc$ effective mass distribution with different impact parameter requests is shown in figure 4.7. Any large impact parameter tracks in the event are used as a tag only and are not used in the candidate Λ_C combinations. An estimate of the background has been made by taking combinations with the wrong charge kaon (ie combinations with p and K either both positive or both negative, which could only have come from Cabbibo-suppressed decay modes), and this is shown throughout as the superimposed dashed line. The best $pK\pi$ effective mass distribution is also shown in figure 4.8 for an associated track impact parameter of ≥ 3.0 cm. As can be seen, the background still dominates. Because of the difficulties in isolating a clean signal in the $pK\pi$ channel none of these events has been used for lifetime fitting. The problem is essentially the combinatorial background, and it is the request of the π^0 in the $pK\pi\pi^0$ which helps to reduce this background in the latter channel.

If we confine our attention to the $pK\pi\pi^0$ plot with the 1cm impact parameter cut we find 30 combinations in the two bins (2.25-2.33 GeV), the mass region expected for the Λ_C . These 30 combinations arise from 24 events which feature 12 Λ_C and 12 anti- Λ_C . Effective mass distributions for the charge conjugate channels are shown separately in figure 4.9. Approximately 20% of the background is due to events with a good Λ_C candidate in the peak, and in particular the small enhancement in the wrong sign kaon distribution between 2.21 GeV and 2.25 GeV (the dashed line in the bin left adjacent to the peak) is almost completely due to events with a good Λ_C combination in the peak.

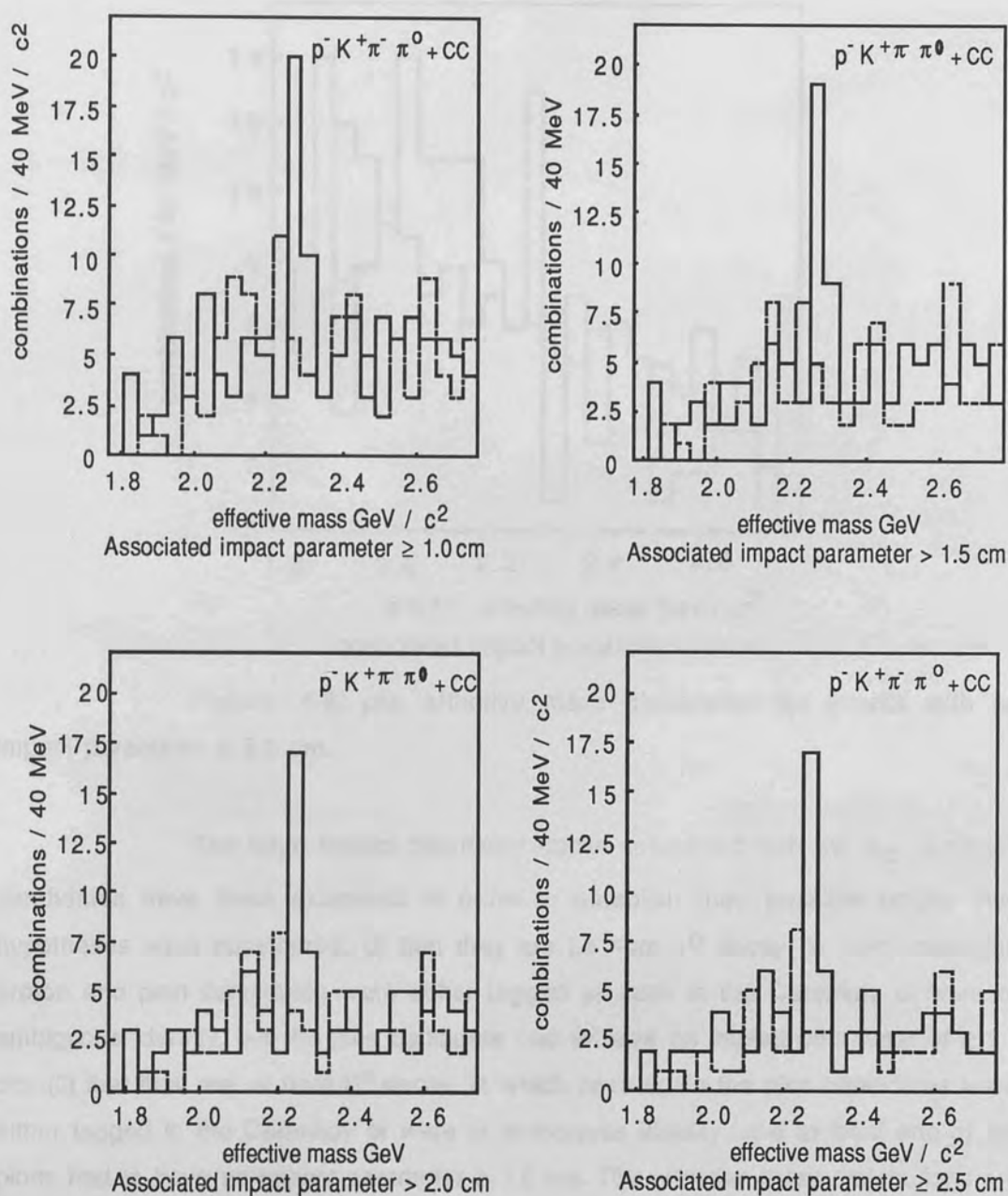
Λ_c Analysis

Figure 4.7: $p^- K^+ \pi^- \pi^0 + cc$ effective mass distributions for different impact parameter tags. The dashed line represents the distribution for $p^- K^- \pi^+ \pi^0 + cc$ evaluated under the same conditions.

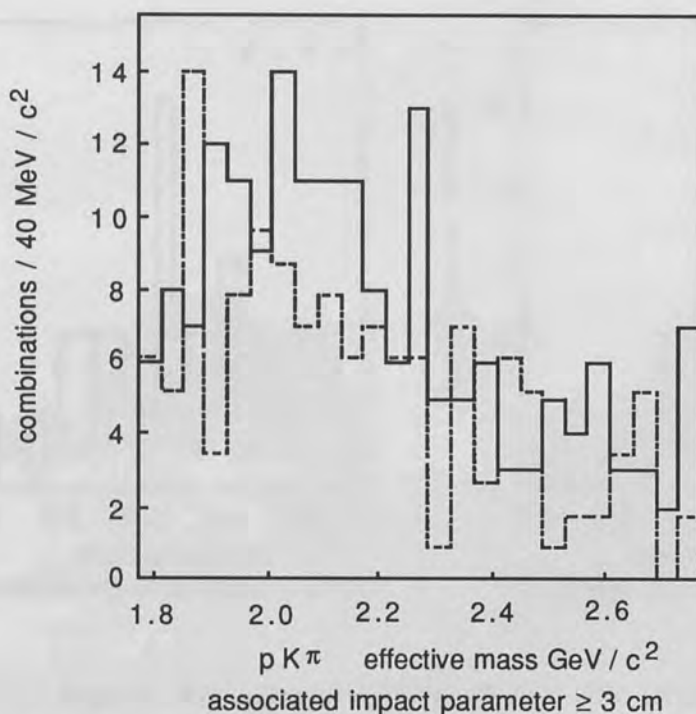
Λ_C Analysis

Figure 4.8: $pK\pi$ effective mass distribution for events with an impact parameter ≥ 3.0 cm.

The large impact parameter tracks associated with the $\Lambda_C \rightarrow pK\pi^0$ candidates have been examined in order to establish their possible origin. Two hypotheses were considered: (i) that they are $p\pi$ from Λ^0 decay, in which case the proton and pion candidates were either tagged as such in the Cerenkov or were of ambiguous identity, but the pion candidate had to have an impact parameter of ≥ 1.0 cm; (ii) that they are $\pi\pi$ from K^0 decay, in which case again the pion candidates were either tagged in the Cerenkov or were of ambiguous identity, and at least one of the pions had to have an impact parameter ≥ 1.0 cm. The effective mass distributions are shown for cases (i) and (ii) in figure 4.10 below. There is evidence that they originated from Λ^0 decay - there are five $p\pi$ combinations falling at the Λ^0 mass with negligible background, whilst not one $\pi\pi$ combination is compatible with K^0 decay. The discrepancy in numbers of Λ^0 and Λ_C (ie there are 24 Λ_C events and only 5 Λ^0 's in the associated large impact parameters) is most probably due to loss of Λ^0 caused by limited reconstruction efficiency, particularly in the case where the decay occurs well into FRAMM, and one of the tracks (ie the proton) is measured badly or not at all.

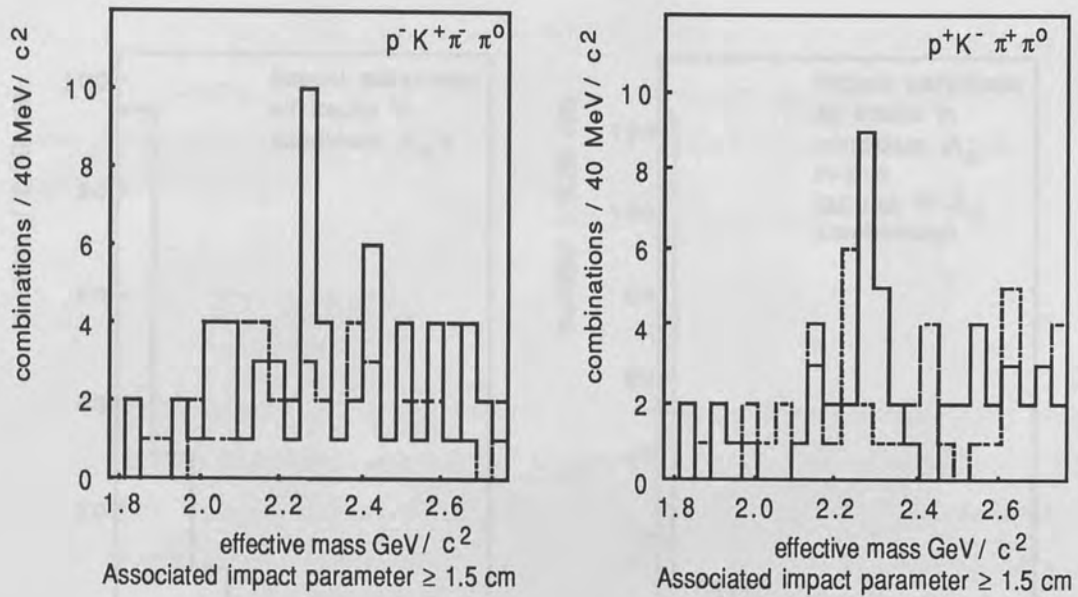
Λ_C Analysis

Figure 4.9: (above) $p^- K^+ \pi^- \pi^0$ and $p^+ K^- \pi^+ \pi^0$ effective mass distributions obtained using an impact parameter tag of ≥ 1.5 cm.

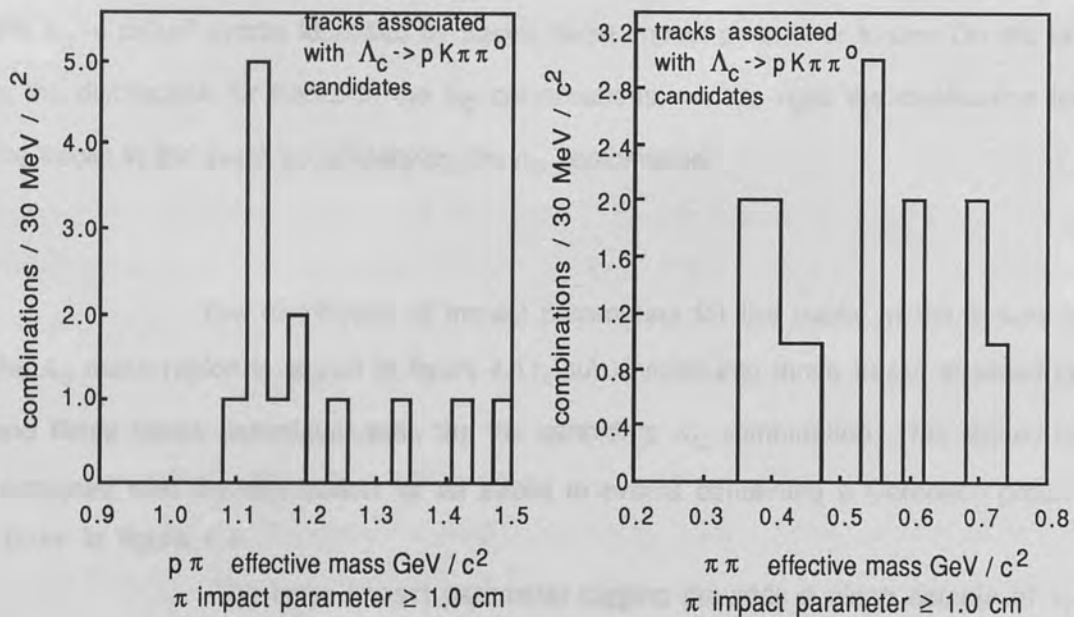


Figure 4.10: effective mass distributions for the tracks associated with the $\Lambda_C \rightarrow p K \pi \pi^0$ candidates tagged via the large impact parameter under the hypothesis that they are $p\pi$ (left) or $\pi\pi$ (right). (see text).

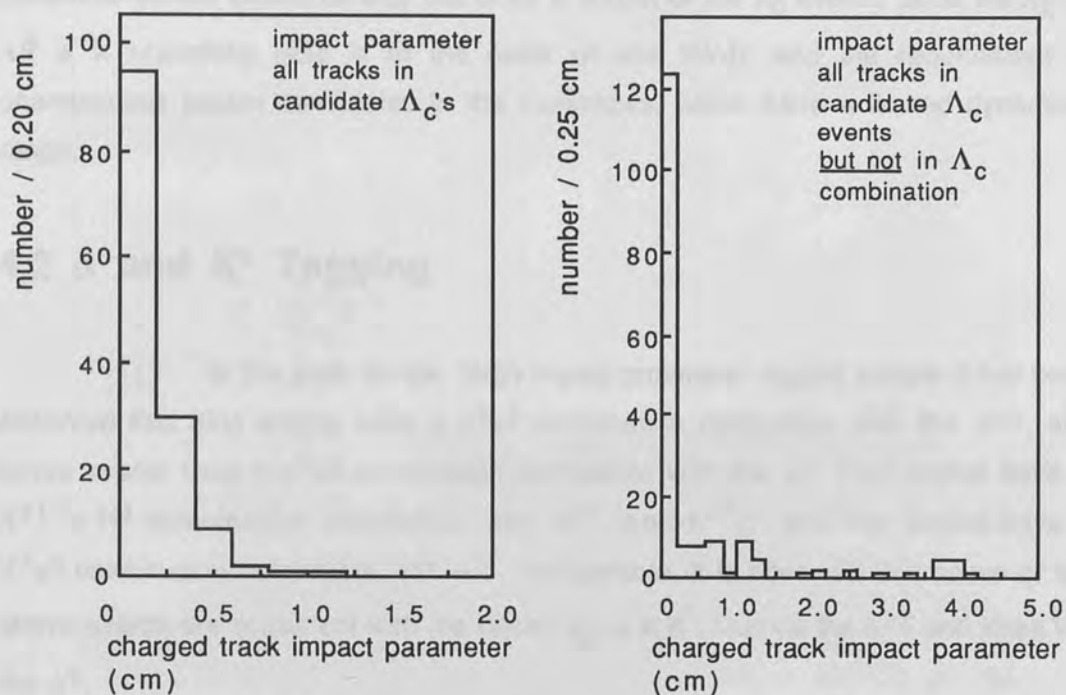
Λ_C Analysis

Figure 4.11: impact parameter distributions for charged tracks in the $\Lambda_C \rightarrow pK\pi\pi^0$ events identified by having large impact parameter tracks. On the left is the distribution for tracks in the Λ_C combinations, on the right the distribution for the tracks in the event accompanying the Λ_C combination.

The distribution of impact parameters for the tracks in the events in the Λ_C mass region is shown in figure 4.11, sub-divided into those tracks included in, and those tracks associated with, the the candidate Λ_C combination. This should be compared with the distribution for all tracks in events containing a Cerenkov proton, shown in figure 4.4.

The large impact parameter tagging provides a clean sample of Λ_C events. However, the target analysis (see section 4.3 below) reveals that less than half these events are suitable for lifetime measurements. In order to increase statistics this Λ_C sample has been studied for suitable selection criteria which would allow a larger sample of Λ_C 's by relaxing the highly restrictive cuts: i.e. on the impact

parameter (which should be only useful for a subset of the Λ_c events, since the $\Lambda_c \rightarrow \Lambda^0 + X$ branching ratio is of the order of one third); and the requirement of unambiguous proton candidates in the Cerenkovs, which have a limited dynamical range.

4.2 Δ and K^* Tagging

In the peak for the large impact parameter tagged sample it has been observed that nine events have a $p^\pm\pi^\pm$ combination compatible with the $\Delta^{\pm\pm}$, and seven events have a $p^\pm\pi^0$ combination compatible with the Δ^\pm . Four events have a $K^{+(-)}\pi^{-(+)}$ combination compatible with K^{0*} (anti- K^{0*}); and five events have a $K^\pm\pi^0$ combination compatible with $K^{\pm*}$. Furthermore, it is observed that seven of the above events are consistent with the decay $\Lambda_c \rightarrow \Delta K^*$, four via the $\Delta^{\pm\pm}$ and three via the Δ^\pm .

Compatibility with the Δ is defined by the $p\pi$ combination falling between 1.16 GeV and 1.3 GeV, and the additional constraint that the ratio of the pion momentum to the proton momentum must not exceed 0.7, as determined by the kinematics of the decay. The K^* is simply defined by the $K\pi$ combination falling between 0.85 GeV and 0.93 GeV.

A study of the $p^-K^+\pi^-\pi^0$ and $p^+K^-\pi^+\pi^0$ effective mass distributions *without* the impact parameter tag has been made, in order to include a statistically significant sample size. The peak region has been analysed and all $p\pi$ and $K\pi$ effective masses have been plotted. A region of the wrong sign kaon background around the Λ_c mass and with comparable statistics has been treated in the same way (note that in this case the reconstructed delta resonance is Δ^0). Figure 4.12 shows triangle plots for the two cases. There are bands evident at the Δ and K^* in the left hand plot which are not present in the control sample (right hand side). In particular a cluster is apparent in the region of intersection of the Δ and K^* masses. The projections onto x (y) of the scatter plots in figure 4.12 are shown in figures 4.13 (4.14) for greater clarity.

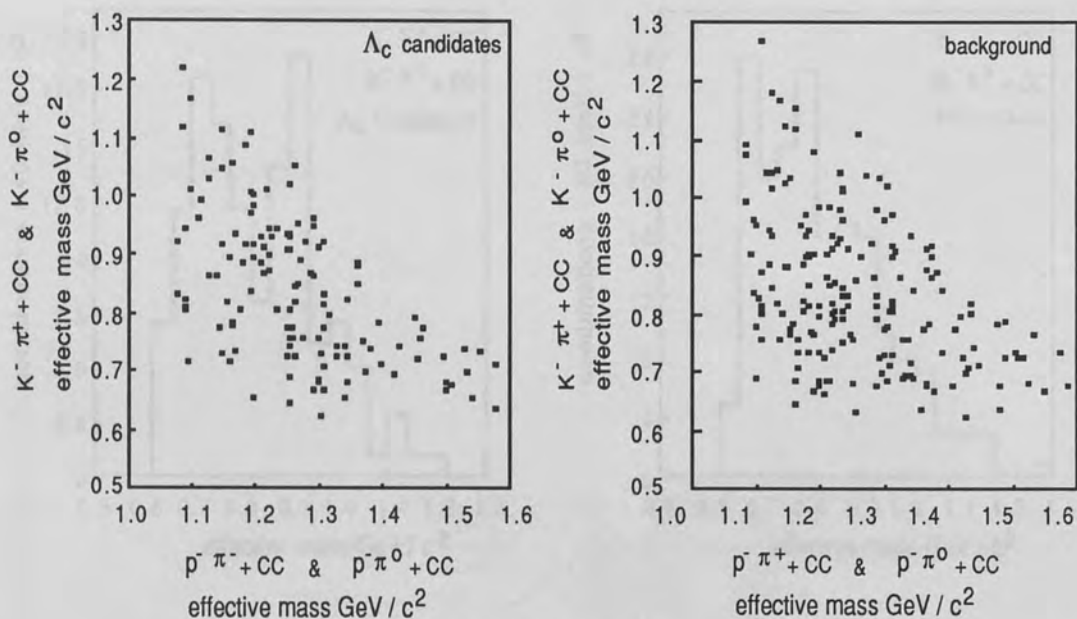
Λ_c Analysis

Figure 4.12: triangle plots showing evidence of resonant substructure in the $p^-K^+\pi^-\pi^0$ and $p^+K^-\pi^+\pi^0$ channels.

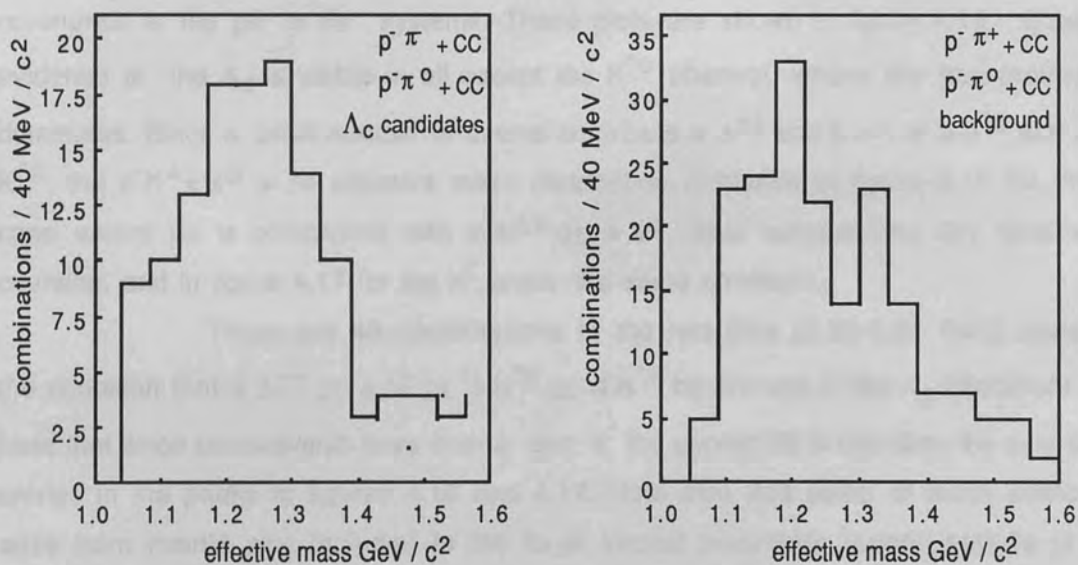


Figure 4.13: $p\pi$ effective mass distributions for events in the peak (left) and the background (right). The Δ can be seen as an enhancement between 1.2 and 1.3 GeV in the left hand plot.

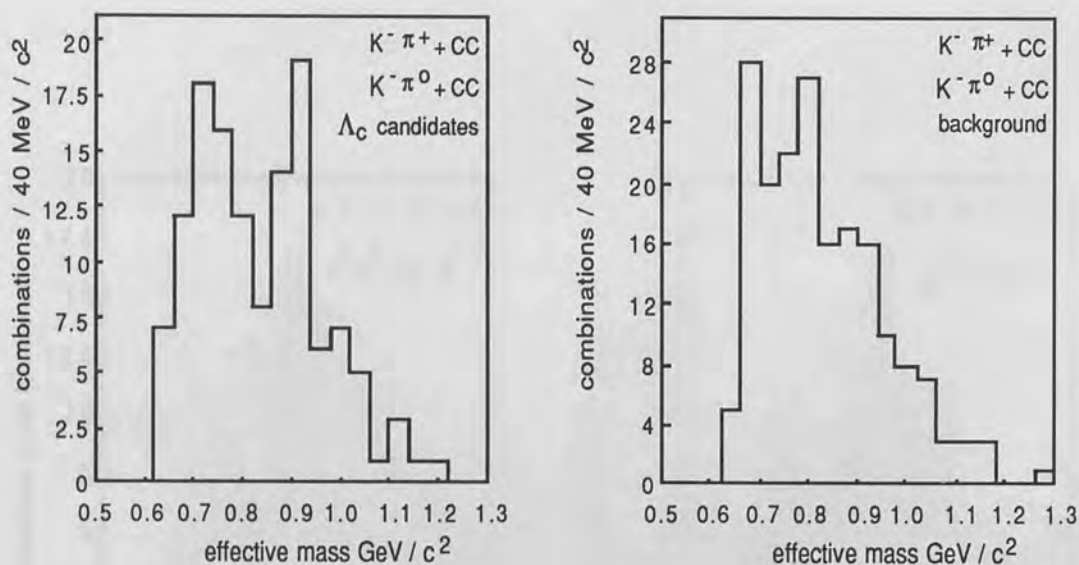
Λ_C Analysis

Figure 4.14: $K\pi$ effective mass distributions. The K^* stands out clearly in the two bins around 0.9 GeV in the left hand plot.

Accordingly the large impact parameter tag has been dropped and the $p^-K^+\pi^-\pi^0$ and $p^+K^-\pi^+\pi^0$ effective mass distributions plotted when there is a resonance in the $p\pi$ or $K\pi$ systems. These plots are shown in figure 4.15. Clear evidence of the Λ_C is visible in all except the K^{*0} channel, where the background dominates. Since a small number of events contribute a $\Delta^{\pm\pm}$ and a Δ^\pm , or a K^{*0} and a $K^{*\pm}$, the $p^-K^+\pi^-\pi^0 + cc$ effective mass distribution is shown in figure 4.16 for the case where $p\pi$ is compatible with a $\Delta^{\pm\pm}$ or a Δ^\pm , thus suppressing any double counting, and in figure 4.17 for the K^* under the same condition.

There are 48 combinations in the two bins (2.25-2.33 GeV) under the condition that a $\Delta^{\pm\pm}$ or a Δ^\pm or a K^{*0} or a $K^{*\pm}$ be present in the Λ_C candidate. Note that since some events have both Δ and K^* the quoted 48 is less than the sum of entries in the peaks in figures 4.16 and 4.17. Note also that some of these entries arise from events also included in the large impact parameter tagged sample (17 events are common to both samples). The 48 combinations come from 37 events, 21 Λ_C^- and 16 Λ_C^+ . There are 20 events best fit using $\Delta^{\pm\pm}$ and 16 events best fit with Δ^\pm . There are 8 events with K^{*0} and 11 events with $K^{*\pm}$. In addition there are 9 $\Lambda_C \rightarrow \Delta^{++} K^{*-} + cc$ and 6 $\Lambda_C \rightarrow \Delta^+ K^{*0} + cc$ events. Again, approximately 20% of the combinatorial background is due to events with good Λ_C candidates in the peak.

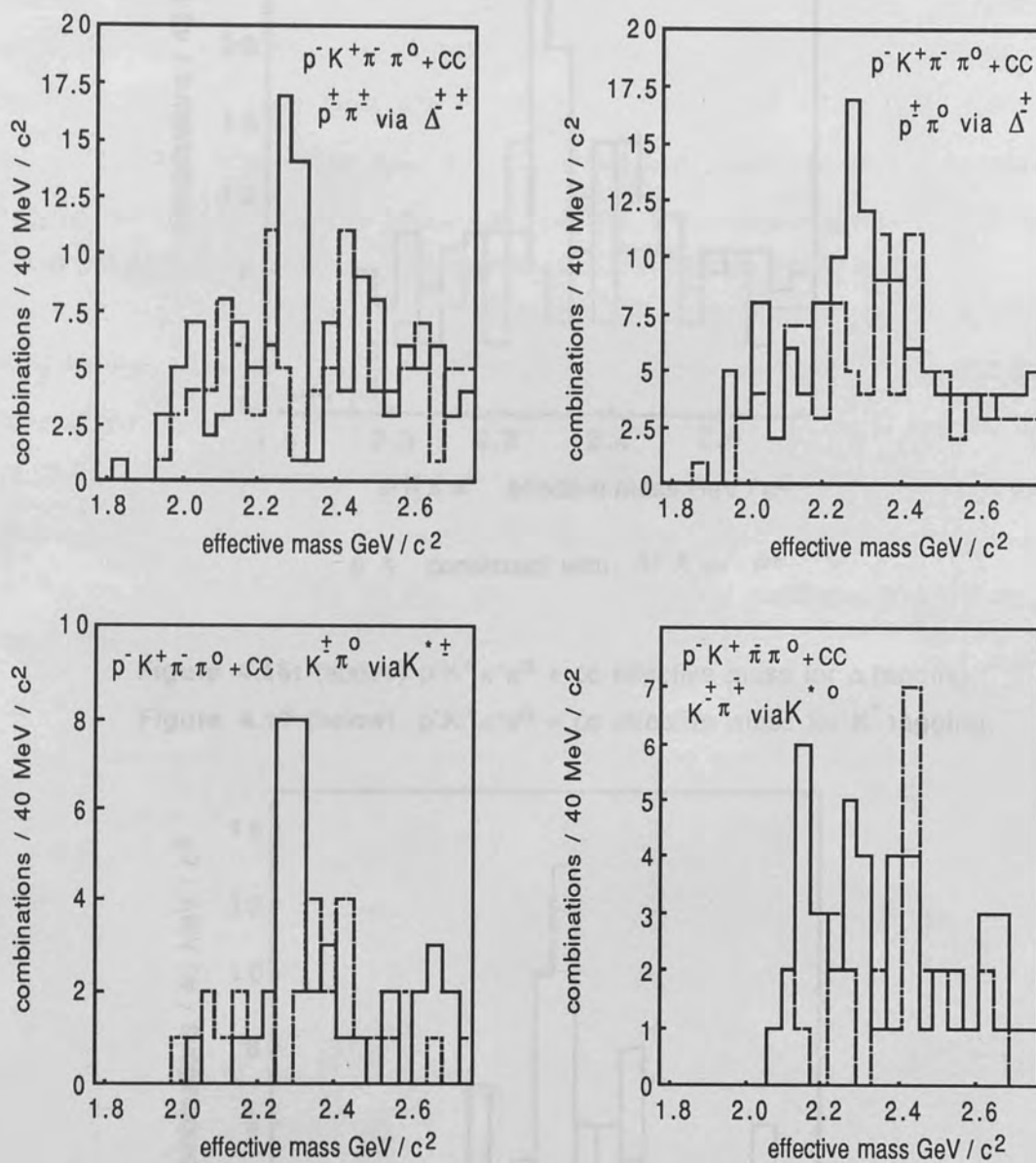
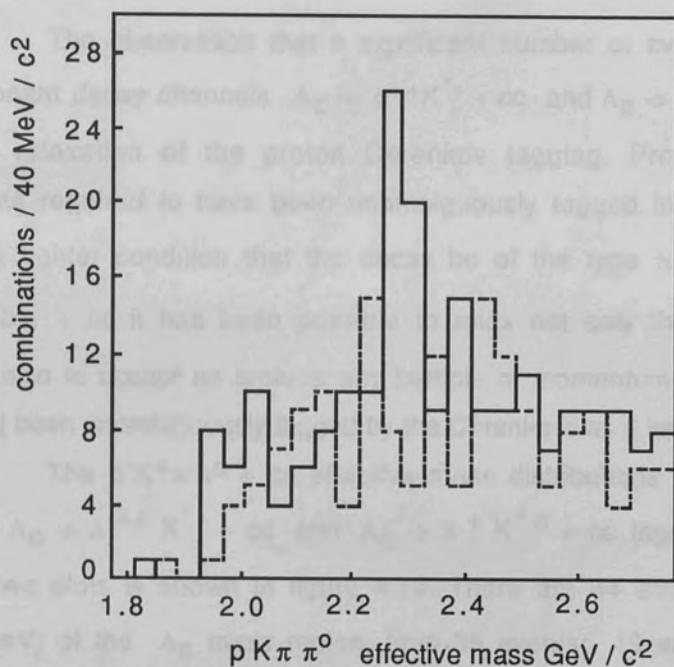
Λ_C Analysis

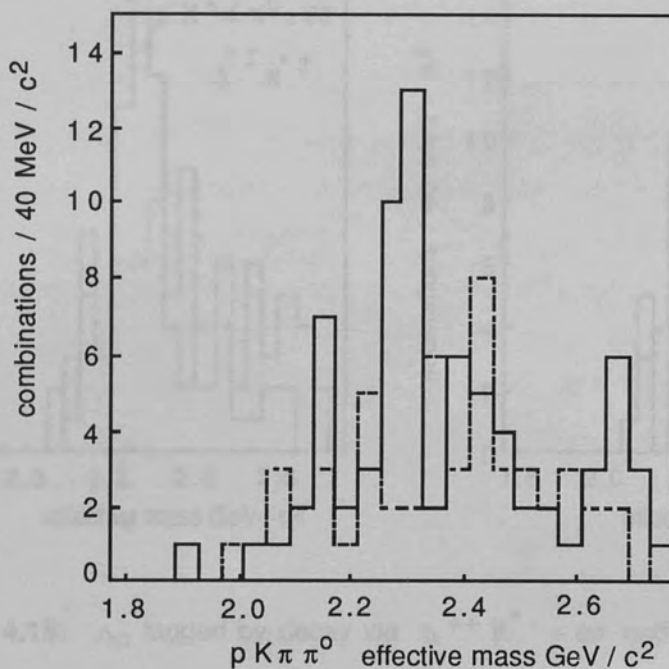
Figure 4.15: $p^- K^+ \pi^- \pi^0 + cc$ effective mass for resonance tagging. The impact parameter tag has been dropped.

Δ_C Analysis

$p \pi$ consistent with Δ^{++} or Δ^+

Figure 4.16: (above) $p^-K^+\pi^-\pi^0 + cc$ effective mass for Δ tagging.

Figure 4.17 (below) $p^-K^+\pi^-\pi^0 + cc$ effective mass for K^* tagging.



$K \pi$ consistent with K^{*+} or K^{*0}

Λ_C Analysis

The observation that a significant number of events are compatible with the resonant decay channels $\Lambda_C \rightarrow \Delta^{++}K^{*-} + cc$ and $\Lambda_C \rightarrow \Delta^+K^{*0} + cc$ has allowed the relaxation of the proton Cerenkov tagging. Previously, the proton candidate was required to have been unambiguously tagged in the Cerenkovs. By imposing the tighter condition that the decay be of the type $\Lambda_C \rightarrow \Delta^{++}K^{*-} + cc$ or $\Lambda_C \rightarrow \Delta^+K^{*0} + cc$ it has been possible to relax not only the impact parameter tagging, but also to accept as protons any particle of momentum greater than 5 GeV which has not been unambiguously tagged by the Cerenkovs as a kaon or a pion.

The $p^-K^+\pi^-\pi^0 + cc$ effective mass distributions are shown in figure 4.18 for the $\Lambda_C \rightarrow \Delta^{++}K^{*-} + cc$ and $\Lambda_C \rightarrow \Delta^+K^{*0} + cc$ tagging case, and the sum of the two plots is shown in figure 4.19. There are 44 entries in the two bins (2.25-2.33 GeV) of the Λ_C mass region, from 35 events: 19 are Λ_C^+ and 16 Λ_C^- . The resonant decay channel breakdown is 19 $\Lambda_C \rightarrow \Delta^{++}K^{*-} + cc$ and 16 $\Lambda_C \rightarrow \Delta^+K^{*0} + cc$. 16 events of the 35 are common to the impact parameter tag and single resonance tag samples.

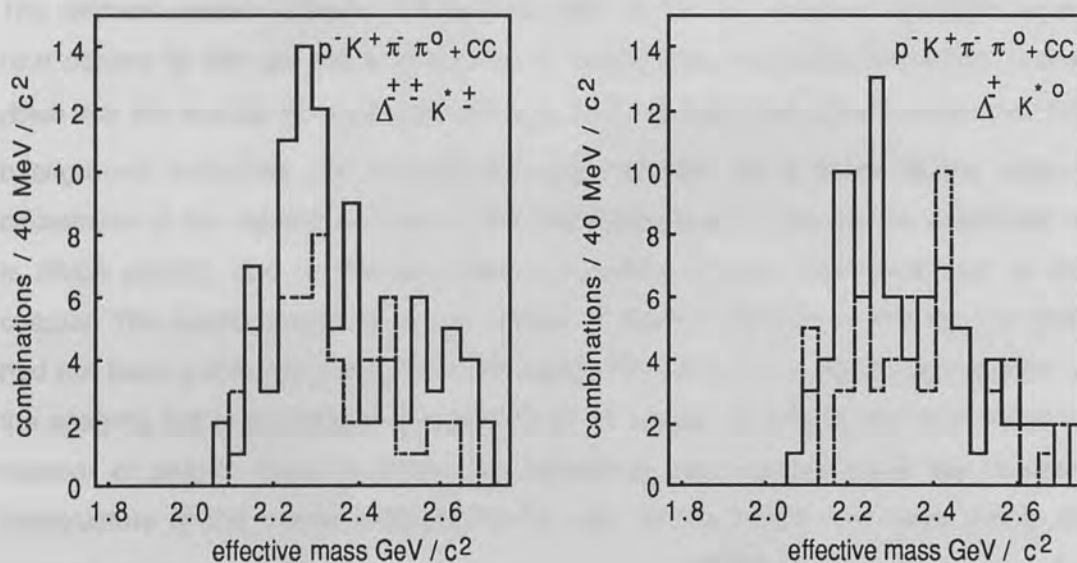


Figure 4.18: Λ_C tagged by decay via $\Delta^{++}K^{*-} + cc$ and $\Delta^+K^{*0} + cc$.

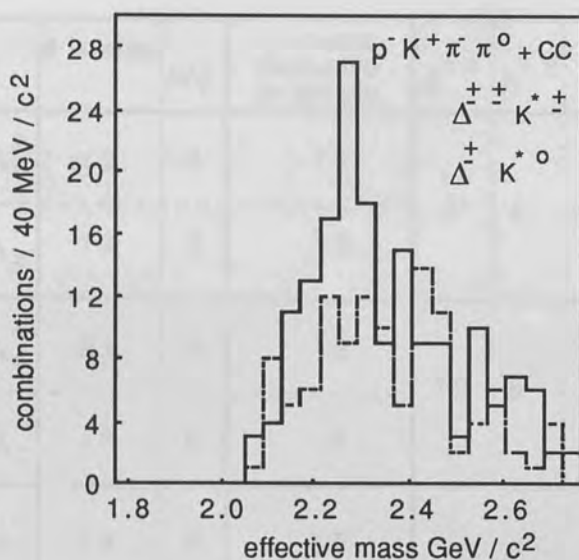
Λ_C Analysis

Figure 4.19: sum of $\Lambda_C \rightarrow \Delta^{++} K^{*-} + cc$ and $\Lambda_C \rightarrow \Delta^+ K^{*0} + cc$.

The salient features of the Λ_C samples tagged using the different methods described above are summarised in table 4.1 below. Since the final sample has been arrived at via diverse procedures the table itself deserves some explanation. The leftmost column indicates the method used to tag the sample in question. In the next column to this are the total number of events that this method selected, broken down into the number of Λ_C 's and anti- Λ_C 's, with an estimate of the background. The background estimates are approximate and intended as a guide to the relative cleanliness of the tagging technique - the true background to the lifetime measurement is much smaller due to the event/target matching criteria described later in this chapter. The middle column gives the number of events *exclusive* to that tag, i.e. which had not been previously found, which of course depends on the chronological order of the analysis, but is intended to give an idea of the degree of overlap and to develop the number of events found in total. The second to right column gives the resonant substructure of the events exclusive to this tag, for the bottom two rows this is the number of $\Lambda_C \rightarrow \Delta^{++} K^{*-} + cc$ and $\Lambda_C \rightarrow \Delta^+ K^{*0} + cc$ events found. The rightmost column summarises the D_S ambiguities, described below.

Λ_C Analysis

sample tagged by		# events	b/g	# events exclusive to sample	$\Delta^{\pm\pm}$	$K^{*\pm}$	Δ^\pm	K^{*0}	D_S Ambiguities
impact parameter	Λ_c^+	12	3	12					4
	Λ_c^-	12	3	12	7	4	9	5	
$\Delta^{\pm\pm}$ Δ^\pm $K^{*\pm}$ K^{*0}	Λ_c^+	21	8	12					1
	Λ_c^-	16	6	8	12	5	8	3	
$\Delta^{\pm\pm}K^*$ $\Delta^\pm K^*$	Λ_c^+	19	6	9					2
	Λ_c^-	16	5	10	10		9		
total	Λ_c^+	52	17	33 (10)					7
	Λ_c^-	44	14	30 (9)	19		16		

Table 4.1: $\Lambda_C \rightarrow pK\pi\pi^0$ event summary.

There exists an ambiguity between the the $D_S(1.97 \text{ GeV})$ and the $\Lambda_C(2.28 \text{ GeV})$ when one of the kaons from D_S decay is treated as a proton in reconstructing the effective mass of D_S decay secondaries. This kinematical reflection is strong in the $D_S \rightarrow KK\pi$ channel, where the maximum of the broad reflected peak falls between 2.17 GeV and 2.37 GeV, centred on the region of the expected Λ_C mass. The reflection is also strong for the $D_S \rightarrow KK\pi\pi^0$ channel, although the broad peak is now in the 2.25 GeV - 2.45 GeV region, and only the lower edge coincides with the Λ_C mass. Thus, in order to ascertain the degree of contamination from D_S events misidentified as Λ_C , the events from the peak region of all three tagged Λ_C samples have been analysed under the hypothesis that the proton candidate is a kaon. The effective mass distribution is shown in figure 4.20 below. There is no evidence that

Λ_C Analysis

the observed Λ_C peak is a reflection of D_S events. Note that while there are on average 1.2 combinations per event in figure 4.20, three entries in the 1.99 - 2.01 GeV bin come from one event, and this is therefore regarded as a statistical fluctuation. Nevertheless, seven events do have a mass compatible with the D_S (i.e. between 1.96 and 1.98 GeV), and in order to prevent any possible bias to the lifetime measurement these have been excluded from the final lifetime fit.

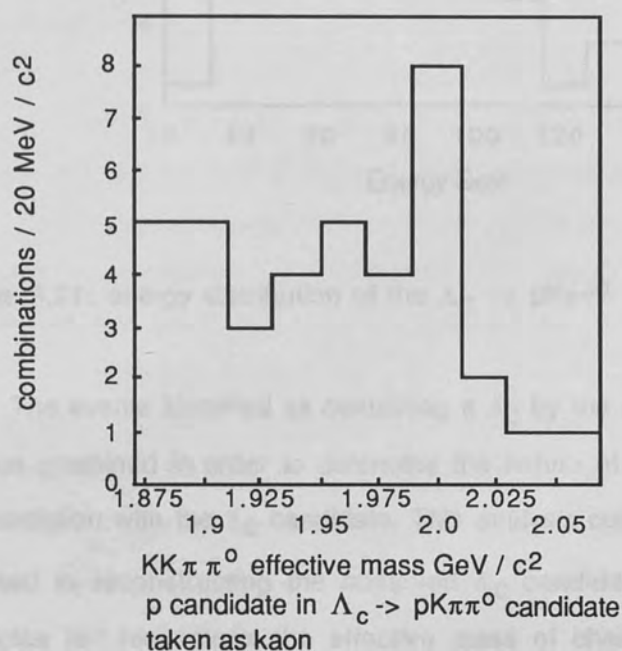


Figure 4.20: effective mass in the D_S region for events in the Λ_C peak when the proton is regarded as a kaon.

The energy distribution for the $\Lambda_C \rightarrow pK\pi\pi^0$ final sample is shown in figure 4.21.

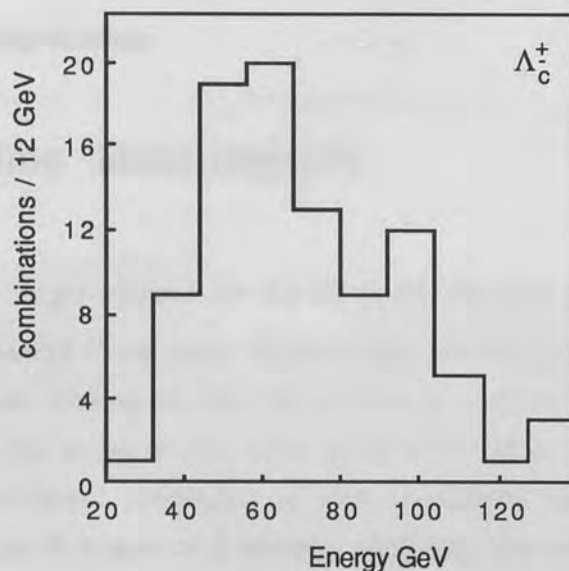
Λ_C Analysis

Figure 4.21: energy distribution of the $\Lambda_C \rightarrow pK\pi\pi^0$ final sample.

The events identified as containing a Λ_C by the procedures described above have been examined in order to determine the nature of the charmed particle produced in association with the Λ_C candidate. This analysis consists of excluding all the particles used in reconstructing the observed Λ_C candidate, and using all the remaining particles to reconstruct the effective mass of charmed particles in the channels with the largest branching ratios observable in FRAMM, namely: $\Lambda_C \rightarrow pK\pi\pi^0, pK\pi, \Lambda^0\pi$, and $\Lambda^0\pi\pi\pi$; $D_S \rightarrow KK\pi$; $D^+ \rightarrow K\pi\pi, K\pi\pi\pi^0$; and $D^0 \rightarrow K\pi, K\pi\pi, K\pi\pi\pi$. No combinations compatible with the D_S, D^+ , or D^0 masses were found. Four events were found to contain, in addition to the already identified $\Lambda_C \rightarrow pK\pi\pi^0$ candidate, a Λ_C combination compatible with the Λ_C mass. Three of these are in the channel $\Lambda_C \rightarrow pK\pi$, and one in $\Lambda_C \rightarrow \Lambda^0\pi\pi\pi$. The target readouts for the former three events are in saturation, whilst the latter, tagged via the large impact parameter from the Λ^0 decay, has a single step of two but where there are twelve strips in saturation at the production point, believed to be due to incoherent production, and possibly masking the other decay step of two. This event was not used for the lifetime measurement. The reconstruction of four exclusive Λ_C anti- Λ_C events and no $\Lambda_C D$ events lends weight to the belief that the principal production mechanism is Λ_C anti- Λ_C pair production as

opposed to associated production.

4.3 Λ_C Lifetime Measurement

The target pictures for the 63 events isolated in the Λ_C peak have been subjected to careful visual scan. As previously pointed out the initial target cut on the data was loose, making no veto on the level of noise in the target event, and consequently 24 of the target events were found to be all or largely in saturation, compatible with incoherent production or high multiplicity events (the most the target can discriminate is a level of 8 charged particles). The visual scan results are summarised in table 4.2 below. Any obvious errors of the target scanning program (for example where the program had invented steps on a steeply falling edge, or fallen into a 'hole' at the back of the target) were corrected by the visual scan. Examples of the target readout are shown in figure 4.22.

Due to the inclusive nature of the analysis no information exists on the associated charm particle in the event. We do know, however, that the candidates isolated in the sample of $\Lambda_C \rightarrow pK\pi\pi^0$ events must necessarily decay with a change of charge multiplicity of two. Useful events are therefore defined as target pictures where, in addition to the production step, there is a single step of 2 or a step of two

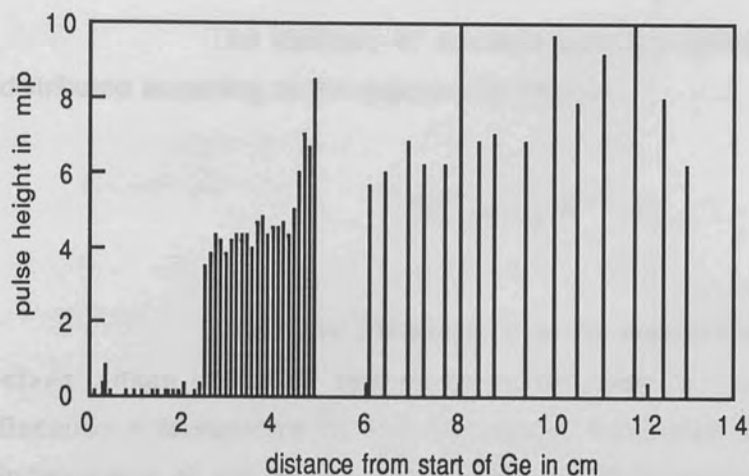
Target event type	number
incoherent / saturation	24
production + single step of 2	13
production + 2 steps of 2	3
production + step of 2 and step of 4	15
production + single step of 4	8

Table 4.2: Summary of target configurations for the Λ_C sample.

Λ_C Analysis

accompanied by a step other than two, so that the γ factor of the Λ_C may be assigned to the decay length. Thus 28 events are accessible to the lifetime measurement (see table 4.2). Of these 28 events four are ambiguous with the D_S and are dropped from the sample. The remaining 24 events have 12 target pictures of 0-2-6-8 or 0-2-4-8 configurations, and the assignment of the $\Lambda_C \gamma$ factor to decay length is unambiguous, and 12 target events showing a single step of 2 besides the production step. For the single step of two in the target it is highly likely that this is the decay step of the reconstructed Λ_C and that the associated particle decays with a charge multiplicity change of zero or outside the acceptance of the target, but nevertheless the assignment of the $\Lambda_C \gamma$ factor to decay length is ambiguous. The confusion arises if the associated particle decays with a multiplicity change of 2 and the reconstructed Λ_C decays outside the acceptance of the target.

If the lifetime of the Λ_C is of the order of $2 \times 10^{-13} \text{ s}$ ($c\tau \sim 0.007 \text{ cm}$) and the target volume therefore scans a maximum of ~ 6 mean lifetimes (depending of course on the production point) for a Λ_C with a γ factor of 30 (the average of the sample) then it is most unlikely that any Λ_C s decay beyond the end of the target. There is, however, the possibility that the reconstructed Λ_C decays so close to the production point that it is unresolvable, giving a production step of 4, whilst the associated particle decays with a charge change of 2 and the γ factor is wrongly assigned to this decay. Note that this effect is relevant to only half of the measured decay times. In addition there is the further possibility that the step of two is the result of one of the photons from the π^0 converting to e^+e^- . Both effects have been studied using the target monte carlo and the results are presented following the lifetime measurement.

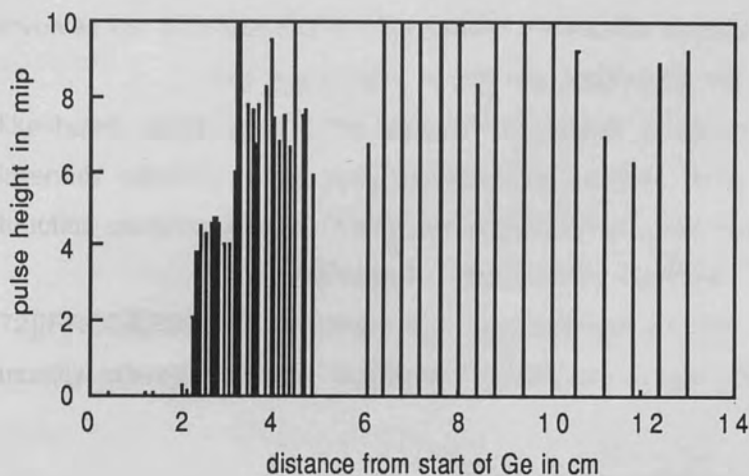
Λ_C Analysis

RUN 7463 EVENT 20451

 Λ_C^+ CANDIDATEENERGY = 76.5 GeV/c²

0 - 4 - 6

DECAY TIME = 0.199 ps

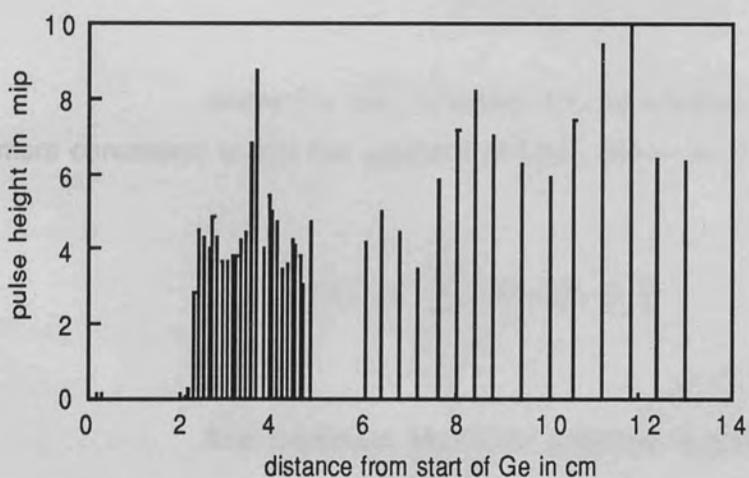


RUN 7463 EVENT 6920

 Λ_C^- CANDIDATEENERGY = 96.4 GeV/c²

0 - 4 - 6

DECAY TIME = 0.070 ps



RUN 7640 EVENT 13303

 Λ_C^- CANDIDATEENERGY = 101.3 GeV/c²

0 - 4 - 6

DECAY TIME = 0.408 ps

Figure 4.22: examples of target events from the Λ_C sample.

Λ_C Analysis

The lifetimes of unstable particles decaying randomly in time are distributed according to the exponential function

$$f(t) = \frac{1}{\tau} e^{-t/\tau} \quad (4.8)$$

where the parameter τ is the expectation value of the distribution $\langle t \rangle = \tau$, more commonly referred to as the mean lifetime, and the variance is τ^2 . Because τ is constant for the exponential distribution the probability of decay is independent of the history of the particle - frequently stated as 'the exponential distribution has no memory'. Measurement of the mean lifetime of the Λ_C thus involves the estimation of the parameter τ from the lifetime data sample.

The parameter τ will be estimated via the method of maximum likelihood, which avoids the loss of information incurred in grouping the data into intervals required for an estimate via least squares fitting. In contrast the likelihood function contains all the information of the lifetime data sample.

The maximum likelihood method [EADIE 82][EDWARDS 72][FRODESEN 79] involves the maximisation of the joint probability function, usually referred to as the likelihood function $L(t, \tau)$, with respect to τ . In general

$$L(t, \tau) = \prod_{i=1}^n f(t_i, \tau) \quad (4.9)$$

where f is the probability density function of event i . In practice it is more convenient to use the logarithm of $L(t, \tau)$, known as the support function :

$$l(t, \tau) = \sum_{i=1}^n \ln(f(t_i, \tau)) \quad (4.10)$$

The maximum likelihood principle is then: if the $\mathbf{t} = \{t_1, t_2, \dots, t_n\}$ variables (ie the measured lifetimes in the experiment) are held constant and τ (the parameter to be estimated) is varied, the best estimate of τ is the value of τ for which L is maximal:

$$L(t, \hat{t}) \geq L(t, \tau) \quad \text{for all } \tau \quad (4.11)$$

The support and likelihood functions are maximal for the same τ . It is therefore sufficient that $f(t, \tau)$ be twice differentiable (clearly true for the exponential distribution), and to find τ such that

$$\frac{\delta}{\delta \tau} L(t, \tau) = 0; \quad \frac{\delta^2}{\delta \tau^2} L(t, \tau) \Big|_{\tau=\hat{t}} < 0 \quad (4.12)$$

to obtain an estimate of the mean lifetime.

The variance of the maximum likelihood estimate is determined by the graphical method described in [FRODESEN 79]. This consists of finding the values of τ (τ_1 and τ_2 , say) for which the likelihood function falls to $e^{-0.5}$ of its maximum value, in which case the maximum likelihood estimate of τ lies in the interval $[\tau_1, \tau_2]$ with a confidence level of 68.3%. The quoted confidence interval is true in the limit of an infinite number of observations, ie when the likelihood function is normal. For non-normal likelihood functions the 68.3% confidence level provides a good approximation, provided the likelihood function has a single maximum and does not deviate too much from the normal.

In practice the finite dimensions of the target restrict the available volume for scanning decay lengths. The net effect of this is a depletion of very short and very long lifetimes in the sample, due to the minimum observable decay length (resolution) and the maximum potential decay length (length) of the target (different for each event, since the energy spectrum and production point distribution are folded in). Figure 4.23 below schematically illustrates these effects on the distribution of lifetime data. Losses due to the length of the NA1 target are not large, since it is long enough to scan several (~ 6 mean lifetimes) for the short Λ_C lifetime (see measurement below), but the resolution does distort the lifetime distribution. For this reason $t - t_{\min}$ is plotted as the horizontal axis in the dN/dt plots, in order to correct for this effect (an equivalent correction can be obtained by weighting the data with the reciprocal of the monte carlo scanning efficiency). This has the additional

advantage of allowing a better comparison between the data points and the slope of the lifetime superimposed on the decay time distribution, since the latter was obtained via the maximum likelihood method *with* the acceptance corrections included.

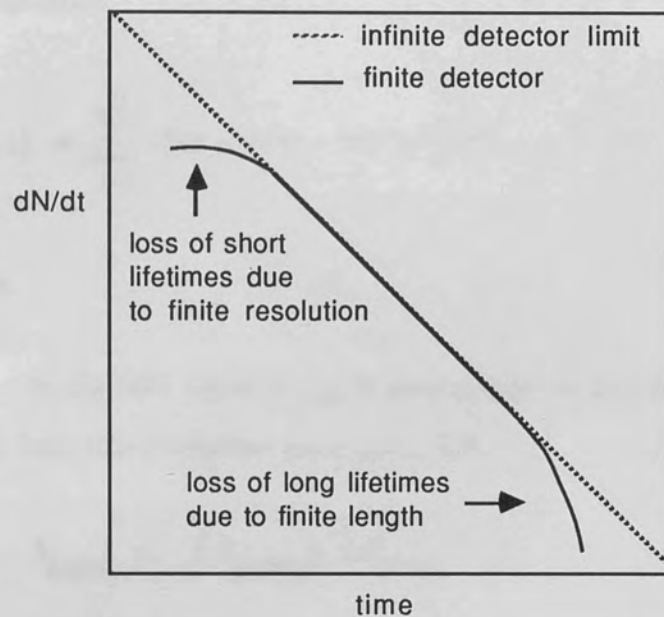


Figure 4.23: Schematic diagram showing the effect of the maximum and minimum observable decay lengths.

The observable probability density function of the decay times is thus a truncation of the true pdf:

$$f(t, \tau) \rightarrow \frac{f(t, \tau)}{\int_{t_{\min}}^{t_{\max}} f(t, \tau) dt} \quad (4.13)$$

Explicitly, for $f(t, \tau) = (1/\tau) \cdot \exp(-t/\tau)$ we have

Λ_C Analysis

$$\frac{1}{\tau} e^{-t/\tau} = \frac{1}{e^{-t_{\min}/\tau} - e^{-t_{\max}/\tau}} \quad (4.14)$$

with support function:

$$l(t, \tau) = \sum_{i=1}^n -\ln \tau - t_i/\tau - \ln(e^{-t_{i,\min}} - e^{-t_{i,\max}}) \quad (4.15)$$

for n lifetimes.

In the NA1 target $t_{i,\min}$ is proportional to the minimum stable level of three strips from the production point ($c=1, \beta=1$)

$$t_{i,\min} = (x_{\text{prod}_{i+3}} - x_{\text{prod}_i}) / \gamma_i \quad (4.16)$$

For a Λ_C with a γ factor of 30 produced at least 3 strips from the end of the germanium target t_{\min} is 0.33×10^{-13} s, which is the time sensitivity of the target for a typical Λ_C .

t_{\max} is defined by the maximum potential time of flight that could be observed, ie the length from the production point to 4 strips before the end of the silicon target, which is 9.9×10^{-13} s for our typical Λ_C (γ factor of 30) produced in the middle of the germanium.

$$t_{i,\max} = (x_{\text{end}-4} - x_{\text{prod}_i}) / \gamma_i \quad (4.17)$$

The errors on the estimate of τ are large if the cutoff for t_{\max} is too short (ie too small a slice of the distribution is observed). Taking, for example, a value of 2×10^{-13} s for the Λ_C mean lifetime implies that the NA1 target scans of the order of 5 mean lifetimes for our typical decay, which is sufficient for a good lifetime

Λ_C Analysis

determination. If, however, the mean lifetime were longer, $10 \times 10^{-13} \text{s}$ say, then the scanning volume would be only one mean lifetime, and a large upper error on the estimate of τ would result. Indeed, very short scanning volumes with respect to the mean lifetime result in no upper limit at all, ie the likelihood function does not turn over.

The time resolution of the target has been studied using the target monte carlo. Using a mean lifetime of $1.5 \times 10^{-13} \text{s}$ and the measured energy spectrum of the Λ_C s, target events were generated and passed through the analysis chain. The conditions and analysis criteria were as for the real data. Each input proper time was subtracted from the corresponding 'measured' proper time, and the result, the time resolution function of the target, is shown in figure 4.24. The FWHM is $\sim 0.4 \times 10^{-13} \text{s}$ leading to a decay time resolution $\sim 0.2 \times 10^{-13} \text{s}$, and the mean is $\sim 0.1 \times 10^{-13} \text{s}$. The decay time resolution of $0.2 \times 10^{-13} \text{s}$ is in agreement with the estimate made using a minimum three strips in the germanium and the average $\Lambda_C \gamma$ factor. The resolution function shows the expected behaviour, ie it has a larger positive tail, corresponding to the scanning program being confused by low excursions in the target readout.

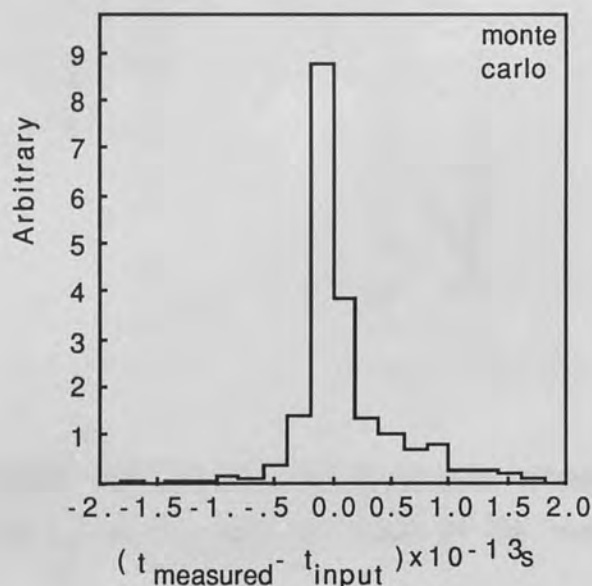


Figure 4.24: time resolution function for the target

The 24 events with matched target pictures have been fitted via the maximum likelihood method outlined above. The result is

Λ_C Analysis

$$\hat{\tau} = 1.4^{+0.4}_{-0.3} \times 10^{-13} \text{ s} \quad (4.18)$$

The χ^2 of the fit compared to the data points $t-t_{\min}$ is 0.36 for one degree of freedom, corresponding to a χ^2 probability of 55%. This is satisfactory, although the significance of this test is doubtful due to the small statistics of the sample and the consequent necessity to use large bins. Nonetheless, that the fit is adequate can be clearly seen from figure 4.25, where the slope of the likelihood fit has been superimposed on the distribution for the $t-t_{\min}$ (acceptance corrected) data.

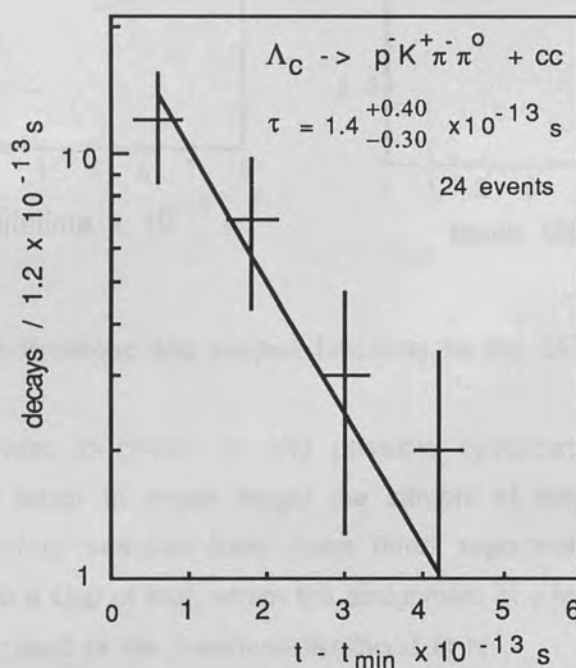


Figure 4.25: decay time distribution corrected for acceptance ($t-t_{\min}$) for the 24 Λ_C events, with the slope of the maximum likelihood fit superposed.

Although the data in figure 4.25 has only been corrected for losses of short lifetimes it is apparent from the figure that there is no significant loss of long lifetimes, demonstrating that the NA1 target is long enough to sample the lifetime distribution in this regime without bias due to the t_{\max} cutoff, and indeed this is

Λ_C Analysis

reflected in the small errors derived from the maximum likelihood fit, given the statistics. The likelihood and support functions are shown in figure 4.26.

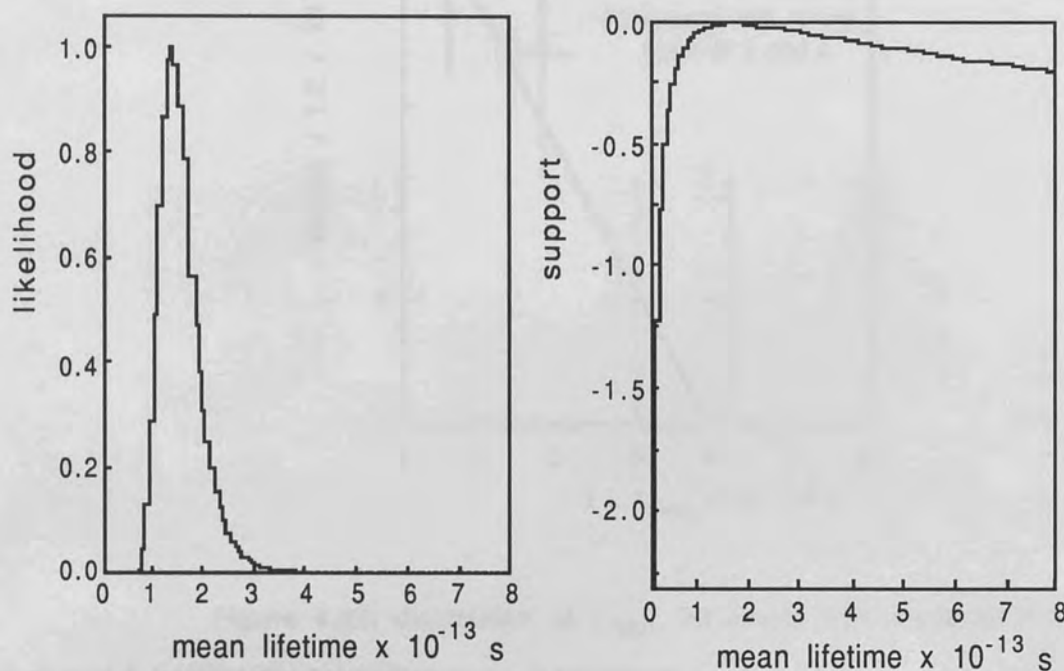


Figure 4.26: likelihood and support functions for the 24 event sample.

In order to check for any possible systematic effect from the misassociation of γ factor to decay length the sample of single-step-of-two and step-two-plus-step-of-four samples have been fitted separately. For the sample with a step of two and a step of four, where the assignment of γ factor to decay length is unambiguous, the result of the maximum likelihood fit is

$$\hat{\tau} = 1.3^{+0.5}_{-0.3} \times 10^{-13} \text{ s} \quad (4.19)$$

No χ^2 is available due to the low statistics, but the reader can judge that the fit is good by reference to the decay time distribution, shown in figure 4.27.

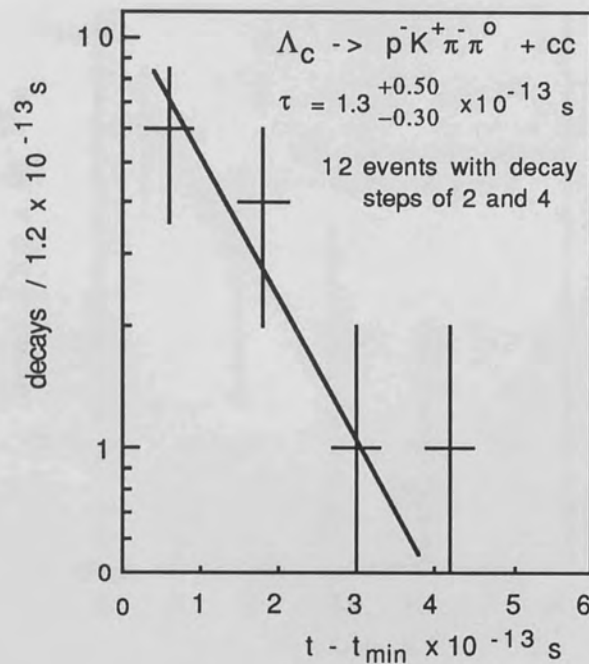
Λ_C Analysis

Figure 4.27: distribution of $t-t_{\min}$ for events with a step of 2 and a step of 4, besides the production step, in the target.

The sample with target readout showing a single step of two besides the production gives a maximum likelihood estimate of the mean lifetime of

$$\hat{\tau} = 1.6^{+0.8}_{-0.4} \times 10^{-13} \text{ s} \quad (4.20)$$

where again no χ^2 is available. The decay time distribution is shown in figure 4.28, and the fit may be seen to be good. The two sub-samples agree well within the errors, and this lends confidence to the hypothesis that there is no significant systematic bias to the lifetime due to misassociation of the γ factor and decay length in the single step sample.

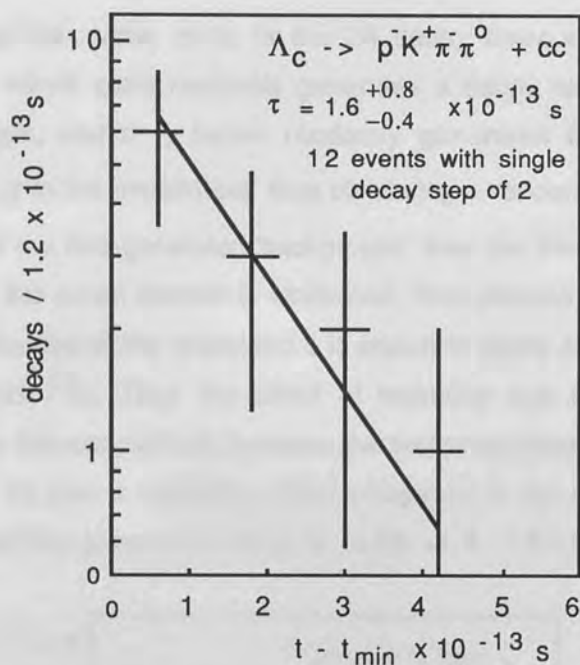
Λ_C Analysis

Figure 4.28: $t-t_{\min}$ distribution for target decay configurations with a production step plus a single step of two.

The background to the lifetime measurement is assessed in the following way: the wrong-sign background (ie the $p^+ K^+ \pi^- \pi^0$) events have been scanned for target configurations of the type used in the lifetime measurement, single-steps-of-two and step-of-two-and-step-of-four. A total of 145 background events were studied in the mass range $2.0\text{-}3.0 \text{ GeV}/c^2$, the vast majority of the target patterns being in saturation, and only one step-of-two-and-step-of-four and nine single-step-of-two (one of which also has a combination in the Λ_C peak) target patterns were observed. In order to normalise the background events to the number of events in the peak the number of background events is multiplied by the ratio of the mass range accepted for the peak and the total mass range scanned for the background, ie 0.08, giving an estimate of 0.08 step-of-two-and-step-of-four background events and 0.72 single-step-of-two background events contributing to the lifetime measurement. An upper limit estimate to the background in the lifetime measurement is that there is one event where a γ factor has been randomly associated to a decay length. It should be noted that the target matching criteria thus greatly suppress the estimated background quoted in table 4.1 from $\sim 30\%$ to $\sim 4\%$.

The effect of this random association has been studied by adding one

Λ_C Analysis

event generated by the monte carlo to the 24 decay times used for the lifetime measurement. The monte carlo randomly generates a decay length uniformly within the NA1 target length, and a γ factor randomly generated from the distribution measured for the Λ_C s in the experiment, thus simulating a random association. The 24 measured times and the one generated 'background' time are then fed into the lifetime fitting software and the mean lifetime is estimated. This process was carried out 100 times, and the distribution of the measured τ is shown in figure 4.29. The mean of the distribution is 1.5×10^{-13} s. Thus the effect of including one randomly associated background event in the sample is to increase the measured mean lifetime on average by 0.1×10^{-13} s, on its own a negligible effect compared to the statistical errors. The lifetime of the randomly generated times is $(5.68 \pm 1.8 \pm 1.2) \times 10^{-13}$ s.

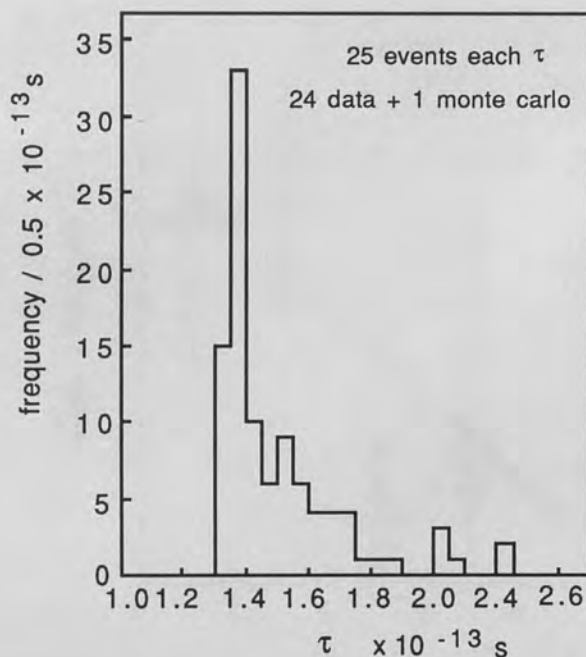


Figure 4.29: distribution of measured mean lifetime when one randomly generated decaytime is added to the sample.

In order to demonstrate that the measured Λ_C lifetime is not a feature of the target size or analysis criteria the lifetime of the ten events from the wrong-sign background, which was arrived at using the same cuts, has been measured. The result is

Λ_C Analysis

$$\hat{\tau} = 4.9^{+8.0}_{-2.0} \times 10^{-13} \text{ s} \quad (4.21)$$

and the acceptance corrected decay time distribution is shown in figure 4.30 (note the changes of scale and bin size when comparing to the Λ_C decay time distributions). The measured lifetime of the background is longer than for the Λ_C , and the errors much larger due to the poor quality of the fit. No χ^2 is available due to the low statistics, but the decay time distribution shows that the fit is not good. The likelihood function for these background events is shown in figure 4.31, where the large high tail explains the large positive error, and this should be compared with figure 4.26 (again note the change in horizontal scale).

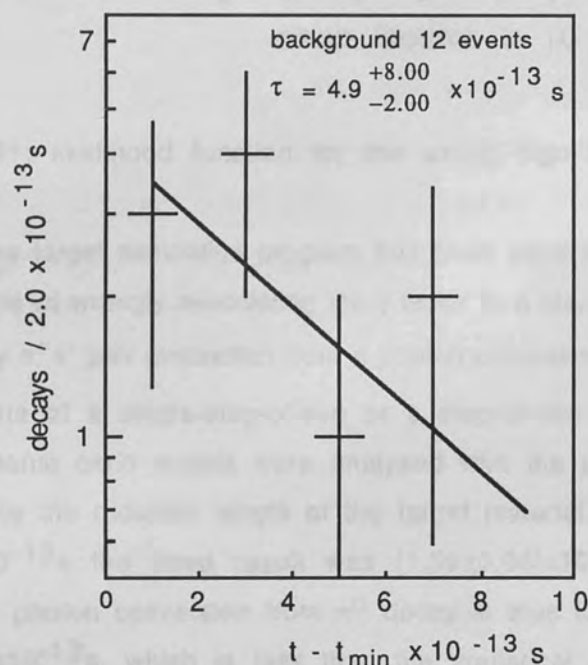


Figure 4.30: acceptance corrected decay time distribution of the wrong-sign background events, with the slope of the maximum likelihood fit superimposed.

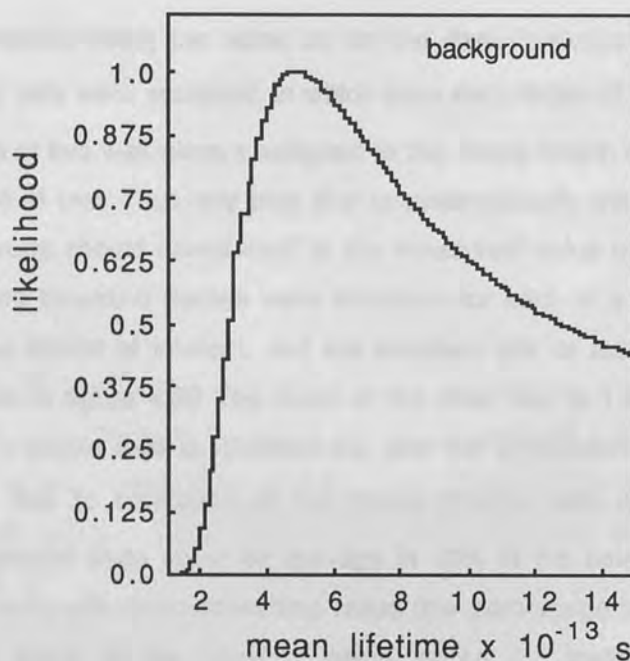
Λ_C Analysis

Figure 4.31: likelihood function for the wrong sign background events.

The target simulation program has been used to study the possible effect on the lifetime of wrongly associating the γ factor to a step of two produced not by Λ_C decay but by e^+e^- pair production from a photon originating from the π^0 . Using the analysis criteria of a single-step-of-two or a step-of-two-and-step-of-four the results of 1000 monte carlo events were analysed with the probability of photon conversion given by the radiation length of the target material. For an input mean lifetime of $1.5 \times 10^{-13} \text{ s}$ the fitted result was $(1.59 \pm 0.06) \times 10^{-13} \text{ s}$. The effect of steps of two from photon conversion from π^0 decay is thus to increase the mean lifetime by $\sim 0.1 \times 10^{-13} \text{ s}$, which is less than the statistical error. The effect of photon conversion is not significant due to the small fraction of radiation length seen by the average photon from π^0 decay and the analysis criteria of not more than one step of two in the target readout.

As a study of the possible systematic bias to the lifetime due to the misassociation of the decay length and γ factor in the step-of-two-sample, the target monte carlo has been run with with Λ_C anti- Λ_C pair production, one decaying solely into steps of two, and the other, in the absence of detailed branching ratios, 50% into steps of two and 50% into steps other than two. The input mean lifetime of the Λ_C was fixed and the output of the simulation was passed through the NA1 target analysis

Λ_C Analysis

chain, the target selection being the same as for the data, ie single steps of two or steps of two and four only were accepted, in which case the γ factor of the Λ_C decaying exclusively into steps of two was always assigned to the decay length corresponding to the charge increment of two. Thus any bias due to systematically getting the γ /decay length association wrong should reveal itself in the 'measured' value of τ output by the analysis program. One thousand decays were simulated for each of a number of input mean lifetimes in the region of interest, and the resultant plot of the input τ against the τ output is shown in figure 4.32 The slope of the fitted line is 1.00 ± 0.04 and the intersection on the τ output axis is -0.025 ± 0.03 , and the conclusion is that there is no systematic bias due to confusion of the decay lengths with Λ_C anti- Λ_C pair production. Misassociation does occur on average in 10% of the time measurements made in the monte carlo with these branching ratios (the percentage of misassociation is sensitive to the value of the input τ , being worse for smaller τ since the 'reconstructed' particle is more likely to have a decay unresolvable from the production step - for τ input = 1.5×10^{-13} s the misassociation is $\sim 7\%$), but because both decay lengths result from the same type of particle in the Λ_C anti- Λ_C pair production monte carlo the effect is averaged out.

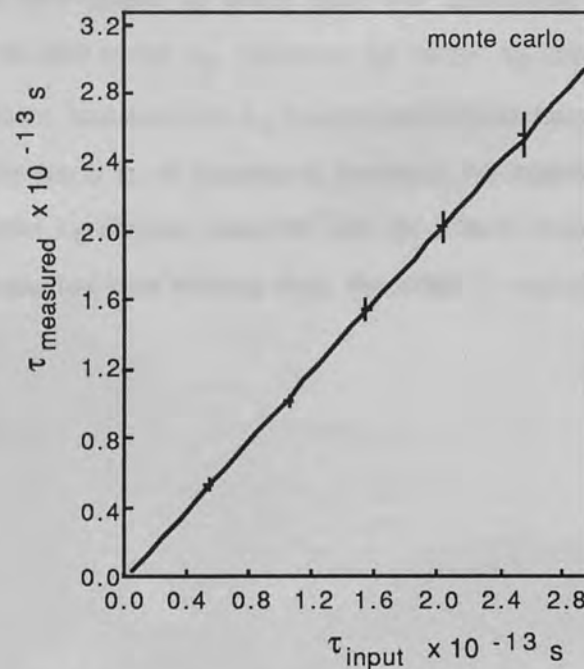


Figure 4.32: monte carlo plot of τ measured with the analysis program against the input τ for Λ_C pair production.

Λ_C Analysis

A more serious problem is anticipated if there is a significant component of Λ_C D associated production, where there is the possibility of missing the short decay length and associating the Λ_C γ factor to the D decay length systematically. This possibility has also been studied using the target monte carlo. The production is assumed to be Λ_C associated with anti- Λ_C and an equal mixture of D^+ and D^0 . Again the Λ_C decays exclusively into a charge change of two whilst the anti- Λ_C , D^+ and D^0 mixture decays 50% into steps of two, 50% into steps other than two. The results of the analysis program are shown in figure 4.33 for four values of τ input and varying degrees of associated production. Note that the % of D production shown along the horizontal axis is half D^0 , half D^+ , ie 20% on the horizontal axis means 10% D^0 + 10% D^+ of the total production in the associated channel, the remaining component (80% in this example) going into anti- Λ_C .

The results in figure 4.33 exhibit systematic bias in the mean lifetime measured due to the contamination from longer D decay lengths mistaken for Λ_C . The effect is particularly strong for very short Λ_C lifetime (see the $\tau = 0.5 \times 10^{-13}$ s trend) where a large number of the Λ_C 's decay with such a short decay length as to be unresolvable in the NA1 target, in which case the associated D decay length is frequently mistaken for that of the Λ_C . However, for longer Λ_C mean lifetime the effect becomes less significant, because the Λ_C decays themselves become resolvable with higher efficiency. The trend is, of course, to increase the measured lifetime. In the region of the measured Λ_C lifetime, however, and for a level of associated production less than 20%, as expected from existing data, the effect is negligible.

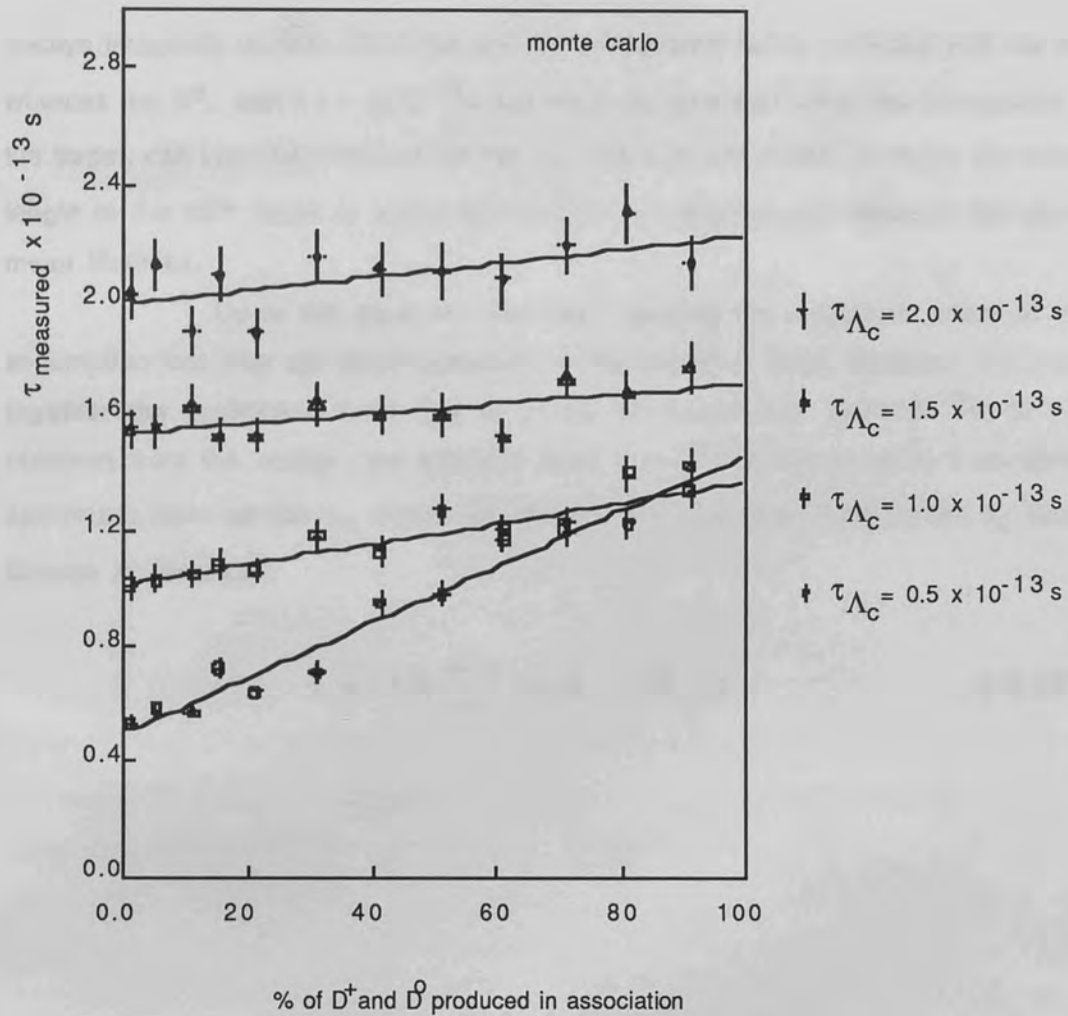
Λ_c Analysis

Figure 4.33: dependence of the output mean lifetime on the input mean lifetime and mixture of associated production, calculated by the target monte carlo. (see text).

	<u>slope</u>	<u>intersect</u>
$\tau_{\text{input}} = 0.5 \times 10^{-13} \text{ s}$	0.0097 ± 0.004	$(0.5 \pm 0.01) \times 10^{-13} \text{ s}$
$\tau_{\text{input}} = 1.0 \times 10^{-13} \text{ s}$	0.0036 ± 0.005	$(1.01 \pm 0.02) \times 10^{-13} \text{ s}$
$\tau_{\text{input}} = 1.5 \times 10^{-13} \text{ s}$	0.0018 ± 0.007	$(1.53 \pm 0.03) \times 10^{-13} \text{ s}$
$\tau_{\text{input}} = 0.5 \times 10^{-13} \text{ s}$	0.0025 ± 0.009	$(1.98 \pm 0.04) \times 10^{-13} \text{ s}$

The trend is almost completely due to contamination from D^0 decays, since the D^+ , with a $\tau = 10 \times 10^{-13} \text{ s}$ and its correspondingly longer decay lengths,

Λ_C Analysis

decays frequently outside the target and is consequently rarely confused with the Λ_C , whereas the D^0 , with a $\tau = 4 \times 10^{-13}$ s and decay lengths well within the acceptance of the target, can often be mistaken for the Λ_C . The problem of misidentifying the decay length in the NA1 target is worse for mixtures of particles with different, but close, mean lifetimes.

Up to this point we have been ignoring the systematic errors on the assumption that they are small compared to the statistical error. However, if we add together the systematic error due to γ from π^0 conversion (0.1×10^{-13} s) to that obtained from the background estimate (also 0.1×10^{-13} s) we arrive at a combined systematic error on the Λ_C lifetime of $\pm 0.2 \times 10^{-13}$ s. Our final result on the Λ_C mean lifetime is therefore:

$$\hat{\tau} = 1.4^{+0.4}_{-0.3} \pm 0.2 \times 10^{-13} \text{ s} \quad (4.22)$$

5: Conclusions

This thesis has presented evidence for Λ_C photoproduction and measured the lifetime of the Λ_C charmed baryon. In the following a summary of the results is given. This is followed by a discussion and comparison of the results with the current status of Λ_C lifetime measurements. Also, the measurement of the D^0 lifetime by the collaboration is introduced and discussed. Finally, a number of areas where the experiment could have been improved are reviewed.

A total of 63 Λ_C^\pm candidates have been isolated in the channel $p^+K^-\pi^+\pi^0$ and charge conjugate. These are believed to be Λ_C because: (i) the effective masses of these candidates are well clustered around the nominal Λ_C mass, 2.28 GeV/c² [PDG 86]; (ii) the mean lifetime of a sub-sample of these candidates is consistent with the decay of the hadrons containing the charmed quark. Various tests have been made to confirm that the signal in the effective mass distribution at 2.28 GeV/c² is not a result of the analysis techniques used. These tests consist of performing an identical analysis on the channel $p^+K^+\pi^-\pi^0$ and charge conjugate, in which case no signal is observed in the effective mass spectrum, and checking for ambiguity with other charmed particles where kinematical reflections are known to exist, in which case a small number of ambiguous events are seen, consistent with the level of background. Of these 63 candidates, 33 are Λ_C and 30 are anti- Λ_C , consistent with the assumption that the dominant production mechanism is Λ_C anti- Λ_C pair production.

A sub-sample of 24 of these events for which the decay length was resolved in the target and could be matched to the information from the forward spectrometer was used to measure the mean lifetime of the Λ_C , which was found to be:

$$\tau(\Lambda_C) = (1.4 \pm 0.4 \pm 0.3 \pm 0.2) \times 10^{-13} \text{ s}$$

The first two errors quoted are statistical, while the third is

Conclusions

systematic, calculated using the target monte carlo program.

The decay of the Λ_C into $pK\pi^0$ has also been observed in 400GeV/c pp interactions in the LEBC bubble chamber and EHS spectrometer [AGUILAR 88]. However, experiment NA1 is the first to report the double resonant substructure $\Delta^{++}K^{*-}$ and Δ^+K^{*0} -bar in Λ_C decays, although $\Delta^{++}K^-$ has been observed in the channel $pK\pi$ in e^+e^- annihilation (MARK II, ARGUS, see eg [HITLIN 87]), and both Δ^{++} and K^{*0} -bar separately in the $pK\pi$ channel in pp collisions at the CERN ISR [BASILE 81].

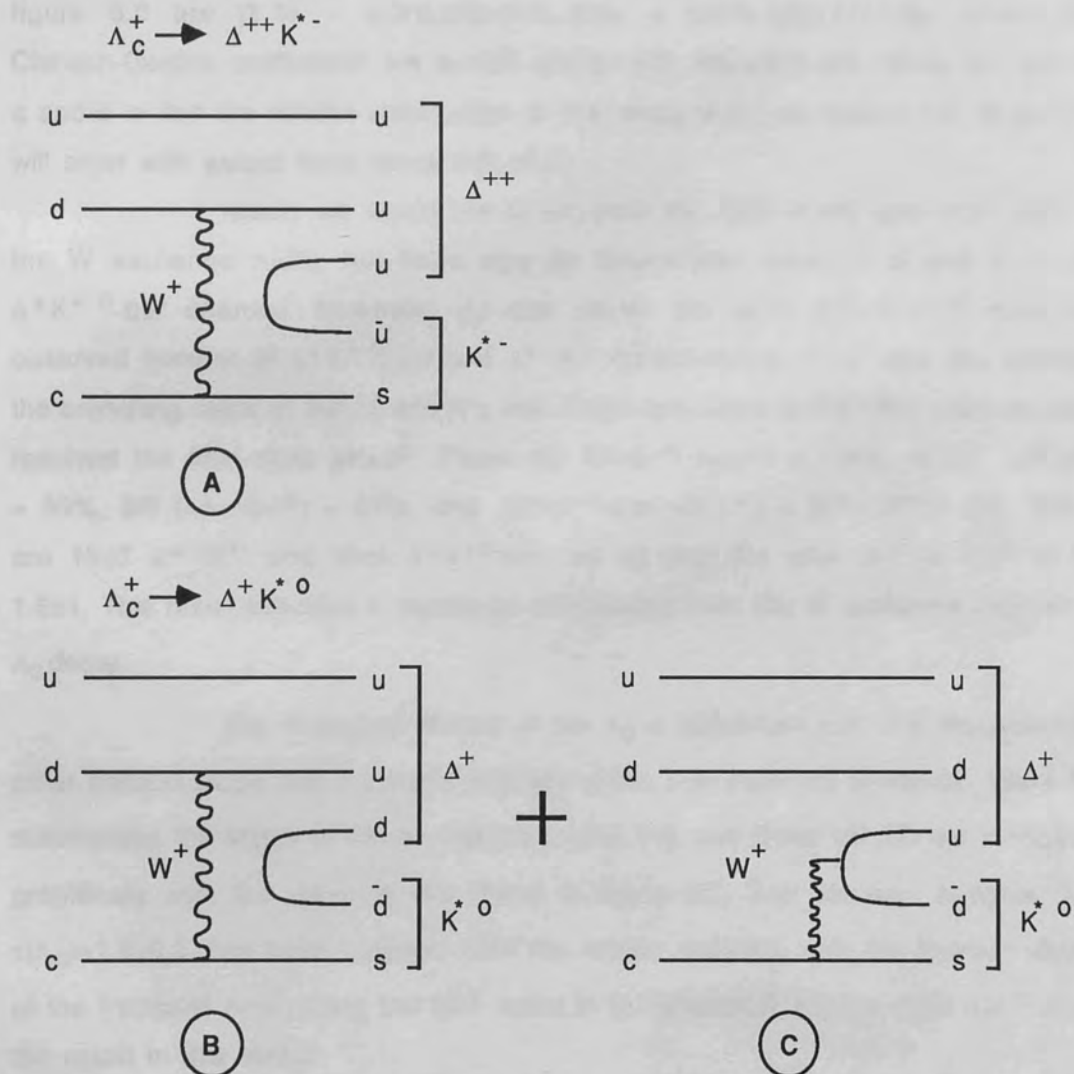


Figure 5.0: analysis of $\Lambda_C \rightarrow \Delta K^*$ decays

Conclusions

It has been pointed out elsewhere by the collaboration [AMENDOLIA 87] that the decay $\Lambda_C \rightarrow \Delta^{++} K^{*-}$ can proceed only through the exchange of a virtual W boson (or via rescattering processes of low probability), whilst the decay $\Lambda_C \rightarrow \Delta^+ K^{*0-\text{bar}}$ may proceed via W exchange or via spectator decay, see figure 5.0. The weak interaction does not conserve isospin: the Λ_C has isospin 0 and the ΔK^* final states can have isospin 2 or 1 (in the notation $|I, I_3\rangle$ then $\Delta^{++} = |3/2, 3/2\rangle$, $\Delta^+ = |3/2, 1/2\rangle$, $K^{*-} = |1/2, -1/2\rangle$ and $K^{*0-\text{bar}} = |1/2, 1/2\rangle$). Under the assumption that this is a $\Delta I = 1$ transition ($|0, 0\rangle \rightarrow |1, 1\rangle$) the contribution of diagrams A and B in figure 5.0 are $|1, 1\rangle = a|3/2, 3/2\rangle|1/2, -1/2\rangle + b|3/2, 1/2\rangle|1/2, 1/2\rangle$ where the Clebesh-Gordon coefficients are $a = \sqrt{3}/2$ and $b = -1/2$. Squaring and taking the ratio of a and b to find the relative contribution to the decay width we expect that diagram A will enter with weight three times that of B.

Ideally we would like to compare the ratio of the spectator width to the W exchange width, but there may be interference between B and C in the $\Delta^+ K^{*0-\text{bar}}$ channel. However, we can obtain the ratio $|A|^2/|B+C|^2$ from the observed number of $\Delta^+ K^{*0-\text{bar}}$ and $\Delta^{++} K^{*-}$ combinations, if we take into account the branching ratios of the Δ s and K^* s into states detectable in FRAMM, since we only resolved the final state $pK\pi\pi^0$. These are $\text{BR}(\Delta^{++} \rightarrow p\pi^+) = 100\%$, $\text{BR}(K^{*-} \rightarrow K^-\pi^0) = 33\%$, $\text{BR}(\Delta^+ \rightarrow p\pi^0) = 67\%$, and $\text{BR}(K^{*0-\text{bar}} \rightarrow K^-\pi^+) = 67\%$ [PDG 86]. There are 19 ± 7 $\Delta^{++} K^{*-}$ and 16 ± 4 $\Delta^+ K^{*0-\text{bar}}$, so we find the ratio $|A|^2/|B+C|^2$ to be 1.6 ± 1 . This result indicates a significant contribution from the W exchange process to Λ_C decay.

The measured lifetime of the Λ_C is consistent with that measured by other collaborations and the world average within one standard deviation. Table 5.0 summarises the status of the Λ_C lifetime [LUTH 88], and these results are compared graphically with the result in this thesis in figure 5.1. The average in figure 5.1, $\tau(\Lambda_C) = 1.9 \pm 0.2$, has been obtained from the results weighted with the inverse square of the fractional error, using the NA1 result in [AMENDOLIA 87] but does not include the result in this thesis.

It should be emphasised that NA1 directly observes the decay length of the Λ_C and that the target has good resolution, $\sim 0.2 \times 10^{-13}$ s for a typical Λ_C . These factors minimise our systematic bias and, together with the improved statistics in

Conclusions

this thesis, allow us to quote one of the smallest errors.

Experiment	reference	vertex detector	number of decays	$\tau(\Lambda_c) \times 10^{13} \text{s}$
E351	USHIDA 86	emulsion	13	$2.0^{+0.7}_{-0.6}$
WA58	ADAMOVICH 86	emulsion	11	$2.3^{+0.9}_{-0.6} \pm 0.4$
NA27	AGUILAR 88	bubble chamber	9	$1.2^{+0.5}_{-0.3}$
NA32	BARLAG 87	OCD	37	$1.6^{+0.4}_{-0.3} \pm 0.3$
E691	ANJOS 87b	Si microstrip	97	$2.2 \pm 0.3 \pm 0.2$
NA1	AMENDOLIA 87	active target	9	$1.1^{+0.8}_{-0.4}$
NA1	this thesis	active target	24	$1.4^{+0.4}_{-0.3} \pm 0.2$

Table 5.0: summary of Λ_c lifetime measurements

In particular note that the high resolution bubble chamber experiment NA27 LEBC/EHS, which is likely to be a good indicator of the lifetime since the decay length itself is directly observed, measures a short lifetime of $(1.2^{+0.9}_{-0.6}) \times 10^{13} \text{s}$. Experiment E691 has the largest statistics, using silicon microstrip detectors in a photon beam, but note used a cut of 8σ for the minimum decay length in order to obtain a clean signal, where σ was typically $300\mu\text{m}$, which corresponds to ~ 1 mean decay length of a Λ_c of γ factor = 30.

Fermilab experiment E691 (also referred to as TPS Tagged Photon Spectrometer) represents the best example of a charm photoproduction experiment to date. E691 should be considered a 'second generation' charm photoproduction experiment in terms of its electronic vertex detector (silicon microstrip detectors), and NA1 a 'first generation' experiment. Despite this difference in vertex detector technology the signal to noise ratio in NA1 was essentially comparable with that of E691. The greatest difference lies in the more intense beam at Fermilab (~ 10 times as intense as the H4 beamline at CERN used in NA1), allowing greater statistics to be

Conclusions

accumulated, aided by TPSs greater momentum acceptance of the Cerenkovs and the ACP (Advanced Computer Project) microprocessor farm which coped with the large data volume.

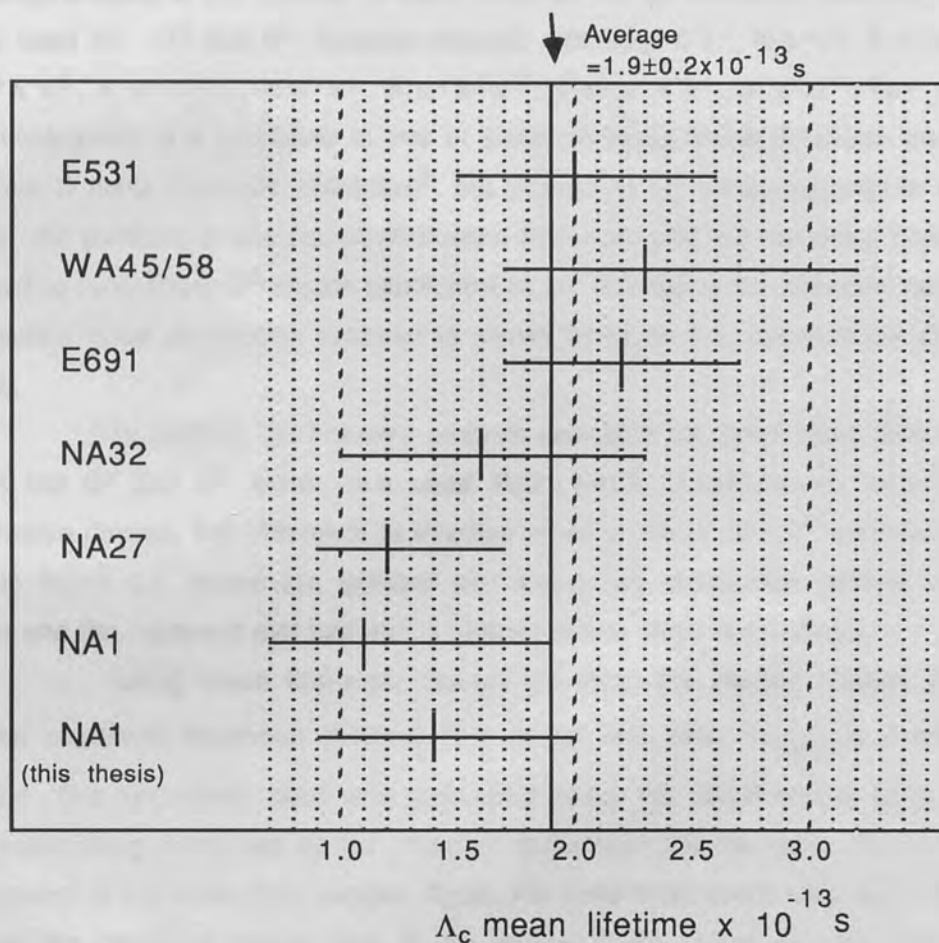


Figure 5.1: world Λ_C lifetime results

With a single mean lifetime measurement there always remains the possibility that the result is solely a feature of the measurement technique, particularly when the device used has as limited acceptance as the NA1 target. However, we are confident that this is not the case as we have previously reported a measurement of the D^0 lifetime from 58 decays [AMENDOLIA 88]:

$$\tau(D^0) = (3.4 +0.6 -0.5 \pm 0.3) \times 10^{-13} \text{ s}$$

Conclusions

where the first two errors are statistical and the third is systematic. This result is compatible with other measurements of the D^0 lifetime.

The analysis techniques were different for the D^0 . Forty-six of the decay lengths used in the lifetime fit were obtained via an exclusive analysis. This analysis used the D^0 and D^+ Cabbibo-allowed channels $K^-\pi^+$, $K^-\pi^+\pi^0$, $K^-\pi^+\pi^+\pi^-$, $K^-\pi^+\pi^+\pi^-\pi^0$, $K^-\pi^+\pi^0\pi^0$, $K^-\pi^+\pi^+$, $K^-\pi^+\pi^+\pi^0$, $K^-\pi^+\pi^+\pi^-\pi^+$, $K^-\pi^+\pi^+\pi^0\pi^0$ and charge conjugates. If a candidate in one of these channels fell in a narrow window around the D mass (typically $\pm 70 \text{ MeV}/c^2$, but depending on the background in each channel) the particles in this combination were excluded, and the remaining particles were used to reconstruct D^0 meson candidates in the first five of the channels quoted. The effective mass distribution obtained is shown in figure 5.2, summed for all D^0 channels.

In addition, an inclusive analysis exploiting the small mass difference between the D^* and D^0 states (we used $M(D^*) - M(D^0) \leq 156 \text{ MeV}/c^2$) isolated a further twelve decays. The difference in effective mass of the D^* and D^0 candidates is shown in figure 5.3, where the lefthand plot shows the distribution without target selection and the righthand plot that with a request of two steps in the target.

Using these fifty-eight decays we fitted the lifetime quoted above using the maximum likelihood method. The decay time plot ($t - t_{\text{min}}$) is shown in figure 5.4. The systematic error was calculated using the target monte carlo, the quoted value being dominated by the γ from π^0 conversion and the upper limit of 10% contamination of the decay time sample. Again, the systematic errors were found to be less than the statistical errors. Due to the nature of the target and the possible ambiguities in assigning γ factors to decay lengths note that the target monte carlo played a central role in the lifetime measurements.

The fact that we have measured two different lifetimes with the same device indicates that neither is a result of the properties of the device used. The small magnitude of the systematic errors also lends confidence to the results. One of the advantages of NA1 is that the target and the spectrometer are completely independent devices, ie the tagging of a charm candidate is completely independent of the decay length measurement, thus minimising any bias in the lifetime measurement due to the analysis technique used.

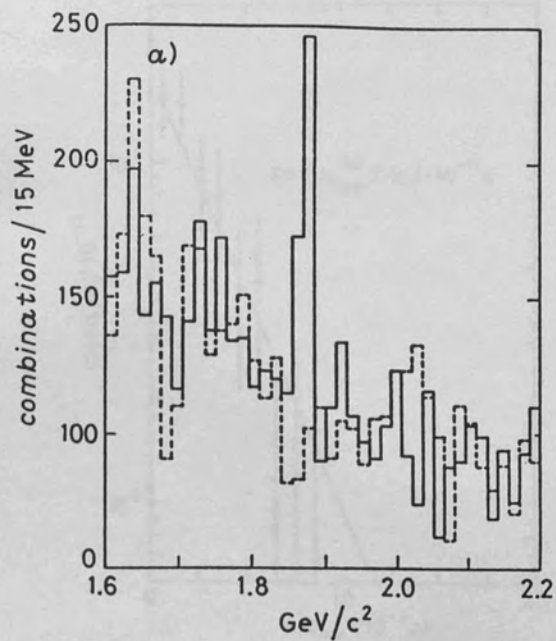


Figure 5.2: D^0 effective mass distribution obtained via the exclusive analysis outlined in the text

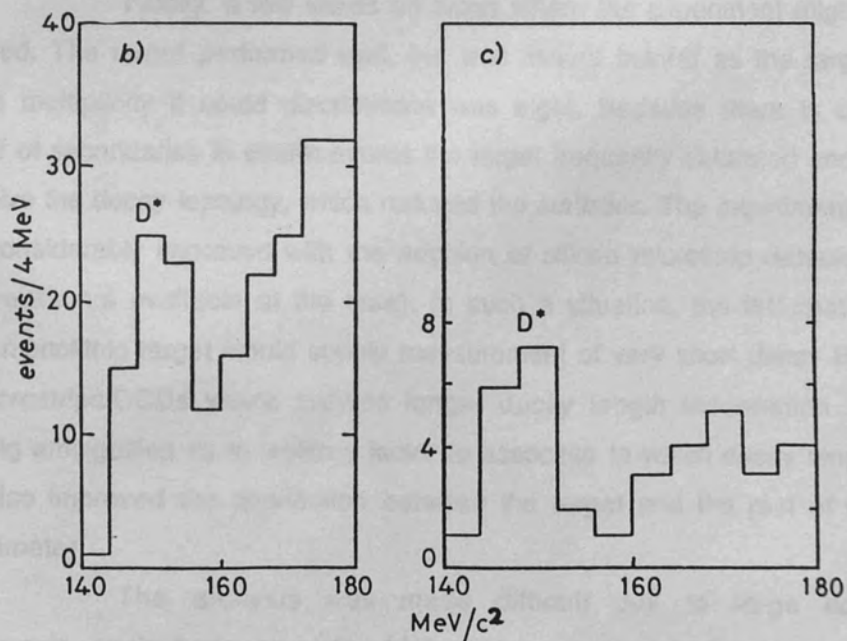


Figure 5.3: $M(D^*)-M(D^0)$ mass difference distribution obtained via the inclusive analysis: left, no target cut; right with a request for two steps in the target

Conclusions

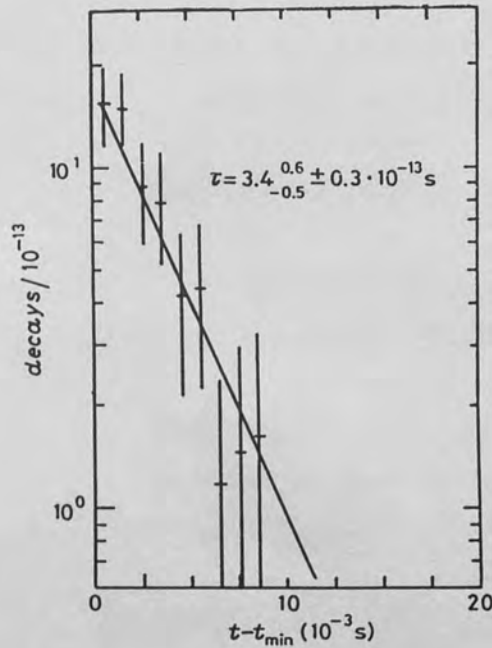


Figure 5.4: decay time ($t-t_{\min}$) distribution for the 58 D^0 decays, with the slope of the maximum likelihood fit superimposed.

Finally, a few words on areas where the experiment might have been improved. The target performed well, but was limited insofar as the largest charged particle multiplicity it could discriminate was eight. Because there is often a large number of secondaries in charm events the target frequently saturated and was unable to resolve the decay topology, which reduced the statistics. The experiment would have been considerably improved with the addition of silicon microstrip detectors or CCDs (these were not available at the time). In such a situation, the information provided by the monolithic target would supply measurement of very short decay lengths whilst the microstrips/CCDs would provide longer decay length information and help in resolving ambiguities as to which γ factor to associate to which decay length. It would have also improved the connection between the target and the rest of the FRAMM spectrometer.

The analysis was made difficult due to large combinatorial backgrounds, again because of the high average multiplicity in charm events. This problem would have been eased by using Cerenkov detectors with finer modularity and greater momentum acceptance, in particular for discriminating K and π in D decays.

References

- ADAMOVICH 86 M. Adamovich *et al*, CERN/EP 86-77 (1986)
- AGUILAR 88 M. Aguilar-Benitez *et al*, CERN/EP 88-49, 1988 and Phys. Lett. 189,1,2(1987)254
- ALBINI 82 E. Albini *et al*, Phys. Lett. Vol.110B , Nos. 3, 4 , P.339, April 1982 "Electronic Measurement of the Lifetime of D^{\pm} Mesons"
- ALTARELLI 74 G. Altarelli & L. Maiani, Phys. Lett. (1974) 52B,351
- AMENDOLIA 80a S.R. Amendolia, Pisa INFN Preprint, Pisa 80-84 (1980)
- AMENDOLIA 80b S.R. Amendolia, Pisa INFN Preprint, Pisa 80-83 (1980)
- AMENDOLIA 80c S.R. Amendolia *et al*, NIM 206 (1980) P.367
- AMENDOLIA 83 S.R. Amendolia *et al*, IEEE Transactions on Nuclear Science Vol. NS-30, No.1, Feb 1983
- AMENDOLIA 84a S.R. Amendolia *et al*, Nuclear Instruments & Methods 226, (1984) 78-81
- AMENDOLIA 84b S.R. Amendolia *et al*, Nuclear Instruments & Methods 226, (1984) 117-121
- AMENDOLIA 84c S.R. Amendolia *et al*, IEE Transactions on Nuclear Science Vol. NS-31, No.2, April 1984
- AMENDOLIA 87 S.R. Amendolia *et al*, Z. Phys. C36 (1987) 513-516

- AMENDOLIA 88 S.R. Amendolia *et al*, Europhys. Lett., 5 (5) pp. 407-412 (1988)
- ANJOS 87a J.C. Anjos *et al*, Fermilab Conference 87/37-E
- ANJOS 87b J.C. Anjos *et al*, FERMILAB-PUB-87/218E (1987)
- BARGER 80 V. Barger *et al*, Phys. Rev. D 44,4(1980)226
- BARLAG 87 S. Barlag *et al*, Z. Phys. C37 (1987)17
- BASILE 81 M. Basile *et al*, Il Nuovo Cimento 62A,N.1(1981)14
- BELLINI 81 G. Bellini *et al*, Pisa INFN Preprint NA1/81/07
- BURAS 86 A.J. Buras, J.M. Gerard, R. Rucke, Nuclear Physics B268, 16 (1986)
- CHARPAK 85 G. Charpak, Trends in Particle Detectors CERN-EP/85-127 Aug 1985
- DAMMERELL 84 C.J.S Dammerell "Recent Developments in Solid State Vertex Detectors" RAL-84-123 Dec 1984
- DARRIULAT 87 P. Darriulat, Rappoteurs talk, Proc. Int. Europhysics Conf. on H.E.P Uppsala Sweden 1987, Page 745
- EADIE 82 W.T. Eadie, D. Drijard, F.E. James, M. Roos, B. Sadoulet "Statistical Methods in Experimental Physics" North Holland 1982
- EDWARDS 72 A.W.F. Edwards, "Likelihood" CUP 1972

- FRODESEN 79 A.G. Frodesen, O. Skjeggeslad & H. Tøfke
"Probability and Statistics in Particle Physics"
Universitetsforlaget 1979
- GAILLARD 74 M.K. Gaillard & Benjamin W. Lee
Phys. Lett. 33,108 (1974)
- GATTI 86 E. Gatti & P.F. Manfred, Rivista del Nuovo Cimento
Vol.9, No.1 (1986)
- GUBERINA 79 B. Guberina, S. Nussinov, R.D. Peccei, R. Nickel
Phys. Lett. 89B,111 (1979)
- GUBERINA 86 B. Guberina *et al*, "Charmed Baryon Lifetime Differences"
Z. Phys. C33(1986)297
- HITLIN 87 D. Hitlin, Rapporteurs talk,
Proc. 1987 Int. Symp. Lepton and Photon Interactions at High
Energies, Hamburg 1987, Page 212
- HOLMES 85 S. Holmes *et al*, Ann. Rev. Nucl. Part. Sci.
1985 35: 397-454
- Mc HUGH 87 Sean Mc Hugh, "Review of D_s and Λ_c Decays"
Proc. Int. Europhysics Conf. on H.E.P
Upsala Sweden 1987, P.348
- HUGHES 85 I.S. Hughes, "Elementary Particles"
CUP 1985
- JAMES 68 James, Monte Carlo Phase Space, CERN 68-15 (1968)
- KALMUS 82 Kalmus, 21st International Conference on HEP, Paris 1982

- LANDAU 44 L. Landau, Journal of Physics USSR 8, 201 (1944)
- LINDHARD 63 J. Lindard, V. Nelson, M. Scharff, P.V. Thomson
Mat. Fys. Medd. Dan. Vid. Selsk 33 No.10 (1963)
- LUTH 88 V. Luth, SLAC-PUB-4552 (1988)
- MARTIN 88 A.D. Martin, "Topics in HEP", IOP Publishing (1988) P.89
- MOYAL 55 J.E. Moyal Phil. Mag. 46(1955)263
- NASH 83 Proceedings of the 1983 International Symposium on
Lepton and Photon Interactions at High Energies
(Cornell) P.352-354
- NASH 87 Study of Charm Production Mechanisms at Fermilab Tagged
Photon Spectrometer, Fermilab-conf-87/71 (1987)
- PDG 86 Particle Data Group, "Review of Particle Properties"
Pys. Lett. 170B(1986)
- RANCOITA 82 P.G. Rancoita & A. Siedman,
Rivista del Nuovo Cimento, Vol.5, No.7 (1982)
- RATOWSKI 75 A. Ratowski, Nuclear Instruments & Methods, 130
(1975) 533-538
- ROSEN 80 S.P. Rosen, Physics Review Lett. 44, 4 (1980)
- RUCKL 83 R. Ruckl, "Weak Decays of Heavy Flavours"
Habilitationsschrift University of Munich,
CERN print (1983)

- RUCKL 85 R. Ruckl, "Heavy Flavours"
copies of transparencies (unpublished)
CERN Academic Training March 1985
- RUCKL 87 R. Ruckl, Proc. XXIII Int. Conf. on H.E.P.
Berkeley, California (1987) Page 797
- SACKS 87 L.E. Sacks, A Measurement of the Lifetime of the Neutral
Charm Meson using an Active Target
Ph.D. Thesis, University of London, 1987
- SAULI 77 CERN 77-09 (1977) P.7
- SCHUBERT 87 K. R. Schubert, Rappoteurs talk,
Proc. Int. Europhysics Conf. on H.E.P
Uppsala Sweden 1987, Page 791
- SILVERMAN 88 D. Silverman & H. Yao, Phys. Rev. D 38,1(1988)214
- USHIDA 86 N. Ushida *et al.* Phys. Rev. Lett. 56 (1986) 1767